MATERIALS SCIENCE AND ENGINEERING

Seed Money Fund

A New Microwave-Driven Pack Cementation Coating Process

J. Kiggans,[1] T. Tiegs,[1] M. Losego,[2] S. Nunn,[1] L. Riester,[1] M. Williams,[1] and R. Lowden[1]
[1]*Metals and Ceramics Division*
[2]*Office of Science, Energy Research Undergraduate Laboratory Fellowship*

Experiments were performed to determine if microwave heating can be used to apply diffusion coatings to metal alloy parts. In order to maintain a broad scope for this project, three metal alloys were selected which represent materials of interest for future research areas. These alloys included a tool steel (A2), a low-carbon steel (1018), and a nickel-chrome super alloy (625). Three types of diffusion coating processes were chosen: aluminization, chromization, and boronization. Control samples were processed by conventional heating. Aluminum-, chrome-, and boron-based diffusion coatings were successfully created using microwave heating. These microwave coatings show some similarities to the conventionally produced coatings, although significant differences also existed in some cases. Very encouraging results were obtained with the A2 tool steel.

Introduction

The use of microwave (MW) energy or processing as a tool for materials processing emerged during the late 1950s, but only within the past two decades has MW research really gained a foothold in the scientific community. Researchers in both the scientific and industrial communities have begun to explore MW technology as a way to improve even well-established processing practices.[1]

Pack cementation is a surface modification technique primarily used for metallic components to increase oxidation/corrosion resistance, wear resistance, and/or surface hardness. Pack cementation is a diffusion-based technique in which the desired species diffuses into the material through the surface. This diffusion creates a solid solution region near the surface with enhanced properties. Common diffusion-driven surface treatments include aluminizing, chromizing, and borodizing. The actual pack cementation process involves packing the untreated metal parts in a powder bed or pack and then heat-treating at temperatures between 800–1000°C. The powder pack consists of three general components: the desired diffusion source material, a halide activator (such as NaCl or NH_4Cl), and an inert filler (typically alumina). At elevated temperatures, the source material reacts with the halide to form a gas, which permeates the porous pack. Upon reaching the surface of the sample, another reaction occurs, depositing the source material on the substrate. Due to the high processing temperatures, the deposited element typically diffuses into the surface, leading to the desired surface treatment. The filler material is present simply to deter sintering.[2] Due to its simplicity and ability to coat even complicated parts, pack cementation continues to be a popular surface treatment method.

Current knowledge surrounding MW processing practices seems to indicate that pack cementation could be improved with the use of MW heating. Exposure of the pack cementation materials to MW energy should exploit the unique characteristics of MW heating behavior, as compared to conventional heating, which should provide several benefits. Depending on the dielectric properties of each component, they will absorb energy differently and therefore heat at different rates. It is well known that dispersed metal particulates heat extremely well in a MW furnace and they should do so in the pack cementation bed. In the above example, the aluminum powder would heat preferentially. The halide activator may or may not heat well by microwaves, depending on its dielectric properties.[3] For instance, the NH_4Cl in the above example would heat better than the NaCl (based on dielectric loss tangents), but neither would heat up as well as the aluminum. However, if one uses $CuCl_2$ as the activator, it heats just as well as the aluminum. Thus, by choosing appropriate halides, that heat or do not heat, further control of the cementation process can be obtained. In general, the inert filler powder would not heat well in a microwave furnace if an oxide, such as Al_2O_3, were employed. However, if fillers such as SiC are used, it could also be modified to tailor the heating response of the cementation pack.

Typically MW energy is confined within the furnace without much energy loss until there is an interaction with an absorber or the targeted sample (coupling). Hence, the energy transfer has much greater efficiency than most conventional heating methods, which employ radiant heating. Ordinarily, a dense metal part would not be expected to heat with microwaves. Thus, MW exposure

of the pack cementation process would most probably preferentially heat the bed containing the precursor source material and the halide activator. However, even in the metal parts there is some microwave absorption in the wear surface region. An estimate of the MW penetration (or skin depth) into a metal part during pack cementation can be made using the following equation:

$$\text{Skin Depth} = 5030\sqrt{\text{Resistivity}/(C \bullet \text{Frequency})}$$

As shown, the skin depth is dependent on the resistivity of the part and the MW frequency (C is a constant and is normally equal to 1). Thus, the approximate penetration depth at 2.45 GHz and a resistivity of 1×10^{-4} W·cm is on the order of 10 µm. Because the resistivity of most metals increases with temperature, the penetration depth should also increase as the temperature increases.

Microwave heating offers several advantages over conventional heating, mainly because it can selectively heat materials in a multicomponent system, creating a unique temperature profile. The potential advantages would include the following.

1. Because the temperature gradients will be higher than those in a conventional heating situation, the concentration gradient of the diffusing species into the component will also be steeper.[4] In most cases, this should increase the enhancement of surface properties and decrease the effects on bulk properties of the part being treated.
2. The process will be faster. Selective absorption of the MW energy will heat the packed bed rapidly to temperatures sufficient for the halide activator to operate. Conversely, because the surrounding insulation is cooler, the part should also cool faster. In addition, MW enhancement of diffusional processes in the near-surface regions, if any, would further improve the kinetics during the treatment.[5,6]
3. The bulk properties of the treated part will undergo only minimal alteration by thermal exposure. Since the process is faster, the parts are not subjected to the same high temperatures for extended periods of time as compared to the conventional heating situation. Consequently, less grain growth and other microstructural changes will occur that would affect the bulk properties.[7]
4. Microwave pack cementation should be safer and more environmentally friendly. With the heating confined to the volume directly surrounding the part to be treated, there should be less halide volatility and therefore less chance for halides being released from the reaction crucible. Also, because of the concentrated heat, it is possible that less halide activator will be required for the process. In addition, since the metal MW cavity is relatively cold, it acts as a getter for fumes, which may evolve during the reaction. Thus, noxious by-products will not be exhausted from the furnace.
5. Because the MW process is faster, safer, and less apt to change bulk properties, it will also be more efficient and economical on a total life cycle basis.

Some challenges do remain, though, including dealing with materials that poorly absorb MW power and controlling thermal runaway in samples that couple too well. Although the metal substrates used for pack cementation are expected to be MW reflectors,[8] the metal powders used as the source material are known to be excellent couplers of MW radiation.[8] Therefore, such heating problems are not expected for this project. However, due to possible shielding effects of the metal samples, it is difficult to predict the compositional and thermal uniformity. Furthermore, accurate measurement of temperatures in MW experiments has proven difficult historically due to temperature gradients that occur naturally in such processes.[9]

Technical Approach

For these experiments, we prepared cylindrical (1.25-cm diam × 1.25 long) and rectangular (1.25 cm × 1.25 cm × 1.25 cm). Three types of diffusion coating processes were chosen: aluminization, chromization, and boronization. For all three processs, the pack consisted of NH_4Cl as the activator and –325 mesh tabular aluminum oxide (Al_2O_3) as the filler. The depositing source materials (15 wt %) were aluminum metal powder (Al) for aluminization; chrome oxide (Cr_2O_3) for chromization; and boron carbide (B_4C) powder for boronization. After placing samples in the packing powder in an alumina crucible, the crucible was sealed with a ceramic paste and an alumina lid, heated to 100°C to set the glue, and evacuated and backfilled twice with argon. Loaded crucibles were heated at either 850 or 925°C for 4 h in flowing argon in either a 2.45-GHz MW furnace or in a conventional tube furnace. Control experiments were performed in which samples were heated in the alumina powder without the NH_4Cl activator and without the source powder. Processed and control samples were weighed and measured both before and after surface treatment. Control and processed samples were analyzed using optical microscopy, scanning electron microscopy, and energy dispersive X-ray spectroscopy (EDS). The hardness values of control and boronized samples were measured using both a nano-indentor and a micro-hardness testing device.

Results and Accomplishments

Aluminization Results

Aluminum-based coatings were successfully deposited on all three alloys using MW heating. Approximately 800 W of power was needed to maintain the temperature at 850 and 925°C for the 40 g of samples and the ~425 g of packing powder. Coatings were also deposited on all alloys using conventional heating. Figure 1 shows weight gain values obtained for the three metal alloys aluminized at 850 and 925°C using either MW or conventional heating. The results show that there was more aluminum deposited on the MW-treated samples at both temperatures. Scanning electron microscopic (SEM) examination of the samples was used to determine the extent of the aluminum diffusion into the samples. SEM examination (photos not shown) show that the aluminum coatings exist as both deposited and diffusion layers. Figures 2 and 3 show data generated from the SEM examination of both the A2 tool steel and the 1018 steel processed by either microwave or conventional heating at 850 or 925°C. The aluminized coatings were much thicker for the A2 and 1018 steel alloys processed to 925°C by MW heating. The data also shows that most of this coating was deposited, rather than diffusion, coating. Dimensional increases of up to 300 µm were observed. Aluminization of both alloys at 850°C yielded slightly thinner coatings; however, a larger percentage of the coatings exist as diffusion coatings, especially for A2 and 1018 samples processed using MW heating. This suggests that the deposition occurred rapidly at the higher temperature and effectively shielded the surface from MW interaction. On the other hand, at the lower temperature, the deposition was slower, so increased diffusion due the MW interactions of the aluminum could take place. Figure 4 shows a SEM micrograph for an A2 sample conventionally aluminized 925°C for 4 h. Figure 5 shows a SEM micrograph of a much thicker coating produced in an A2 sample aluminized using microwave heating at 925°C for 4 h. Note there was minor cracking in both the conventional and microwave coatings, possibly due to the large thickness of the coatings.

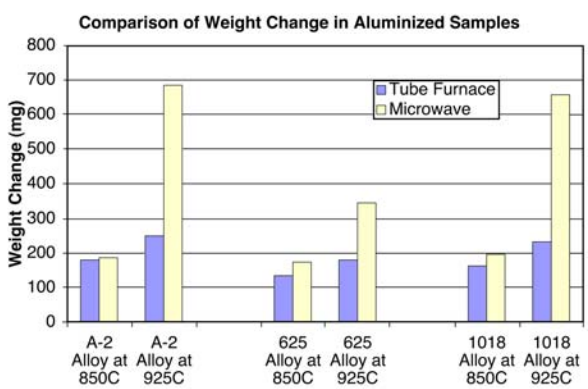

Fig. 1. Observed weight changes during aluminization.

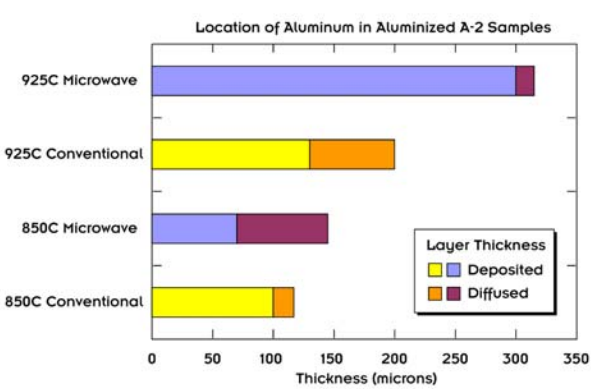

Fig. 2. Thickness of deposited and diffusion layers in aluminized A2 samples.

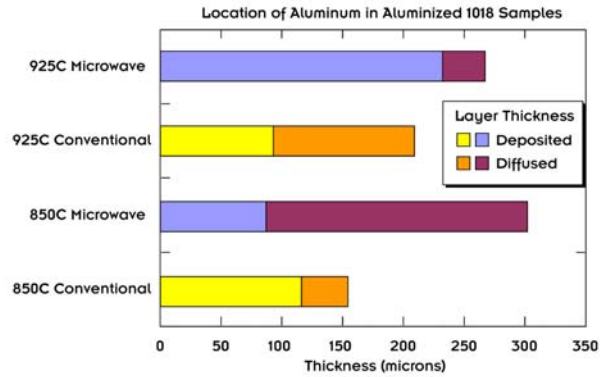

Fig. 3. Thickness of deposited and diffusion layers in aluminized 1018 samples.

According to collected X-ray diffraction (XRD) data, the A2 and 1018 alloys showed the formation of an Al_5Fe_2 phase in the deposited aluminum layer under all processing conditions except at 850°C in the MW furnace. However, since iron is an excellent absorber of copper K_a radiation, this data is only applicable to about the first 20 to 40 µm. Therefore, this conclusion may be slightly oversimplified. Although most of the backscatter electron (BSE) images reveal a compositionally homogenous layer, the 1018 sample conventionally aluminized at 925°C clearly has multiple phases. Hence, the Al_5Fe_2 phase seems to be favored when the pack is fully activated at these processing temperatures, although the formation of other phases is possible due to the temperature of concentration gradients. Structurally, this deposited layer seems highly prone to crack formation in both MW and conventional samples at 925°C. This probability for cracking decreases somewhat at 850°C but is not totally eliminated. According to Koo and Yu's work,[10] this cracking is the result of thermal expansion differences (not volumetric increases) and will lead to local corrosion attacks. Therefore, a shorter process

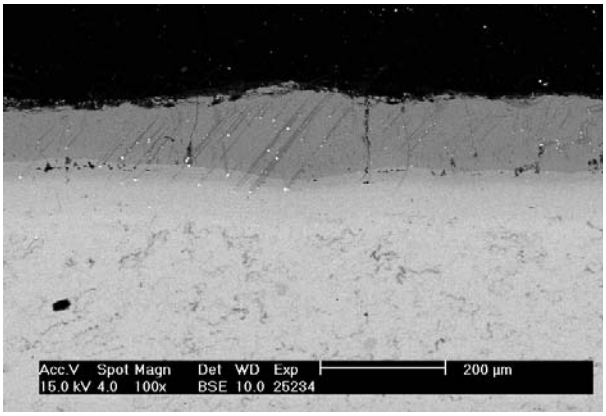

Fig. 4. SEM micrograph of A2 sample conventionally aluminized at 925°C for 4 h.

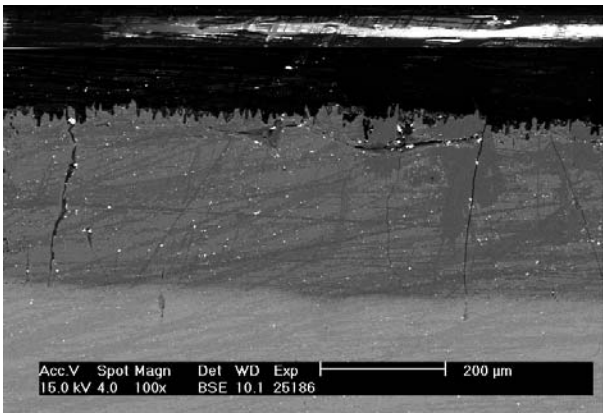

Fig. 5. SEM micrograph of A2 sample aluminized at 925°C with microwaves.

time is advisable for future aluminizing experiments. In comparing MW to conventionally heated samples, the largest structural difference is the tendency for porosity to form near the original surface of MW-processed samples. Unlike the 1018 samples, aluminized A2 samples tend to form chrome-vanadium carbide precipitates in the diffused region. Such precipitates were not observed in any of the control samples. Thus, this precipitation suggests that the diffused aluminum is forming a solid solution with the iron and making the formation of carbide thermodynamically favorable. These precipitates were observed in all aluminized A2 samples.

Chromization Results

Chrome-based coatings were successfully deposited on all three alloys using MW heating. Approximately, 600 W of power was needed to maintain the temperature at 850 and 925°C for the 40 g of samples and the ~450 g of packing powder. Coatings were also deposited on all alloys using conventional heating. Figure 6 shows the weight changes for the three alloys heated to either 850 or

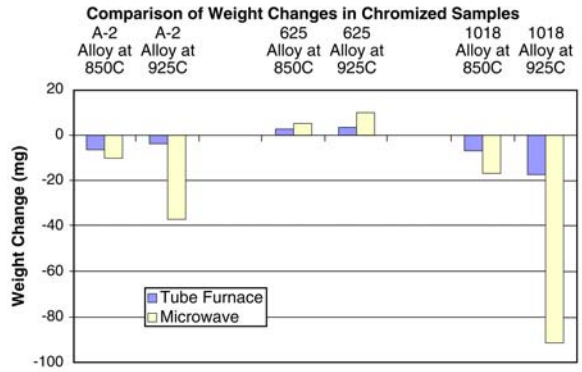

Fig. 6. Observed weight changes during chromization.

925°C using conventional and MW heating. The 625 nickel alloy gained a small amount of weight for both conventional and microwave processing. Weight losses were observed in the A2 and the 1018 alloys for samples processed by both conventional and microwave heating, with higher weight losses in microwave-heated parts. SEM analysis showed that the chromization of MW-treated pieces was better at the higher processing temperature; however, even at 925°C for 4 h, the diffusion layer was not as continuous as that observed in the conventionally heated samples. SEM analysis showed that the chrome appeared to diffuse into the first 2 to 10 µm at the samples surfaces. The MW samples appear to be less uniformly chromized. Unlike conventional samples that display a nearly continuous diffused chrome region near the surface, MW samples seem much more prone to show patches of chrome diffusion. A possible solution is substituting metallic chrome powder for the Cr_2O_3 source used in these experiments. The weight losses shown in Fig. 6 suggest iron volatilization from the surfaces. Energy dispersive X-ray (EDX) analysis indicated higher-than-normal iron concentrations near the surface of the chromized 625 nickel samples provide further evidence that iron volatilization from the other samples occurred during chromization of all three alloys. Chromized A2 and 1018 alloys display many similarities by XRD analysis. Typical phases found in these samples are Cr_7C_3 and Cr_2O_3. Once more, though, the MW samples treated at 850°C deviate significantly from this trend. Carbide formation was not unexpected, since it is a very stable phase, and often steels are aluminized first before chromization to prevent such a layer.[11]

Boronization Results

Boron-based coatings were successfully deposited on all three alloys using MW heating. Approximately, 350 W of power was needed to maintain the temperature at 850 and 925°C for the 40 g of samples and the ~350 g of packing powder. For control experiments, approximately

1050 W of microwave power was needed to maintain the temperature at 850 and 925°C with the alumina powder pack. Coatings were also deposited on all alloys using conventional heating. Very little changes in hardness changes were observed for the hardness at the surface of the 625 and 1018 alloys processed by microwave and conventional heating (data not shown). Since borides of iron or nickel are not very stable, this is not surprising. However, very interesting results were obtained for the A2 tool steel, where the alloying additive readily form borides. Figure 7 shows a graph of the nanohardness values for the A2 as-received material, A2 material processed in the tube furnace (TF), and A2 material processed in the MW furnace with alumina powder or with B_4C present. Both the MW controls heated in alumina powder alone and the A2 material heated in the B_4C pack using MW heating showed higher hardness values than the control untreated sample. Figure 8 shows a finer analysis of the near surface of the A2 samples processed in a tube furnace (top) or a microwave furnace (bottom). Due the size of the nano-indentor tip, one sees large hardness spikes as the tip hits hard and softer grains. Figure 9 shows micro-hardness hardness data for A2 alloy processed under several conditions. The microhardness tester was chosen to obtain a larger indent size, and thus a more average number is obtained than with the nano-indentor. The data shows the highest hardness for MW-treated samples packed in B_4C powder. The next two higher hardness levels were for A2 samples packed in alumina powder and processed conventionally and for A2 samples packed in alumina powder and processed using MW heating. The hardness values for the as-received A2 sample and the A2 samples processed in the tube furnace with B_4C powder were much lower. Figure 9 data suggests that there is a surface hardening effect with not only B_4C powder, but also the alumina powder with the A2 steel alloy. The fact that the A2 alloy heated in the MW transparent alumina powder bed was an unexpected result.

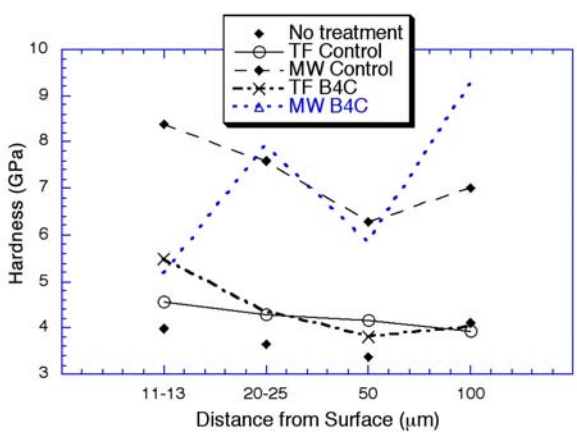

Fig. 7. Hardness as measured with a nano-indentor for as-received A2 steel, control samples heated in Al_2O_3, and samples treated in a B_4C pack at 925°C for 4 h using conventional (TF) and MW heating.

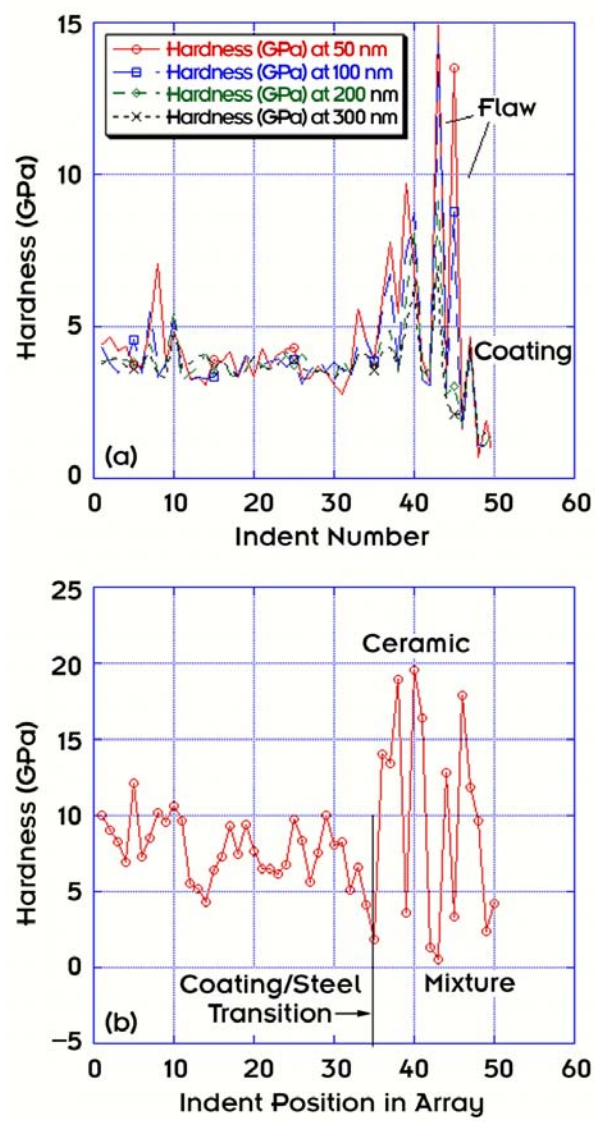

Fig. 8. Nano-indent hardness data for A2 alloy heated in a B4C pack at 925°C for 4 h by conventional (top) or MW heating (bottom).

Summary and Conclusions

Results of this broad, scoping project indicate that the MW heating shows strong potential as a method for surface treating alloys to obtain deeper diffusion of alloy elements into metal parts. Very low MW power is required to heat pack cement parts to 925°C. In addition, surprising results were obtained in control samples processed using MW heating in aluminum oxide, with no boron-hardening additive. These results indicate that microwave heating may be an additional method for surface hardening of metal

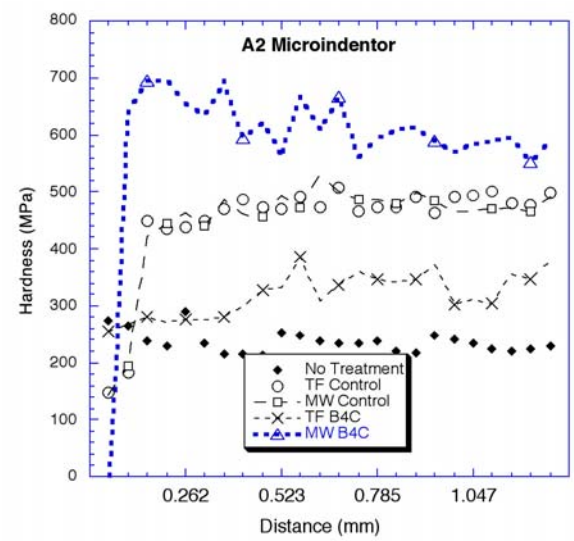

Fig. 9. Hardness as measured with a nano-indentor for an A2 alloy control sample and an A2 alloy sample heated using MW processing with B_4C packing at 925°C for 4 h.

parts. The work described has also led to an interest and FY 2003 funding provided by the Office of Energy Efficiency and Renewable Energy for pack cementation of ceramic parts for improved corrosion resistance.

References

[1]W. H. Sutton, "Microwave Processing of Ceramics—An Overview," pp. 33–38 in *Microwave Processing of Materials III.* MRS Symposium Proceedings Volume 269, Pittsburgh, 1992.

[2]R. Bianco, R. A. Rapp, and J. L. Smialek, "Chromium and Reactive Element Modified Aluminide Diffusion Coatings on Superalloys: Environmental Testing," *Journal of the Electrochemistry Society* **140**, 1191–1203 (1993).

[3]S. L. McGill et al., "Effects of Power Level on the Microwave Heating of Selected Chemicals and Minerals," pp. 247–252 in *Mater. Res. Soc. Symp. Proc.*, Vol. 124, Mater. Res. Soc., Pittsburgh, Pa., 1988.

[4]D. F. Stein et al., "Microwave Processing—An Emerging Industrial Technology," pp. 3–7 in *Mater. Res. Soc. Symp. Proc.*, Vol. 347, Mater. Res. Soc., Pittsburgh, Pa., 1994.

[5]S. J. Rothman, "Critical Assessment of Microwave-Enhanced Diffusion," pp. 9–18 in *Mater. Res. Soc. Symp. Proc.*, Vol. 347, Mater. Res. Soc., Pittsburgh, Pa., 1994.

[6]M. A. Janney et al., "Enhanced Diffusion in Sapphire During Microwave Heating," *J. Mat. Sci.* **32**, 1347–1355 (1997).

[7]Z. Xie et al., "Microwave Processing and Properties of Ceramics with Different Dielectric Loss," *J. Eur. Ceram. Soc.*, **19**, 381–387 (1999).

[8]D. E. Clark, W. H. Sutton, and D. A. Lewis, "Microwave Processing of Materials," pp. 61–96 in *Microwaves: Theory and Application in Materials Processing IV,* American Ceramic Society, Westerville, 1997.

[9]J. G. P. Binner and T. E. Cross, "Microwave Processing in the UK," pp. 33–28 in *Microwave Processing of Materials III.* MRS Symposium Proceedings Volume 269, Pittsburgh, Pa., 1992.

[10]C. H. Koo and T. H. Yu, "Pack Cementation Coatings on Ti_3Al-Nb Alloys to Modify the High-Temperature Oxidation Properties," *Surface and Coatings Technology* **126**, 171–180 (2000).

[11]Z. Minhui and R. A. Rapp, "Simultaneous Aluminizing and Chromizing of Steels to Form $(Fe, Cr)_3Al$ Coatings," *Oxidation of Materials* **49**, 19–31 (1997).

Ultrasonic Processing of Ultrafine Materials

Q. Han,[1] C. L. Xu,[2] G. R. Romanoski,[1] D. T. Hoelzer,[1] M. M. Menon,[3] and R. P. Taleyarkhan[4]
[1]*Metals and Ceramics Division*
[2]*University of Tennessee*
[3]*Nuclear Science and Technology Division*
[4]*Engineering Science and Technology Division*

High-intensity ultrasonic energy can be used to produce oscillating strain/stress fields in solid materials. The purpose of this seed money project was to explore novel use of the strain/stress induced by ultrasonic vibration for the production of ultrafine materials. Two new approaches have been developed conceptually and tested experimentally. The first approach was to use ultrasonically induced strain/stress to induce plastic deformation in materials. The second approach was to use ultrasonically induced oscillating stress fields to induce repeated phase transformation in the solid materials. Initial experimental results indicate that, for the first time, nanostructures are formed in the ultrasonically treated metal. The size of the nanostructures obtained using the first approach is smaller than 200 nm and possibly in the range of 100 nm.

Introduction

Nanostructured materials offer unique and entirely different mechanical, electronical, optical, and magnetic properties compared with conventional micro- or millimeter-sized materials. In metals, for example, the hardness of nanocrystalline copper increases with decreasing grain size, and 6-nm copper grains show five times the hardness of conventional copper.[1] Nanosized Al-Ni-In alloys exhibit a tensile strength larger than 1200 MPa, greater than conventional high-strength aluminum alloys.[2] Nanostructured M50 steel is more fatigue and fracture resistant than conventional M50 steel that is widely used in the aircraft industry as the main-shaft bearings in gas turbine engines.[3] In semiconductors, nanoclusters are often referred to as quantum dots, nanocrystals, and Q-particles. As an example, quantum dots can be developed to emit and absorb a desired wavelength of light by changing the particle diameter. This feature allows the construction of a finely tunable and efficient semiconductor laser.

Traditional methods for producing nanostructured materials include gas atomization and ball milling, followed by consolidation and rapid solidification.[4–6] These processes tend to be expensive and capable of producing only small amounts of material. Recently approaches for producing nanostructured materials include severe plastic deformation.[7–8] equal channel angular extrusion (ECAE) is one of the methods that uses severe plastic deformation to produce nanostructured materials, but the size of the sample is limited due to the high friction forces that exist between the material and the wall.[9] These developments suggest that methods that can produce severe plastic deformation have the potential in the production of nanostructured materials.

Ultrasonic vibrations produce oscillating strain and stress fields in solid materials.[10] Experiments have shown that ultrasonic vibrations above a critical intensity increase the concentration of dislocations and point defects in the solids. The density of the defects increases with increasing ultrasonic intensity. When the density of the dislocations is high enough, an alignment of dislocations occurs. It has been observed that a distinct cellular structure, about 2 μm in size, is formed in ultrasonically treated aluminum monocrystals after it was exposed to ultrasonic vibration for only 8 s.[11] The experimental evidence suggests that ultrasound is a powerful tool in producing severe plastic deformation in solid materials. However, the grains size was still a few orders of magnitude larger than the size of nanostructures. Also the oscillating nature of the strain and stress induced in solid metal by ultrasonic vibrations is not explored for grain refinement.

The purpose of this research was to investigate the possibility of producing nanostructures in metals using ultrasonic vibrations. Two new approaches have been developed conceptually and tested experimentally. Initial experimental results indicate that, for the first time, nanostructures are formed in the ultrasonically treated metal. The size of the nanostructures obtained using the first approach is smaller than 200 nm and possibly in the range of 100 nm.

Technical Approach

The First Approach

The idea in the first approach was to use the ultrasonically induced strain/stress to enhance dislocation and vacancy densities in metal in the hope that the line/point defects can align themselves to form ultra-fine structures. Extruded 1010 steel was used, and the initial grain size in the steel was about 10 μm. A 20-kHz, 1.5-kW ultrasonic unit was used for the experiments. Initially ultrasonic energy was directly injected into steel bars. No substantial grain refinement was observed, and the bar fractured due to fatigue. This was because in an oscillating stress field, the stresses are periodic (positive and negative). Usually materials fracture more easily under tensile stress.

A novel approach was then developed to offset the instantaneous tensile stress induced by ultrasonic vibration. High-intensity ultrasonic energy was then focused on specific locations in the specimen for 60 s, resulting in a severe plastic deformation in those locations. The deformed region was polished, etched, and characterized using scanning electron microscopy (SEM) and transmission electron microscopy (TEM).

The Second Approach

The idea in the second approach was to inject acoustic energy into metal at its solid/solid phase transformation temperature such that the oscillating stress generated by ultrasonic vibration may lead to a repeated phase transformation at high frequency. The solid/solid phase transformation temperature varies with external stress. Under the influence of oscillating stress, the phase transformation temperature will also oscillate around its equilibrium temperature. When the specimen under acoustic vibration is held at the equilibrium solid/solid phase transformation temperature, oscillating undercooling occurs for both phases, which may result in repeated nucleation for both of the phases involved. Since the diffusion coefficient in the solid state is very small, the growth rate of the newly formed phase will be small, and the grain size of the newly formed phase will be mainly determined by the nucleation stage of the phase transformation.

In the second approach, bar specimens were made out of 1010 steel and placed in a furnace with a known temperature gradient. The temperature was 1000°C at one end of the specimen and was room temperature at the other end to ensure that the α to γ phase transformation occurred at a certain location in the specimen. Ultrasonic energy was then injected into the specimen for 5 to 20 s until the specimen was quenched in water to preserve the grain size at high temperatures.

Results and Accomplishments

Ultrasonically Induced Plastic Deformation

Sever plastic deformation occurred in the specific location of specimen injected with high-intensity ultrasonic vibration under compressive stress. Optical microscopy revealed that the original α grains were severely deformed into thin strips. The SEM image shown in Fig. 1 indicates that the strips are narrower than 200 nm. Within each nanosized strip, a large number of small features/grains in the neighborhood of 200 nm can be barely seen.

Figure 2 is a TEM image showing the size of the nano particles/grains. A few particles less than 200 nm can be clearly seen. On the top side of the image, dislocation densities are extremely high, indicating that severe deformation occurred in those locations.

Results shown in Figs. 1 and 2 indicate that grain size smaller than 200 nm have been obtained by injecting ultrasonic energy into 1010 steel specimens. By using ultrasonic vibrations, the smallest grain size never before obtained is 200 nm. The grain sizes are in the nanosize scale, and it was one of the objectives of this project.

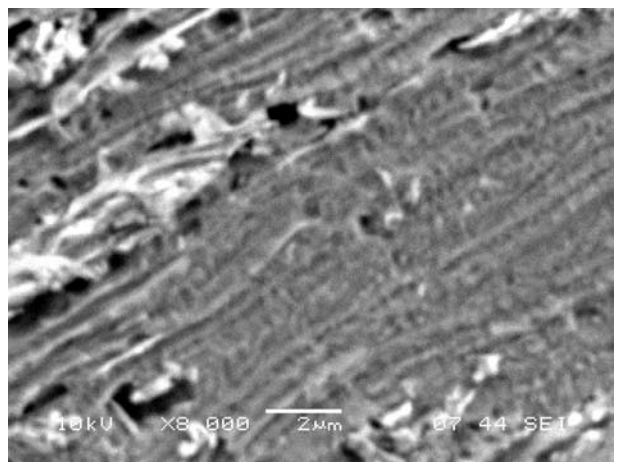

Fig. 1. An SEM image of the severely deformed region in the 1010 steel specimen. The fine strips are the deformed α phase, and the coarse structure are the pearlite. Most of the fine strips are narrower than 200 nm and contain a large number of particles smaller than 200 nm.

Repeatedly Induced Phase Transformation

Results obtained in the second approach were not as anticipated. When ultrasonic energy was injected into the test bar (~1.9 cm diam), the specimen was quickly broken at the location corresponding to the δ to γ phase transformation (A3 temperature). This phenomenon, which was not reported before, might be related to the volume change during repeated δ–to-γ phase transformation at high frequencies.

In order to observe the microstructure at the δ–to-γ phase transformation, the specimen was quenched before

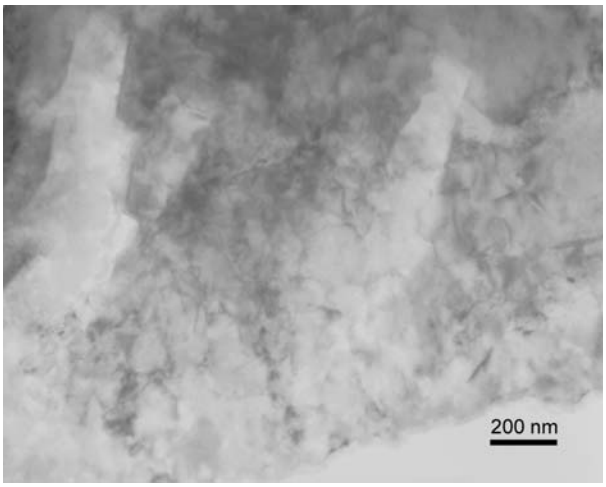

Fig. 2. A TEM image showing particles smaller than 200 nm in the severely deformed region. The dark areas on the image contain a large number of dislocations.

being broken. Figure 3 shows the microstructure of the quenched specimen. Parallel plates like those of martensite structure occurred in the specimen. Fractures can be observed at the grain boundaries. Adjacent to the cracks, a large number of nanosized features/grains exist, which has also not been reported before. It looks as if the δ–to-γ phase transformation occurred only at the grains boundaries, and the reactions didn't reach to the center of the previous α grains before cracking occurred.

Although bulk nanostructures were not really obtained in this approach, two nanosized features were observed: one occurred at the grain boundaries adjacent to the cracks, and the other was the two-dimensional parallel plates, which might be martensite.

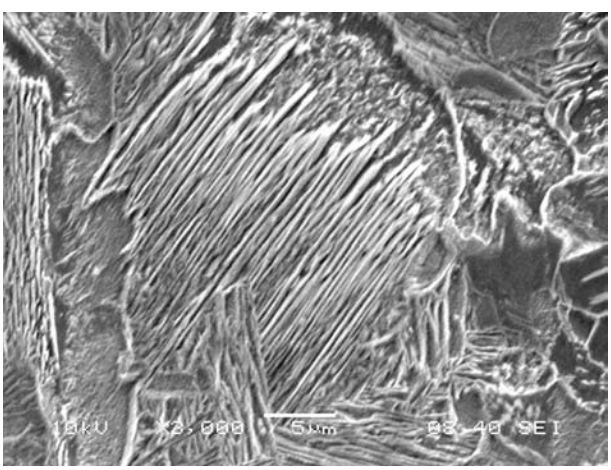

Fig. 3. A TEM image showing the microstructure in the quenched specimen. The specimen was subject to ultrasonic vibrations for 15 s at its α–to-γ phase transformation temperature before quenching. Cracking occurred along the grain boundaries.

Summary and Conclusions

Nanostructures have been obtained in 1010 steel using ultrasonically induced severe plastic deformation. The size of the grains in the severely deformed regions is smaller than 200 nm.

The experiments on repeated phase transformation induced by ultrasonic vibration revealed some new phenomena not reported in the open literature. Fine, nanosized grains occurred near the grain boundaries. Parallel nanoplates form during quenching of 1010 steel injected with ultrasonic energy.

The project results have the potential for scaling up for the production of critical metal components for transportation and defense applications, leading to energy savings. Contact will be made with DOE and DOD program managers for future funding to continue this work.

References

[1]H. S. Nalwa, *Handbook of Nanostructured Materials and Technology*, ed. H. S. Nalwa, Academic Press, 1996, p. ix.

[2]K. Kita, K. Saito, A. Inoue, and T. Matsumoto, *Mater. Sci. Eng.* **A226–228**, 1004 (1997).

[3]K. E. Gonsalves, S. P. Rangara, and J. Wang, *Handbook of Nanostructured Materials and Technology*, ed. H. S. Nalwa, Academic Press, 1996, p. 27.

[4]R. W. Seigel, *MRS Bulletin* **15**, 60 (1990).

[5]M. Umemoto, Z. G. Liu, and K. Masuyama, *Scripta Mater.* **44**(8–9), 1741–45 (2001).

[6]I. G. Brodova, D. V. Bashlykov, and A. B. Manukhin, *Scripta. Mater.* **44**(8–9), 1761–64 (2001).

[7]I. V. Alexandrov and R. Z. Valiev, *Scripta Mater.* **44**(8–9), 1605–08 (2001).

[8]I. Altenburger, B. Scholtes, and V. Martin, *Mat. Sci. Eng.* **A264** (1–2), 1–6 (1991).

[9]K. Zhang, I. V. Alexandrov, and K. Lu, *Nanostruct. Mater.* **9**(1–8, 347–350 (1997).

[10]O. V. Abramov, High-Intensity Ultrasonics Theory and Industrial Applications, Gorden and Breach Science Publishers, Singapore, 1998.

[11]B. Langenecker, *Proc. High Power Ultrasonics*, 1971, p. 32.

Compound Semiconductors on Silicon: Shedding Some Light on the Matter

O. W. Holland,[1] B. C. Larson,[1] D. B. Beach,[2] and M. F. Chisholm[1]
[1]*Condensed Matter Sciences Division*
[2]*Chemical and Analytical Sciences Division*

The integration of lattice-mismatched material onto Si wafers is key to increasing the functionality of integrated circuits and, in particular, to integrating both optical and digital processing on a single chip. A method is proposed which is capable of providing a growth template on Si for films with a lattice mismatch of ≤4%. It involves implantation of Ge into Si to form a dilute solid solution. Enrichment is achieved by thermal oxidation of the implanted layer to snowplow the Ge ahead of the growing oxide interface to form a uniform pseudomorphic SiGe film. The composition of the film (and thus the lattice parameter) can be varied from pure Ge to Si rich by adjusting the oxidation conditions. Once formed and relaxed to its natural lattice spacing, the SiGe film is an ideal template for growth of defect-free GaAs and/or strained-layer SiGe layers. Methods of achieving this relaxation without plastic deformation are discussed.

Introduction

Silicon, an indirect bandgap semiconductor, is well suited for digital electronics but is an inefficient emitter of light. Many III-V compound semiconductors such as GaAs have a direct bandgap and, as such, are ideally suited for optical applications. However, the lattice mismatch (4.1%) between silicon and GaAs is too large for growth of defect-free, oriented, single-crystal films. Ge is lattice matched to GaAs and can be grown on Si by a number of deposition techniques, but the large misfit results in the creation of misfit dislocations, which partially relieve the strain. Dislocations that thread through the film have the potential to severely degrade the optical and electrical integrity of any material grown on this layer.

Technical Approach

The proposed process involves sequential Ge^+-implantation and thermal oxidation of the top Si layer in silicon-on-insulator (SOI) material. Implantation initially yields a dilute SiGe mixture in the near surface that is progressively Ge enriched during oxidation until it forms a distinct pseudomorphic GeSi-layer on the Si substrate. The method relies on the complete rejection of the implanted Ge from the oxide during growth. This segregation results in the formation of a distinct Ge-rich layer at the interface that is epitaxially oriented on the underlying Si. A method is demonstrated for relaxing the strain in the Ge layer without plastic deformation so that it can be used as an intermediate layer to facilitate growth of lattice mismatched films on Si. The process involves decoupling the Ge layer from the Si substrate by using SOI material. The material consists of a buried oxide layer (BOX) beneath the surface that isolates a top Si layer from the bulk Si. In general the Ge layer formed by this process is biaxially strained near the lattice parameter of Si. The temperatures involved in the oxidation of Si may allow the germanium layer to partially relax to its natural lattice spacing (i.e., as a result of viscoelastic flow of the SiO_2 or buckling of the thin Ge film). Further relaxation of the film has was achieved by ion irradiation without misfit dislocation formation.

This process is substantially different from other growth techniques that generally achieve layer-by-layer growth by atomic attachment at a free surface. The proposed two-step process is more akin to a bulk process in that it does not involve a free surface (although it does depend on a interfacial boundary), and it achieves layer formation by enrichment rather than by an adatom process. These differences offer substantial benefits in forming strained layers that yield a greater thermal stability (against relaxation) and, thus, different pathways or mechanisms for relaxation. The thickness of the pseudomorphic Ge-rich layers formed by this technique has been shown to far exceed the critical value established by Matthew[1] (i.e., the thermodynamic limit). The kinetic barrier for forming misfit dislocations is sufficiently great that relaxation generally occurs only when the elastic strain within the pseudomorphic film far exceeds its critical value (i.e., where dislocation formation is energetically favored). Thus, studies have shown that the onset of misfit formation can only occur as a result of nonhomogeneous strain with the layer. Such is the cause when growth involves a free surface that can develop morphological instabilities. It has been shown that such instabilities (i.e., roughening) redistribute the strain within the film to produce localized

strain that is capable of nucleating misfit growth. Thus, the absence of a free surface and the inherent stability against roughening in the layers formed by the proposed technique is considered to be responsible for its substantial benefits over other techniques.

Results and Accomplishments

Cross-section, transmission electron micrographs (XTEM) in Fig. 1 show a SiGe film formed by this technique. The sample shown is an SOI wafer implanted with Ge at 80 keV at a dose of $5 \times 10^{16} cm^{-2}$. It was oxidized in dry O_2 in several stages. An initial cycle of 1150°C/3 h was used followed by a 1050°C cycle and a final cycle at 930°C. The oxidation temperature was decreased as the Ge content of the film increases to avoid melting (which occurs at 934°C for pure Ge). These oxidation cycles removed most of the top Si layer and left only a well-defined SiGe layer encapsulated between the thermal oxide (on the top) and the buried oxide (BOX) of the SOI. Both the bright-field image in Fig. 1(a) and the dark-field image in Fig.1(b) demonstrate that partial relaxation of the film (~50%) has occurred by dislocation formation. Interestingly, both micrographs indicate that the segregated film has bifurcated into a Ge-rich layer at the top and a Si-rich layer at the bottom. Threading dislocation segments can be seen originating from the bilayer interface. The results demonstrate that the viscoelastic response of the BOX is insufficient to accommodate the strain in the SiGe film. These results are consistent with those by Hobart,[2] who reported relaxation in a compressively strained SiGe film bonded to a borophosphorosilicate glass by buckling. Buckling was avoided by patterning the film into small areas prior to annealing (i.e., relaxation).

It is clear that another technique is required to achieve defect-free relaxation of the segregated film. XTEM of a sample that was processed similarly to the one previously discussed is shown in Fig. 2. It is clear from the figure that the SiGe film (estimated to be 70% Ge) is quite uniform in thickness with planar interfaces at both oxide layers. There is no indication of bifurcation within the film. An inspection across the entire field of view (~several microns) within the microscope failed to find any dislocations within the film. This yields a rough estimate for the upper limit for threading dislocations density of $\sim 10^7 cm^{-2}$. The main difference in processing of this sample compared to the one shown in Fig. 1 was that it was irradiated (with 200 keV Si^+ ions) prior to the final oxidation cycle at 900°C in an attempt to promote relaxation within the Ge layer. While no additional relaxation was observed compared to a non-irradiated control, the ion mixed sample achieved a 50% relaxation of the in-plane spacing without plastic deformation (i.e., no misfit dislocations), while a high dislocation density was observed in the control sample.

The use of energetic ions to promote relaxation of highly strained, pseudomorphic films offers an innovative method to form dislocation-free, relaxed films. The effect derives from the ability of the energetic ions to transfer sufficient energy to the Ge atoms in the film to physically remove them from the film. This ballistic effect is shown pictorially in Fig. 3. The biaxial compressed film is relaxed by the physical removal of excess Ge atoms in the film, which allows the film to relax to its natural lattice spacing.

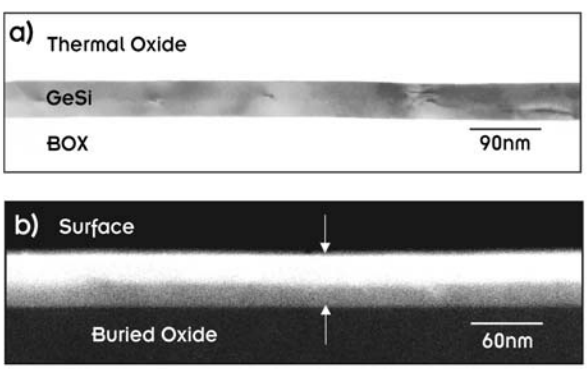

Fig. 1. XTEM micrograph of a Ge-rich film encapsulated within a SOI material by a buried oxide (BOX) and a superficial thermal oxide at the surface. The SOI was implanted with 80 keV Ge^+-ions at a fluence of $5 \times 10^{16} cm^{-2}$. (a) Bright field image revealing a dislocation array near the centerline of the film with threading segments spanning to the top and bottom interface. (b) z-contrast image showing bilayer: top 24 nm of film is Ge rich compared to bottom 16 nm. Viscoelastic response of the oxide substrate (BOX) is insufficient for large area films to achieve defect-free relaxation of the encapsulated film. Strain relaxation is observed, but it appears to be predominantly due to misfit dislocation formation.

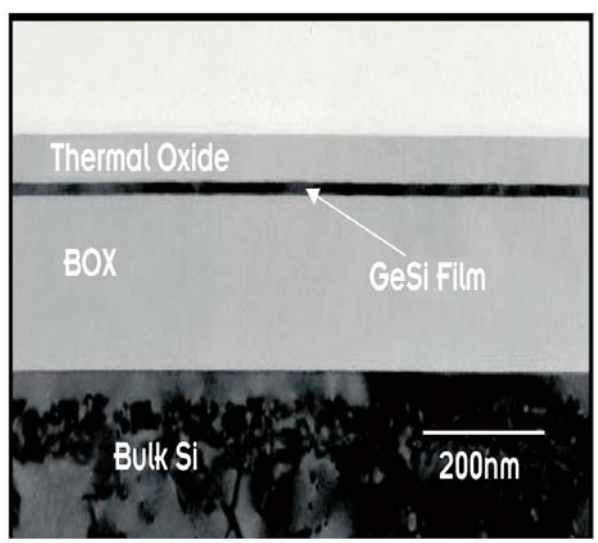

Fig. 2. XTEM of a continuous 15 nm $Si_{0.3}Ge_{0.7}$ film with no dislocations by inspection over a wide area.

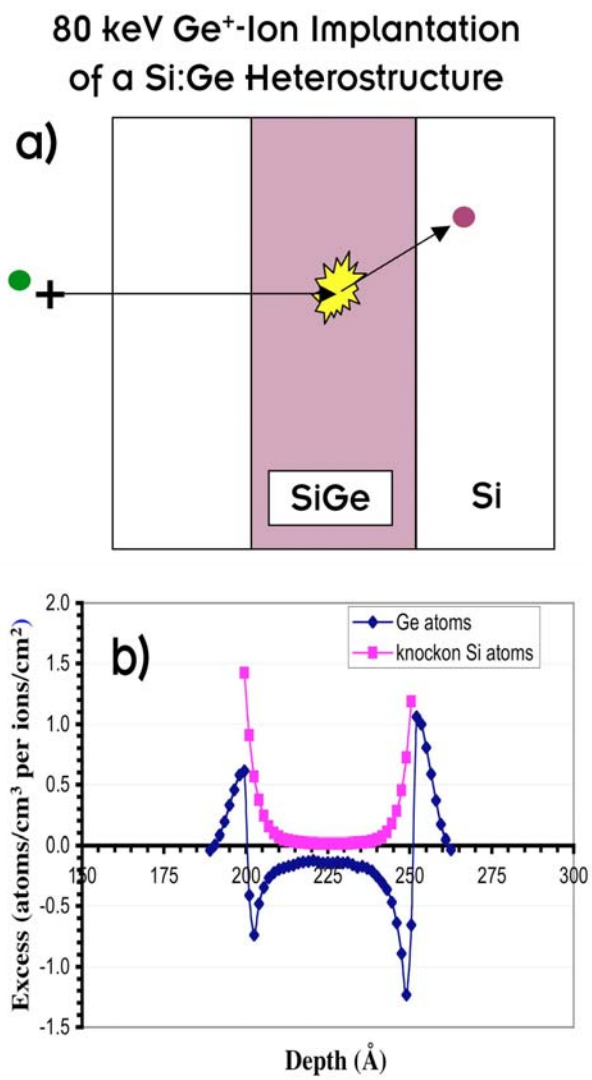

Fig. 3. (a) Ballistic rarefaction of Ge film by ion implantation, and (b) TRIM simulation of rarefaction process demonstrating the ability of energetic ions to ballistically remove atoms from the film to allow it to relax without dislocation formation.

Results of a computer simulation of this process are also shown in Fig. 3. The simulation shows that, although Ge atoms are removed from the film, Si atoms are knocked into the film. However, the process strongly favors removal of Ge atoms due to the larger scattering cross section of the ions with the higher atomic number. Simulation results show that complete relaxation can be achieved at a dose of ~10^{16}cm^{-2}.

Summary and Conclusions

A method of forming a dislocation-free, relaxed Ge layer on SOI was demonstrated. The method involved Ge^+-implantation and thermal oxidation to form a thin, pseudomorphic Ge layer in SOI. Relaxation of the segregated Ge film was achieved using a ballistic effect due to the interaction of energetic ions with the Ge atoms. The partial relaxation of the film was achieved without any plastic deformation in the film. Fully optimized, this technique should be capable of achieving almost full relaxation of the Ge films, which will permit integration of defect-free GaAs and other III-V films onto Si substrates.

This project explored methods of relaxing strained thin films without plastic deformation (dislocations). An innovative technique involving the use of energetic ions to promote relaxation was discovered to produce 50% relaxation of the strain without the introduction of dislocations. While the method is rather specialized, the principal benefit will be increased understanding of strain relaxation in thin films. This improves the basic science foundation of the DOE and other programs that rely on the integration of lattice mismatched film/substrate systems.

References

[1]J. W. Matthews and A. E. Blakeslee, *J. Cryst. Growth (Netherlands)* **27**, 118 (1974).

[2]K. D. Hobart, F. J. Kub, M. Fatemi, M. E. Twigg, P. E. Thompson, T. S. Kuan, and C. K. Inoki, *Journal of Electronic Materials* **29**, 897 (2000).

Ferromagnetism in Dilute Magnetic Semiconductors: Getting to the Science with Neutron Scattering

B. C. Sales,[1] D. Mandrus,[1] H. A. Mook, Jr.,[1] L. A. Boatner,[1] and T. C. Schulthess[2]
[1]*Condensed Matter Sciences Division*
[2]*Computer Science and Mathematics Division*

This project focused on the growth and characterization of single crystals of dilute magnetic semiconductors (DMS). DMS are one of the key components in the next generation of electronic devices that make use of the electron spin as well as its charge. The origin of the ferromagnetism in DMS is not well understood, in part because virtually all of the DMS have been prepared in thin film form using nonequilibrium synthesis methods. Single crystals can be studied with a larger variety of experimental methods, including neutron scattering. A large number of magnetically doped single crystals were prepared during the early stages of this project (chalcopyrites, ZnO, $KTaO_3$, Ge, and TiO_2—doped with Mn, Co, and Fe). Initial studies on these crystals indicated that much of the room-temperature ferromagnetism reported in the literature was due to clustering and/or an impurity phase. To avoid clustering, we have grown and started to characterize large crystals (≈0.7 g) of a stochiometric DMS: $Yb_{14}MnSb_{11}$. In this ferromagnetic compound, all of the Mn atoms are located at a well-defined crystallographic site, and hence there is no problem with clustering. $Yb_{14}MnSb_{11}$ and related compounds appear to be ideal materials on which to unravel the magnetism in DMS. Because of the extra work involved in showing that earlier studies were incorrect, neutron scattering experiments were not conducted as part of this seed money. However, the $Yb_{14}MnSb_{11}$ materials were shown to be extremely interesting and DOE Basic Energy Sciences funding has been redirected to fund neutron scattering experiments that are currently in progress.

Introduction

"Until recently, the spin of the electron was ignored in mainstream charge-based electronics. A technology has emerged called spintronics (spin transport electronics or spin based electronics), where it is not the electron charge but the electron spin that carries information, and this offers opportunities for a new generation of devices combining standard microelectronics with spin-dependent effects that arise from the interaction between the spin of the carrier and the magnetic properties of the material."[1] This quote from a recent review article in *Science* summarizes the emerging field of spintronics that includes everything from spin valves to quantum computing. This is a vast new area of science and technology that has already resulted in new read heads for computer hard drives (based on a spin valve)[1] and the first demonstration of a primitive quantum computer.[2]

One of the key components in the next generation of proposed spintronic devices is a ferromagnetic semiconductor that can be used as a source of current in which the spins of the carriers are highly polarized.[1,3] The recent observation of ferromagnetism near room temperature in semiconductors containing a few percent of magnetic atoms was a surprise and is not well understood.[4,5] To date, all of the DMS have been prepared in thin-film form using nonequilibrium synthesis methods. Neutron scattering is the most powerful technique for probing and understanding magnetism in a solid, but it does not have enough sensitivity to study a DMS thin film. The goal of this project is to identify and prepare one or more DMS as a large single crystal (>1 mm^3) suitable for neutron scattering investigations.

Technical Approach

A large number of different materials were grown as single crystals based on various reports in the literature. These reports usually indicated the observation of ferromagnetism in a thin-film semiconductor doped with a few percent of a magnetic element such as Co, Mn, or Fe via a nonequilibrium method. Based on these reports, we prepared crystals of the following materials:

1. ZnO doped with Mn or Co (Crystals were grown via vapor transport in a sealed silica tube at temperatures between 600–800°C using NH_4Cl as a transport agent.)
2. Ge doped with Mn (Crystals grown by slow cooling of melt in a silica crucible from 1100°C or by quenching the melt to room temperature followed by annealing.)

3. $CdSiP_2$ doped with Mn (Phosphides with the chalcopyrite structure were grown from a molten tin flux. The excess tin was removed from the crystals using a centrifuge.)
4. $ZnSnAs_2$ doped with Mn (Arsenides with the chalcopyrite structure were grown by pre-reacting the elements in a sealed silica tube at 600°C followed by melting at 1150°C and slow cooling.)
5. TiO_2 crystals doped with Co (Small doped crystals of TiO_2—anatase structure—were grown via vapor transport.)
6. $KTaO_3$ doped with Mn, Fe, Co, and Ni (Large crystals of doped $KTaO_3$ were grown using a self-flux method.)

Preliminary structural, magnetic, and electrical measurements were made on all of the crystals listed above. We found no evidence of ferromagnetism in any of the magnetically doped semiconducting crystals. In some of the materials (such as $KTaO_3$), the equilibrium solubility of magnetic elements in the structure was too low (0.1–0.3%); in others (ZnO), the coupling between the magnetic elements was too weak to produce ferromagnetism above 4 K. In several of the crystals (Ge: Mn and $ZnSnAs_2$: Mn), ferromagnetism could be traced to a metallic impurity phase.

The disappointing results discussed in the previous paragraph indicated a need to change our technical approach. The problem of clustering and/or impurity phases in a semiconducting host could be eliminated if we could find a ferromagnetic semiconducting compound where all of the magnetic ions are at well-defined but widely separated crystallographic sites. The physics of the magnetism in such a compound would also be much easier to study using neutron scattering. David Mandrus pointed out that there is indeed such a class of materials, the Zintl compounds such as $Ca_{14}MnSb_{11}$. These semiconductors are ferromagnetic at about 60 K,[6] contain only 3.8 at. % of the magnetic element Mn, and the Mn ions are at well-defined crystallographic sites that are separated by at least 1 nm.

Results

We have been able to grow large crystals (0.7 g) of the Yb member of this family of materials ($Yb_{14}MnSb_{11}$) from a Sn flux.[7] This compound crystallizes in the tetragonal $Ca_{14}AlSb_{11}$ structure-type, $I4_1/acd$ space group (Z = 8) with a = 16.61 Å and c = 21.95 Å. $Yb_{14}MnSb_{11}$ has 208 atoms in the unit cell and contains only 3.8 at. % Mn. The Yb is divalent in this compound and hence is not magnetic. A photograph of one of the flux-grown crystals is shown in Fig. 1. Magnetic susceptibility and magnetization data from one crystal (Fig. 2) clearly demonstrate that this compound is ferromagnetic below

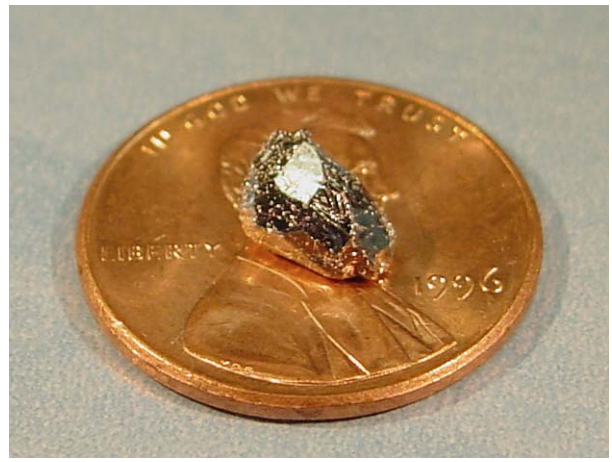

Fig. 1. Flux grown crystal of $Yb_{14}MnSb_{11}$.

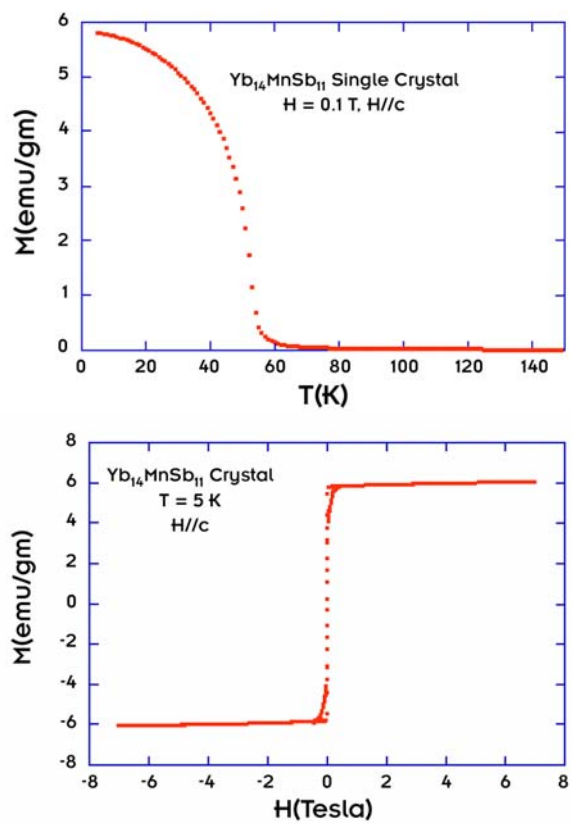

Fig. 2. Magnetic susceptibility (top) and magnetization data (bottom) from a $Yb_{14}MnSb_{11}$ crystal. The ferromagnetic transition at $T_c \approx 55$ K is clearly evident.

about 55 K. The magnitude of the saturation magnetization corresponds to a magnetic moment of about 4 μ_B per Mn. The electrical resistivity of undoped $Yb_{14}MnSb_{11}$ crystals is about 1 mΩ-cm at room temperature, which is indicative of a heavily doped semiconductor. Although we have still not unambiguously measured the carrier concentration in this material, we have determined from doping studies that

the dominant carriers are holes. We have grown single crystals of La-doped $Yb_{14}MnSb_{11}$ and Te-doped $Yb_{14}MnSb_{11}$. Both of these dopants should increase the concentration of electrons. Since the Curie temperature,

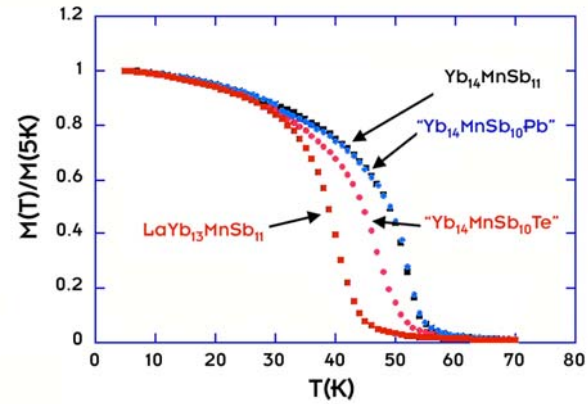

Fig. 3. Normalized magnetization data from undoped and doped crystals of $Yb_{14}MnSb_{11}$. Electron doping with La or Te lowers T_c and suggests that holes are the dominant carriers in $Yb_{14}MnSb_{11}$.

T_c, decreases with La or Te additions, it is likely that the overall carrier concentration has decreased, suggesting that holes are the dominant carriers. The decrease of T_c with electron doping is shown in Fig 3.

Summary and Conclusions

A large number of crystals were grown in an attempt to duplicate many of the claims in the literature concerning the existence of DMS. Several claims of DMS in bulk materials (Ge:Mn for example) were found to be due to impurity phases and poor science. For other material systems, we found that equilibrium crystal growth was not able to duplicate results found in thin films prepared using nonequilibrium methods. Either the solubility limit of various magnetic elements in the semiconducting host was too low to induce ferromagnetism ($KaTaO_3$: Mn for example) or the carrier concentration could not be increased enough to couple the magnetic moments to each other (ZnO: Mn for example).

We found that a more successful approach was to prepare single crystals of an unusual class of ferromagnetic semiconducting compounds where all of the magnetic ions are at well-defined but widely separated crystallographic sites: $Yb_{14}MnSb_{11}$ or $Ca_{14}MnSb_{11}$ for example. We found we could grow relatively large crystals (0.7 g) of $Yb_{14}MnSb_{11}$ and could change the carrier concentration through doping on one of the non-magnetic sites (Yb or Sb sites) with La or Te. This system appears to be ideal to investigate the physics of carrier-mediated ferromagnetism, a phenomenon that is at the heart of all DMS materials envisioned for spintronic applications. Because these new materials were discovered near the end of the seed money project, there was no time for neutron scattering experiments. However, the initial results from the $Yb_{14}MnSb_{11}$ were so interesting that DOE Basic Energy Science funding has been redirected to study these materials and neutron scattering experiments are currently in progress.

References

[1]S. A. Wolf, D. D. Awschalom, R. A. Buhrman, J. M. Daughton, S. von Molnar, M. L. Roukes, A. Y. Chtchelkanova, and D. M. Treger, *Science* **294**, 1488 (2001).

[2]L. M. K. Vandersypen, M. Steffen, G. Breyta, C. S. Yannoni, M. H. Sherwood, and I. L. Chung, *Nature* **414**, 883 (2001).

[3]S. Das Sarma, J. Fabian, X. Hu, and I. Zutic, *Solid State Commun.* **119**, 207 (2001).

[4]H. Ohno, A. Shen, F. Matsukura, A. Oiwa, A. Endo, S. Katsumoto, and Y. Iye, *Appl. Phys. Lett.* **69**, 363 (1996).

[5]T. Dietl, H. Ohno, F. Matsukara, J. Cibert, and D. Ferrand, *Science* **287**, 1019 (2000).

[6]J. Y. Chan, M. N. Olmstead, and S. M. Kauzlarich, *Chem. Mat.* **10**, 3583 (1998).

[7]I. R. Fisher et al., *Phys. Rev. B.* **59**, 13829 (1999).

Growth of MgB_2 Thin Films for Superconductor Applications

T. M. Besmann, A. Goyal, and D. M. Kroeger
Metals and Ceramics Division

The recent discovery of the superconducting properties of MgB_2 has stirred significant scientific and technological interest. Films of MgB_2 have potential advantages over oxide superconductors in their applicability to Josephson Junctions and as high-power, medium-temperature superconductor wires and tapes. A major issue in the use of the material is its fabrication in a cost-effective manner. While a number of attempts to produce films have been successful, they all use very expensive, low-throughput techniques such as laser ablation. We proposed to use a unique chemical vapor deposition (CVD) precursor system that would allow, for the first time, the deposition of the MgB_2 phase using this technique. Resources were sufficient to prepare the CVD for the deposition of MgB_2 using two unique precursors, and for a limited number (5) of runs. The films were characterized with regard to their crystallinity and composition. It was determined that MgB_2 was not formed under the conditions utilized, although elemental magnesium was deposited. This was encouraging for future attempts, as well as valuable in itself.

Introduction

The recent discovery of superconductivity in magnesium diboride, MgB_2, by Akimitsu et al. caused a flurry of activity among researchers all over the world.[1,2] MgB_2 is a simple binary intermetallic compound with a transition temperature, T_c, of 39 K. This value is nearly twice that of any previously known metallic superconductor. Bud'ko et al.[3] demonstrated a boron isotope effect in $Mg^{10}B_2$ with an increase of T_c to 40.2 K and concluded that the compound behaves as a phonon-mediated BCS superconductor. The growth of thin films of MgB_2 with T_c near 39 K and with critical current densities greater than 10^5 A/cm^2 has been reported.

The problem in growing high-quality MgB_2 films in situ using physical vapor deposition techniques is that the very high vapor pressure and volatility of magnesium in the temperature range suitable for formation of MgB_2 (850–900°C) results in magnesium-deficient films. Hence, investigations have focused on using an ex situ approach so far. Such investigations use a two-step approach wherein a boron precursor film is first deposited on the substrate and then the sample is annealed in a magnesium-containing environment. Zeng et al.[4] have very recently reported a high-pressure chemical vapor deposition (CVD) in which they bulk heat magnesium to provide the vapor source and react it with diborane. Besides the tremendous toxicity of diborane, the use of high pressures is problematic in that deposition on desired surfaces is difficult to control. Here, we propose to use a new method to fabricate high-quality MgB_2 films—metalorganic CVD (MOCVD), which may be useful for both epitaxial and nonepitaxial potential applications. Very recent reports from the Pennsylvania State University confirm that a quasi-CVD approach can produce high-quality MgB_2 films, although the boron source and volatility of the magnesium are still problematic.[3]

Technical Approach

This project used the organometallics bis-(cyclopentadienyl)-magnesium (Cp_2Mg) as the magnesium source and *o*-carborane, *o*-$C_2H_2B_{10}H_{10}$, as the boron source and were commercially available from Aldrich, Inc. The required CVD equipment was available in our laboratory.

The efforts focused on the conditions needed to produce dense, uniform coatings of ~0.2–1 μm in thickness on various single-crystal substrates of interest such as C-plane sapphire. Variables that were explored centered on the evaporation temperatures of the organometallic sources. Because of the differing thermochemical stability of the organometallics employed, different evaporation temperatures at the same pressure are possible. Argon carrier gas was used to deliver precursor molecules into the reaction zone. As Cp_2Mg is an air-sensitive compound, it required specialized handling, including the use of glove bags.

A set of evaporation temperatures for Cp_2Mg and *o*-carborane temperatures were explored to deposit MgB_2 films. The films were characterized with respect to crystallinity, composition, and microstructure using electron microscopy/scanning Auger spectroscopy and X-ray diffraction.

Results and Accomplishments

A CVD system was modified to accept the organometallic precursor source vessels. The precursors were acquired and were installed in the deposition system. The entire system was tested for leak-tightness and thermal stability. Since the vapor pressures of the precursors were unknown, the range of vapor source temperatures had to be estimated. These resulted in an apparent high rate of evaporation of the *o*-carborane and a more modest evaporation rate of the magnesium precursor.

Five runs at various temperatures and flows were performed and are summarized in Table 1.

Table 1. Summary of CVD run conditions

Run No.	*o*-carborane					Bis-Mg					Furnace temp. (°C)	Run time (min)
	Temp (°C)	H_2 flow (sccm)	Weight (g)			Temp (°C)	H_2 flow (sccm)	Weight (g)				
			Initial	Final	Change			Initial	Final	Change		
1	105	100	1178.7	1176	2.7	140	100	1198.8	1195.6	3.2	700	15[a]
2	50	250	1176	1176.1	–0.1	100	250	1195.6	1189.3	6.3	700	120
3	100	250	1181.3	1180.1	1.2	50	250	1189.3	1188.8	0.5	700	37[a]
4	75	250	1180.6	1178.6	2	50	250	1188.8	1187.8	1	700	120
5	75	250	n/a	n/a	n/a	75	250	n/a	n/a	n/a	700	120

[a]Clogging in *o*-carborane lines stopped run. *o*-carborane pot was refilled after second run.

The weight gains for the coatings on sapphire substrates are listed in Table 2. Coatings were optically observed on the substrates (Fig. 1), although the weight gain on the ~6-mm-square samples was low. Low-angle and normal-incidence-angle X-ray diffraction did not indicate the presence of a detectable coating. However, scanning Auger analysis did reveal an elemental magnesium coating on specimens of run 2 (Fig. 2), as well as oxygen and carbon. The oxygen is likely a contaminant from the air, as magnesium will form a native oxide. The carbon can be either an environmental contaminant or actually deposited from the carbon in the precursor. There was no observation of boron in the coatings or of MgB_2. It was observed that the cooled exhaust end of the reactor condensed crystalline material during the run that had the same appearance as the *o*-carborane. It was thus assumed that the *o*-carborane was transported through the CVD furnace unreacted.

Table 2. Results of CVD runs

Run	Specimen	Initial (g)	Final (g)	Gain (g)
1	1	0.3179	0.3183	0.0004
	2	0.3198	0.3203	0.0005
	3	0.3170	0.3175	0.0005
2	1	0.3190	0.3397	0.0207
	2	0.3196	0.3274	0.0078
	3	0.3182	0.3244	0.0062
3	1	0.1470	0.1483	0.0013
	2	0.3176	0.3202	0.0026
	3	0.3170	0.3196	0.0026
4	1	0.1473	0. 1474	0.0001
	2	0.1473	0. 1475	0.0002
	3	0.1469	0. 1471	0.0002
5	1	0.1470	0. 1476	0.0006
	2	0.1469	0. 1468	–0.0001
	3	0.1467	0. 1474	0.0007

Summary and Conclusions

Given the uncertainties entering into the project and the limited resources, it was not possible to accomplish the deposition of MgB_2. Encouraging results were seen in the deposition of elemental magnesium, which in itself is difficult to accomplish. The bis-(cyclopentadienyl)-magnesium does indeed reduce to magnesium under appropriate CVD reactor conditions. These were high hydrogen-to-magnesium precursor gas ratios, approximately 700°C ambient, and reduced total pressure.

The stability of *o*-carborane was too great to allow deposition of the diboride. The precursor appeared to transport through the reactor unaffected. Subsequent considerations resulted in the conclusion that less-stable boron sources, such as diborane, would have had a substantially greater probability of success. Unfortunately diborane was not considered in the project due to its both high toxicity and pyrophoric/explosive nature. Although the use of diborane is possible, it would have required a very significant upgrade in the safety configuration of the CVD apparatus.

A major benefit of this research has been the demonstrated ability to deposit elemental magnesium. This led directly to the development of a preliminary proposal

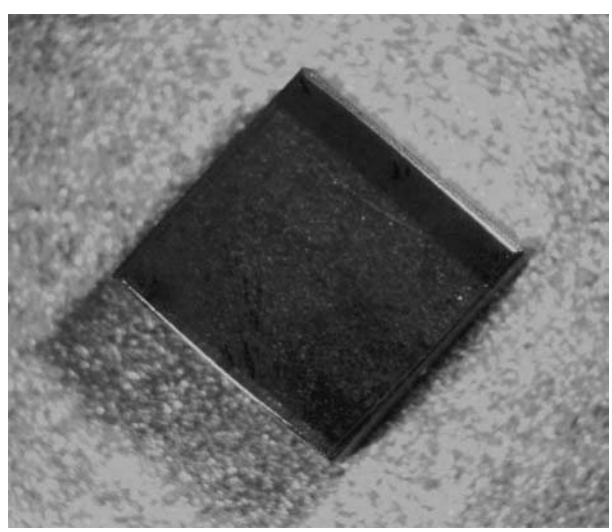

Fig. 1. Optical image of a 6-mm-square coated sapphire substrate.

to participate in a DOE virtual center for research on the storage of hydrogen. Although this proposal was not successful, efforts are continuing to develop magnesium-based hydrogen storage projects based on these results.

References

[1]J. Akimitsu, Symposium on transition metal oxides, Sendai, January 10, 2001.

[2]J. Nagamatsu, N. Nakagawa, T. Muranaka, Y. Zenitani, and J.Akimitsu, *Nature* **410**, 63 (2001).

[3]A. V. Pogrebnyakov, J. M. Redwing, J. E. Jones, X. X. Xi, S. Y. Xu, Q. Li, V. Vaithyanathan, and D. G. Schlom, *Appl. Phys.Lett.* **82**(24), 4319 (2003).

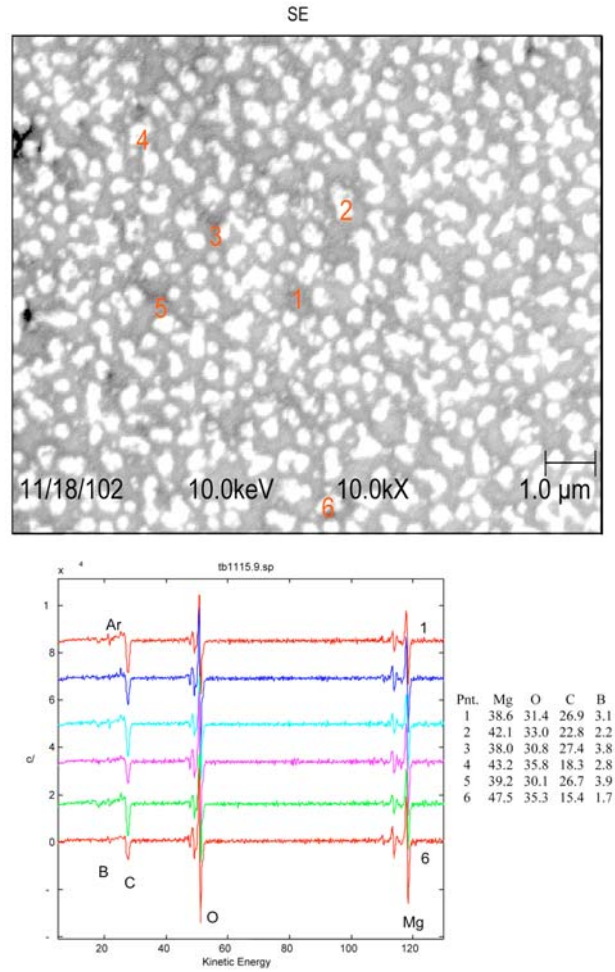

Fig. 2. Scanning Auger results for specimen 3 of run 2 (Tables 1 and 2). The upper image is a secondary electron image indicating positions where the Auger signals were acquired. The Auger energy spectra are shown in the lower image with indicators for the elemental identification. The table is an integrated numerical determination of the relative percentage of the elements observed.

Light-Emitting Nanoscale Tunnel Junctions

T. L. Ferrell
Life Sciences Division

This project was initiated to fabricate and study light-emitting, metal-oxide-metal, electron tunneling junctions on the nanoscale. It is well known that macroscopic metal-oxide-metal (MOM) tunnel junctions radiate with low efficiency. On the nanoscale, the junctions, in which the tunneling electrons engender localized radiative surface plasmons, can radiate with an efficiency 137 (reciprocal of the fine-structure constant) times greater than that of previously investigated millimeter-scale junctions. With each junction of a size much less than the wavelength of the photons emitted, an array of the junctions would radiate in dipolar mode with sufficient intensity to provide an extremely high-resolution, three-dimensional, thin, flat-screen, color display. The frequency of emission would be eV/h for a bias voltage V so that tunable operation in the visible would require 1.5–3 volts. Additionally, operation in reverse would provide a new type of photovoltaic device with stacked transparent layers illuminated laterally by p-polarized light. Finally, due to the sensitivity of the surface plasmon resonance to the optical index of an adsorbate, a novel sensor array could be realized that presents high spatial resolution. Previous studies on the millimeter scale produced low emission intensities due to the multiple couplings needed for radiative emission, but this work established methods of obtaining practicable operation lifetimes.

Introduction

Metal-oxide-metal (MOM) tunnel junctions have been explored for many years motivated by interest in the associated fundamental physics and by the possibility of obtaining thin-film, tunable, light emitters in the visible portion of the electromagnetic spectrum. A considerable body of literature was amassed due to a variety of potential applications. Unfortunately, in practice, the millimeter-scale junctions have poor emission intensities and tend to suffer breakdown due to oxide surface irregularities, impurities, or diffusion of metal ions. MOM tunnel junctions have in the past invariably been constructed using flat wire electrodes of millimeter size. The poor emission intensities are due to the fact that the tunneling first engenders nonradiative surface plasmons that must thereafter couple to dipolar surface plasmons on surface roughness features on the upper electrode. In this project, a high-density nanoscale alternative was explored with far superior characteristics and performance with the ideas of enabling high-resolution, three-dimensional displays, sensors, and photovoltaic cells, and potentially a new type of tunable laser.

Technical Approach

Fundamental theory predicts that by eliminating the need for an intermediate coupling stage involving the nonradiative mode, a much higher emission intensity would be evinced. As a result, the objective was to produce an array of nanoscale tunnel junctions using microlithographic masks prepared by electron-beam lithography and applied using the standard lift-off process for metal deposition. Such an array consists of aluminum wires of 120-nm width separated by a slightly larger amount, oxidized, and orthogonally crossed with similarly sized and arranged gold wires. Elementary electrodynamics provides that a radiative dipole is induced on any surface that is bounded in one or more dimensions on the nanoscale (dimensions smaller than the wavelength of the emission) when the electron distribution is locally disturbed from equilibrium. In the present geometry, each junction is bounded normal to the surface and diagonally at the inside "corners." Hence, direct dipole radiation is emitted normal to the surface and tangential to the surface by the respective surface plasmon modes engendered by the tunneling electrons. This eliminates the intermediate-stage coupling to the nonradiative surface plasmons and thus is of much higher intensity since losses occur at each necessary stage of coupling.

Fabrication by electron-beam lithography was used in this project in order to obtain the nanometer-scale linewidths required. The fabrication was carried out via a subcontract with Dr. Greg Norden of the University of Alabama in Huntsville (UAH). The procedure used was to first layout the design (Fig. 1) and then carry out the following lithography process:

1. Sputter 500-nm SiO_2 on silicon wafer for insulation purposes.

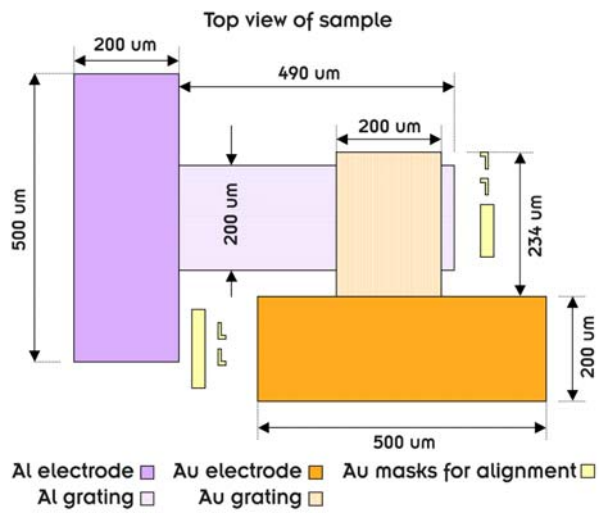

Fig. 1. Layout drawing for tunnel-junction array.

2. Spin coat 150 nm PMMA A4 on the surface and bake the resist at 400°C.
3. Fabricate two sets of "L"-shaped Au masks by e-beam exposure followed by Au metallization and lift-off.
4. Repeat spin and bake of PMMA on the sample.
5. Expose the Al pad and grating pattern by using one of the two alignment mask sets followed by Al metallization and lift-off.
6. Grow Al_2O_3 on the top of the Al grating (200° and 15 min in oven).
7. Repeat spin and bake of PMMA on the sample.
8. Transfer the Au electrode pattern by using the same alignment mask set as used in step 5 followed by a Cr-Au metallization and lift-off.
9. Repeat spin and bake of PMMA onto the sample.
10. Transfer the Au grating pattern by using the second alignment mask set followed by purely Au metallization and liftoff.

A complete theory of the light emission wavelength, intensity, angular distribution, and polarization in the present case was developed at ORNL. The parameters of the device were thus known to UAH for purposes of fabrication. Testing at ORNL was conducted for similar mesoscopic samples in order to prepare the substantial portion of the test procedures for the nanoscale devices.

Results and Accomplishments

The first devices using the above procedure were successfully fabricated in the first six months of the project. The contacts to the device were then attempted using a commercial wirebond instrument. In this step the Au-Al_2O_3 contacts peeled and the device was not then viable. In the ensuing attempts at fabrication, the scanning electron microscope began displaying anomalies that grew worse over time. Further samples thus displayed irregularities that prevented their use in testing. Service on the scanning-electron microscope was requested from the vendor but was unavailable for the remaining three months of the project due to corporate-level changes by the manufacturer. Device images are shown in Figs. 2 and 3.

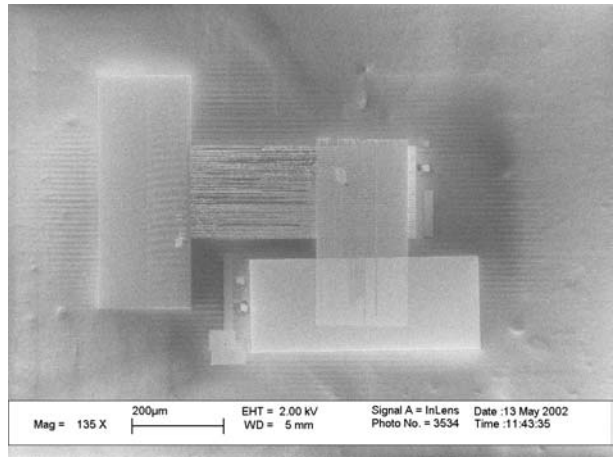

Fig. 2. First tunnel-junction array fabricated.

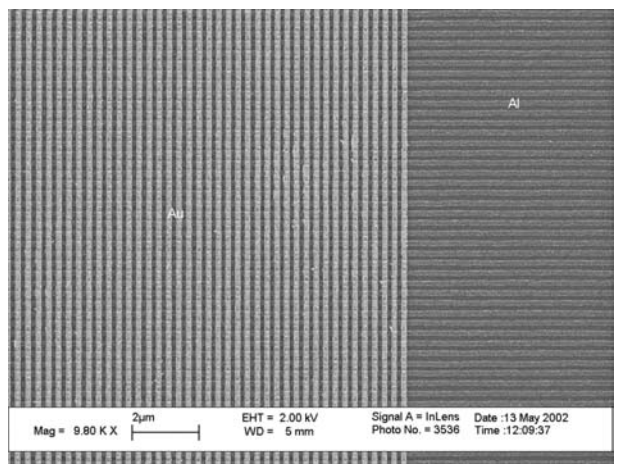

Fig. 3. Scanning electron microscope image of first array.

Images of all samples prepared are shown in the figures. It was thus established that the desired tunneling junction array can be fabricated by electron-beam lithography, but samples could not be further studied.

Summary and Conclusions

Although the technical difficulties prevented our obtaining samples that could be tested for light emission, the fact that samples were fabricated led us to apply for capital funding for an ORNL electron-beam lithography system that would allow further work. We were able to obtain $125,000 in capital funds from the DOE for this purpose and are currently preparing proposals using the preliminary sample images and results.

Dynamic Transport in Nanostructures

Z. Zhang,[1] A. Eguiluz,[1,2] S. T. Pantelides,[1,3] and K. Varga[1]
[1]*Condensed Matter Science Division*
[2]*University of Tennessee, Knoxville*
[3]*Vanderbilt University , Nashville*

Conventional microelectronics is already confronting the nanoscale, where quantum phenomena are inevitable. The time is approaching fast when nanoscale devices will have to exploit quantum phenomena instead of avoiding them. The theoretical understanding of the transport in nanoscale devices is very important. We have developed new approaches to transport problems which are simpler and more efficient than previous methods. Our research focused on two important areas: the development of a novel "source and sink" approach to transport and the development and implementation of the time-dependent density functional theory (TDDFT) for large-scale simulations of the dynamical aspects of quantum transport. We have implemented a Lagrange interpolants approach into the TDDFT, which combines the rapid convergence of spectral methods with the matrix sparsity of the local (real space) representations. This new technique speeds up the calculations by an order of magnitude, facilitating direct-time-step integration in TDDFT.

Introduction

It is now clear that silion-based technologies are expected to reach insurmountable roadblocks beyond the year 2020. One of the most promising directions for overcoming the envisioned obstacles lie in the development of a robust nanoscale electronic systems, which promises to open a whole new world of novel devices and sensors with outstanding capabilities. Indeed, the past decade has seen considerable progress in producing experimental prototypes of such devices. Theoretical progress in this field is considerably slower, and it has so far been limited primarily to DC transport. There is, however, a substantial interest in time-dependent transport in nanostructures; dynamic conductance, photon-assisted tunneling, AC characteristics, nanostructures in time-varying electromagnetic fields, electron pump, electron turnstiles, and frequency-dependent localization, are just a few examples where time-dependent electron dynamics plays an extremely important role. In the last few decades, the emphasis of first-principles quantum mechanical calculations for molecules and solids has been the electronic structure of the ground state and the exploration of the available unoccupied states (excited states). It is important to note that the transport problem is far more complicated than the usual ground-state problem or the problem of excited states of molecules or crystalline solids, which represent closed systems (the Schrödinger equation amounts to solving an eigenvalue problem). The transport problem has distinctly different boundary conditions, namely links to reservoirs of electrons with a steady-state current. We have developed two new and novel approaches to solving the time-dependent or dynamic quantum transport problem. In the first approach we evaluate an approach to quantum transport by directly building in "sources and sinks" for the current into the ab initio problem. In the second approach, we combine the Schrödinger and Maxwell equations and explicitly integrate them in time.

Technical Approach

In the approach we have developed, the circuit (i.e., the open system consisting of the device, the leads and the battery) is replaced by a closed finite system that with a source and a sink which are connected to the device as shown in Fig. 1. The source and the sink are modeled by imaginary Dirac delta-function potentials. A positive imaginary potential injects electrons, while the negative imaginary potentials absorb the wave function at the boundaries. The novelty of this method is that the source and sink potentials may be determined self-consistently, and that they therefore drive the same current through the molecular device with the same voltage drops.

To see this, we consider the continuity equation for the current density j of a device subject to a Hamiltonian that contains an imaginary potential $W(r)$:

$$\nabla j = 2W(r)\rho(r) .$$

Depending on its sign, W describes a source or sink for the current flowing through the system. When a Dirac delta-like source is added to the right, along with a

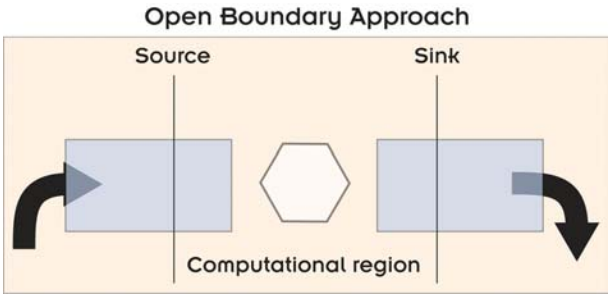

Fig. 1. Schematic of a two-probe structure with "source/sink" boundaries.

corresponding "sink" term (same potential with the opposite sign) to the right, the corresponding imaginary potential takes on the form:

$$iW(r) = \frac{I}{2\rho(r)}[\delta(z-L) - \delta(z-R)] \quad .$$

To impose these injecting and absorbing boundary conditions, the Schrodinger equation with wavefunction

$\phi(r) = \exp\,[iG(r)]\ \varphi(r)$

with real functions $G(r)$ and φ(r) may be decomposed into its real and imaginary parts:

$$H + \frac{1}{2m}[\nabla G(r)^2]\varphi(r) = E\varphi(r)$$

and

$\nabla^2 G(r)\ \varphi(r) + 2\nabla\ G(r)\ \nabla\ \varphi(r) = 2W(r)\ \rho(r)$.

The first equation is a Schrödinger equation with an extra potential term for the real wave function $\varphi(r)$, while the second equation is continuity equation of the probability current $j(r) = \nabla\ G(r)\ \rho(r)$,

$\nabla j(r) = 2W(r)\ \rho(r)$.

The Schrödinger equation and the continuity equation for ∇G need to be solved self-consistently.

Results and Accomplishments

Our initial numerical calculations for simple systems, for example, for an analytically solvable square-well potential barrier (see Fig. 2) or for a three-atom sodium nanowire connected to jellium electrodes (see Fig. 3), show that this approach can work very efficiently and accurately.

We believe that this approach has the following potentially unique features:

- The transport problem for open systems is transformed into an eigenvalue problem. The eigenvalue problem is very similar to the usual Kohn-Sham equations, and therefore the existing advanced techniques developed for the solution of the Kohn-Sham equation can be utilized.
- The current is calculated explicitly using current-carrying complex wave functions. The method therefore can be used in current density functional theory approaches as well.
- Multiterminal devices can be described by introducing several sources and sinks. This makes possible the direct investigation of FET transistors and other devices where the current is controlled by a gate voltage.
- A further advantage may be that this approach may be extended to time-dependent transport problems. In this case, the boundary conditions depend on time and time-dependent "source and sink" terms are needed.

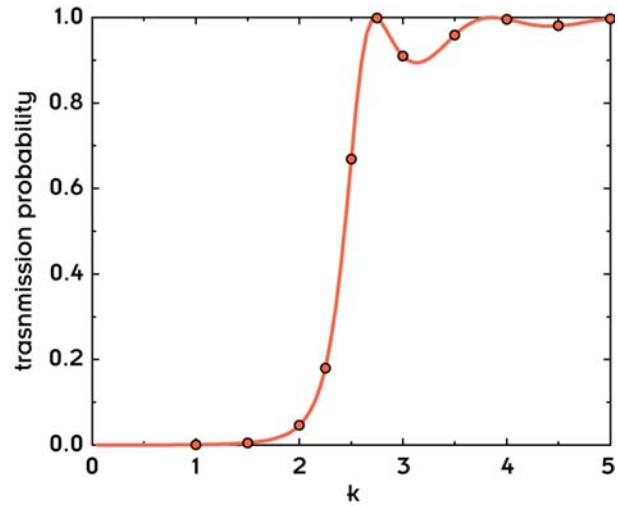

Fig. 2. Comparison of the exact and numerically calculated transmission probability for a square-well potential barrier.

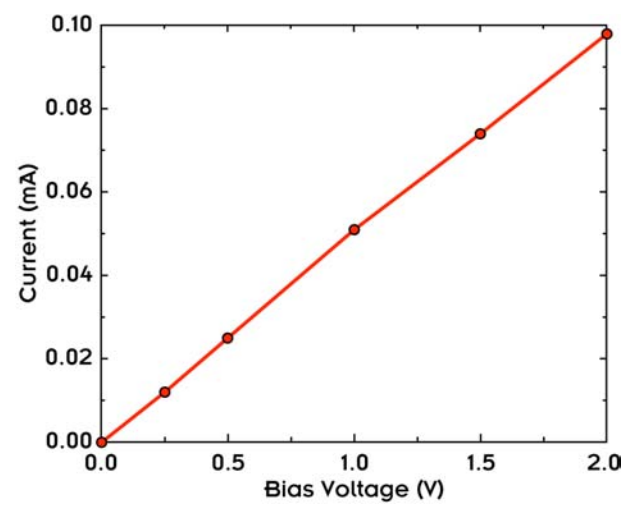

Fig. 3. I-V characteristic of a three-atom sodium nanowire connected to tellium electrodes.

Our aim was to develop tools for large-scale time dependent density functional theory (TDDFT), which directly couple the Schrödinger and Maxwell equations. This approach, while computationally demanding, is important because it provides a natural scheme for a first-principles treatment of the electronic conduction in such "difficult" cases as nonequilibrium and strongly inhomogeneous systems. Indeed, TDDFT enables one to meaningfully discuss the dynamical effects of quantum confinement in the presence of important correlations between the electrons, which are treated on the same footing as the electronic structure and bonding characteristics of the molecular device. To this aim we have developed a new very powerful approach for the direct time integration of the TDDFT equations. In this method the real space part of the wave function is represented by a Lagrange mesh basis, which dramatically reduces the basis dimensions to facilitate the fast direct solution of the time-dependent problem. The Lagrange basis functions are defined by the property that they are equal to unity in a single grid point but vanish on all other grid points.[1,2] It is a variational, spectral method with exponential convergence; the basis functions are very flexible and Hamiltonian is sparse. This basis preserves the most advantagous property of the real space mesh methods, but the basis functions are defined everywhere, not only on the mesh points. Due to the Lagrange interpolation condition, the potential matrix elements are diagonal and the matrix elements of the kinetic energy operator can be easily calculated by numerical integration.

The implementation of the Lagrange mesh technique dramatically speeds up the convergence and reduces the size of required basis dimensions. We have compared the convergence of the energy of the C_6H_6 molecule using the Lagrange mesh and a traditional finite-difference scheme in Table 1. This shows that the number of basis functions is about an order of magnitude smaller then in the previously applied methods. This results in a significant speed up in time-dependent simulations, and it also gives us a better control of accuracy.

Table 1. Convergence of the energy (in eV) of C_6H_6 as a function of number of basis states N using Lagrange mesh (LM) and finite difference (FD) approaches

N	LM	FD
8^3	–1014.40	
12^3	–1016.85	
16^3	–1016.72	–1014.67
20^3	–1016.73	–1015.82
24^3	–1016.73	–1016.51
28^3	–1016.73	–1016.72
32^3	–1016.73	–1016.73

Summary and Conclusions

We have developed a very efficient new approach to transport problems[3] in which using a sink and a source potential maps the open boundary problem to a closed eigenvalue problem. Its accuracy and efficiency have been illustrated through several benchmark calculations. To facilitate fast and reliable direct-time integration of TDDFT equations, we have developed a new Lagrange mesh–based approach[4] which speeds up the convergence and reduces the basis dimensions considerably. These new techniques allow us faster and more efficient calculations of molecular electronic devices.

Follow-on funding has been received from DOE for "Integrated Multiscale Modeling of Molecular Computing Devices."

References

[1]D. Baye and P.-H. Heenen, *J. Phys.* **A19**, 2041 (1986).

[2]B. I. Schneider and N. Nygaard, *J. Chem. Phys.* **A106**, 10773 (2002).

[3]K. Varga, Z. Zhang, and S. T. Pantelides, "Open Boundary Approach to Transport Problems," in preparation.

[4]K. Varga, Z. Zhang, and S. T. Pantelides, "Lagrange Mesh Approach to the Solution of the Density Functional Equations," in preparation.

Nanocrystalline Giant Magnetostrictive Materials for Microactuator Applications

C. T. Liu,[1] J. A. Horton,[1] C. L. Fu,[1] E. P. George,[1] and J. H. Zhu[2]
[1]*Metals and Ceramics Division*
[2]*Tennessee Technological University*

This project focused on the development of nanocrystalline giant magnetostrictive (GMS) materials for next-generation microactuators which will exhibit large-displacement, high-actuating force/energy density, low-actuating and saturation magnetic fields, rapid response, and compatibility with Si microfabrication. The project demonstrated that the amorphous state in the $(Tb,Dy)Fe_2$–based system could be stabilized by combining alloy design and melt spinning. Initial work showed that by controlling the annealing condition (i.e., temperature), the crystallization process could be controlled and nanocrystalline GMS materials could be synthesized. It was further indicated that the nanocrystalline GMS materials exhibited higher magnetostriction and/or magnetostrictive strain coefficient, in comparison to both amorphous and fully crystalline GMS materials.

Introduction

In the past several years, microelectromechanical systems (MEMS) have evolved rapidly from an academic curiosity into a relatively new technology of considerable commercial and military interest. A crucial element of MEMS technology is the development of suitable microactuators. Thin-film/thick-film magnetostrictive materials have been recognized recently as a promising material for making MEMS microsensors and microactuators,[1–5] due to the low actuating voltage, high actuating force, and fast response. Microactuator devices utilizing magnetostriction as the actuation mechanism have been designed and demonstrated, including micropumps,[3–6] linear ultrasonic motor,[3] small flying machine,[7] etc.

Terfenol-D, based on a ternary Laves phase system with composition of stoichiometric $(Tb_xDy_{1-x})Fe_2$, is the preferred magnetostrictive material, with strains about 0.2% in a field of 10,000 Oe at room temperature.[8] One important issue related to MEMS application of magnetostrictive materials is to increase the magnetostriction at low magnetic field and to lower the saturation field. Recent studies indicated that stabilization of the amorphous state in $(Tb,Dy)Fe_2$ via alloying additions (such as boron) and rapid cooling could significantly reduce the saturation field.[9–11]

Even though amorphization has been found to reduce the saturation field of $(Tb,Dy)Fe_2$ significantly, it has an adverse effect in decreasing the maximum magnetostrictive strain. What is really desirable for microsystem application is to increase the magnetostrictive strain coefficient and maximum magnetostrictive strain while maintaining the low saturation field through some innovative approach. In this project, nanocrystalline magnetostrictive materials based on $(Tb,Dy)Fe_2$ are proposed to achieve the desired performance for MEMS applications.

Technical Approach

To achieve the desirable performance for the microactuators, it is proposed to form aligned nanocrystalline $(Tb,Dy)Fe_2$ with a size of 1–10 nm in an amorphous matrix by crystallizing amorphous $(Tb,Dy)Fe_2$ alloys in controlled magnetic fields. The rationale for such an approach is as follows: the amorphous matrix and the nanoscale crystalline phase will reduce the magnetoelastic anisotropy of the material, thus retaining the low saturation magnetic field of the amorphous alloy; under the influence of magnetic field during crystallization and cooling, the nanocrystalline phase will align themselves in such a way that the magnetostrictive strain will be maximized, up to or even surpassing the limit of the single-crystal material (0.2%); the reduction of grain size to nanoscale range will improve magnetic softness of the alloys; for example, coercivity and hysteresis will decrease dramatically.

Since the magnetostrictive properties correlate with the crystal size, it is important to develop scientific bases to control the grain size of these materials. One very attractive way to control the grain size of the crystalline materials is to first stabilize the amorphous state of the material, followed by controlled crystallization to get the desirable nanoscale grain size via thermal treatments. This approach requires a fast cooling rate or enhanced glass formability to obtain a supercooled liquid state.

Recent studies indicate that three metallurgical factors strongly affect the glass forming ability of bulk amorphous alloys:[12–14]

1. multicomponent systems consisting of more than three elements;

2. significant difference in atomic size ratios above 12% among the three main constituent elements; and
3. negative heats of mixing among the three main constituent elements.

According to the physical metallurgy principles required for forming amorphous structures, additional elements with tiny atomic size such as B and C, small atom size such as Co and Ni, and large atom size such as Zr and Al have been added to $(Tb,Dy)Fe_2$ system to achieve the large difference in atomic sizes among the main constituent elements. With careful control of alloying elements, it is expected that the glass-forming ability of the $(Tb,Dy)Fe_2$ phase will be enhanced, and amorphous $(Tb,Dy)Fe_2$-based ribbons can be synthesized by melt-spinning.

Once the formation of amorphous structure has been accomplished, controlled heat treatments will be conducted to crystallize the materials to obtain nanocrystalline structures. By controlling the annealing temperature/time, it is possible to get extremely fine, nanoscale structures with the crystalline phase distributed in an amorphous matrix, or a mixture of several crystalline phases. Ultimately, magnetic field will be utilized during heat treatment to self-align the magnetic domains and thus further improve the magnetic and magnetostrictive properties of the nanocrystalline GMS materials.

Results and Accomplishments

We first characterized the magnetostrictive properties of commercial GMS Terfenol-D bar processed by directional solidification (DS) (supplied by ETREMA Products, Inc.) and melt-spun ribbon fabricated in our laboratory using the ETREMA material. It was found that the Terfenol-D ribbons synthesized by melt-spinning were crystalline, and the amorphous state could not be stabilized by modifying the melt-spinning parameters alone. Furthermore, the magnetostriction of the Terfenol-D ribbon was lower than the Terfenol-D bar and annealing of the ribbon at 500°C for 1 h did not improve the magnetostriction of the ribbon. This can be explained by the fact that the Terfenol-D bar was directionally solidified, and its grains have been preferentially oriented to optimize its magnetostrictive properties.

To develop amorphous $(Tb,Dy)Fe_2$-based alloys with enhanced glass formability, a large number of alloys with various alloying additions were arc melted using high-purity starting materials; furthermore, ribbons were prepared by melt-spinning, followed by characterization with X-ray diffraction and other techniques to assess if the amorphous state was stabilized in the ribbon. A magnetostriction measurement rig was constructed which could be used to measure the magnetostriction of the ribbons by the strain-gauge method, as shown in Fig. 1.

A series of alloy compositions have been identified, which retained amorphous structure after melt-spinning, as indicated by X-ray diffraction (Fig. 2). The alloy compositions are based on the multicomponent system of $Tb_{30}Fe_{(70-a-b-c)}X_aY_bZ_c$, where X and Y are small atoms compared to Tb or Fe, and Z is a reactive element added to scavenge oxygen and nitrogen in the alloys. The optimal contents of X, Y, and Z have been determined. Transition-metals such as Co and Ni were also added, which did not noticeably affect the glass-forming ability of the alloys. Preliminary results on heat treatment of the amorphous ribbons indicated that after crystallization at 500°C for 1 h a crystalline Laves phase is formed from the amorphous matrix (see Fig. 2 for X-ray diffraction results and Fig. 3(b) for a scanning electron micrograph). The precipitates were very fine, and the sizes were in the range of 5–50 nm. As a comparison, the as-spun ribbon shows a featureless, complete amorphous structure, see Fig. 3(a). On the other hand, heat treatment at 600°C for 1 h fully crystallized the material and more than two crystalline phases could be identified (see Fig. 2 for X-ray diffraction results). Obviously, TEM observation will be needed for further revealing the fine structure in these materials.

Preliminary magnetostriction measurements of the ribbons after different heat treatments are summarized in

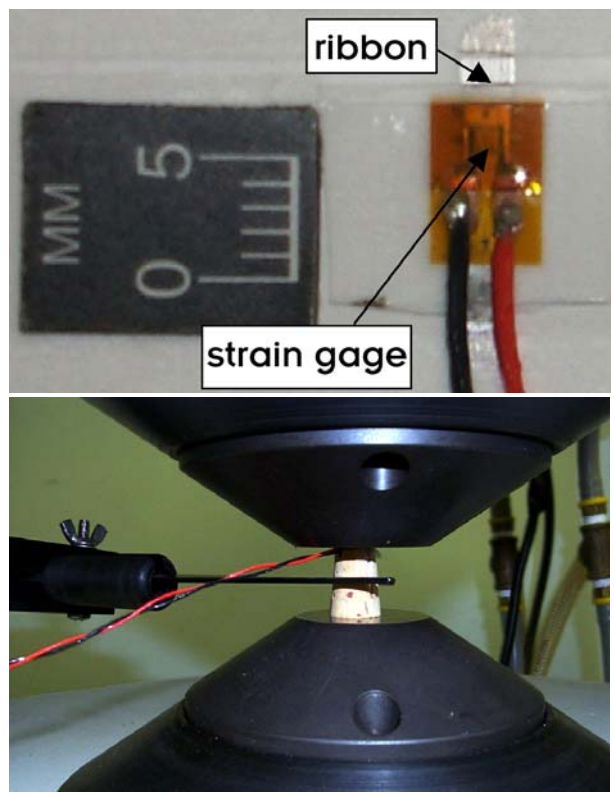

Fig.1. Test setup for measuring the magnetostriction of the ribbon:(a) ribbon with strain gauge on it; and (b) setup of the measurement rig.

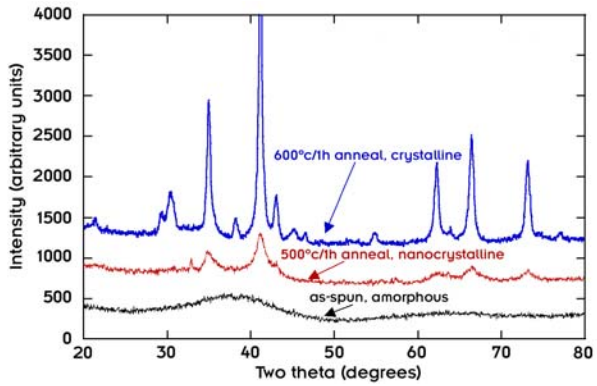

Fig. 2. X-ray diffraction results on melt-spun ribbons based on $Tb_{30}Fe_{(70-a-b-c)}X_aY_bZ_c$, indicating amorphous state for as-spun ribbon (black line), nanocrystalline state after 500°C/1 h anneal (red line), and fully crystallized state after 600°C/1 h anneal (blue line).

Fig. 4. Here, it was observed that the saturation magnetostriction was 280 µm/m for the amorphous ribbon, while heat treatment of 400°C for 1 h decreased the saturation magnetostriction slightly, yet increased the initial magnetostrictive strain coefficient. Heat treatment of 500°C for 1 h increased the saturation magnetostriction significantly, up to the level of 500 µm/m, possibly due to the formation of nanocrystalline microstructure. Further increase in annealing temperature decreased, instead of increased, the saturation magnetostriction.

Compared to the same alloy after arc-melting/casting, the nanostructured ribbon obtained by 500°C for 1-h heat treatment showed significantly higher magnetostrictive strain coefficient and required much lower actuating magnetic field to achieve saturation magnetostriction, as shown in Fig. 5. This clearly indicated that the amorphous/nanocrystalline structure was advantageous over the large-grained crystalline structure in the GMS materials. Figure 6 is a back-scattered electron micrograph showing the large, random crystalline structure in the as-cast $Tb_{30}Fe_{(70-a-b-c)}X_aY_bZ_c$ alloys. Corresponding electron probe microanalysis indicated that three phases were co-existing in the material, with the composition of each phase included in Table 1.

Summary and Conclusions

A series of alloy compositions with enhanced glass formability that retained the amorphous structure after melt-spinning have been identified. Initial heat treatment experiments have demonstrated that the crystallization process could be manipulated to achieve nanocrystalline microstructure in the developed alloys. The new alloy, after a 500°C for 1 h nanocrystallization treatment, possessed higher saturation magnetostriction and initial magnetostrictive strain coefficient and required smaller magnetic field for actuation, compared to the same alloys in the amorphous, as-cast, or fully crystallized conditions.

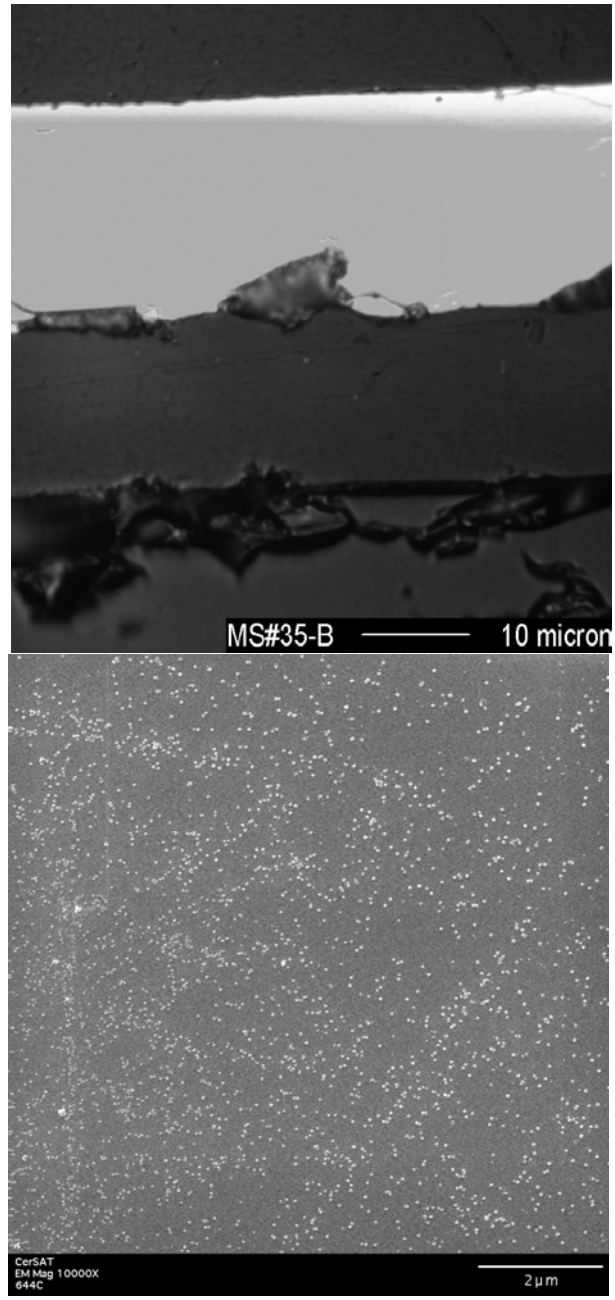

Fig. 3. Microstructure of amorphous and nanocrystalline ribbons ($Tb_{30}Fe_{(70-a-b-c)}X_aY_bZ_c$): (a) in as-spun condition, showing featureless amorphous structure; (b) upon annealing of 500°C for 1 h, showing fine precipitates of the Laves phase in an amorphous matrix.

References

[1]E. Quandt, H. Holleck, "Materials Development for Thin Film Actuators," *Microsystems Technologies* **1**, 178–184, (1995).

[2]G. Flik, M. Schnell, F. Schatz, and M. Hirscher, "Giant Magnetostrictive Thin Film Transducers for Microsystems," *Proc. Actuator* **94**, Bremen, 232 (1994).

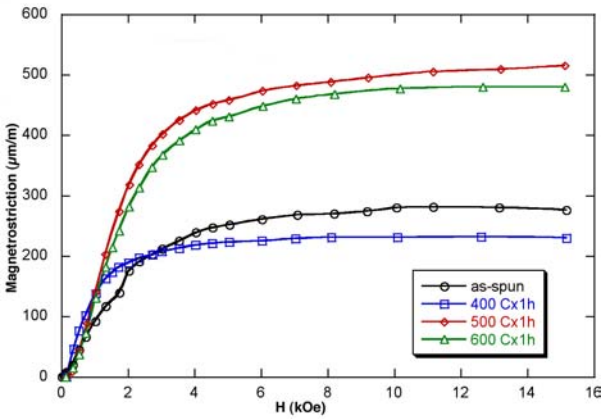

Fig. 4. Magnetostriction of the $Tb_{30}Fe_{(70-a-b-c)}X_aY_bZ_c$ ribbons after different heat treatments.

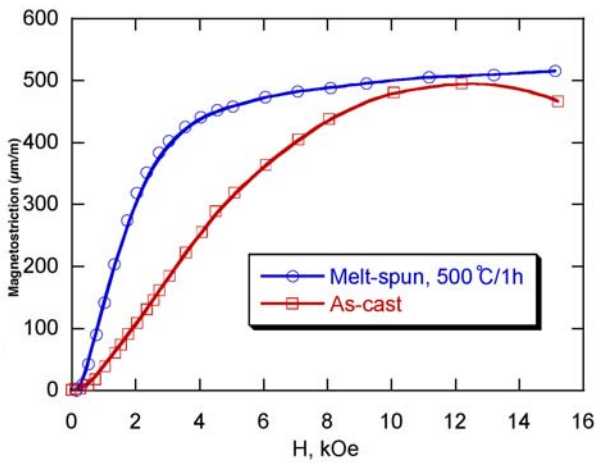

Fig. 5. Comparison of magnetostriction of nanostructured $Tb_{30}Fe_{(70-a-b-c)}X_aY_bZ_c$ ribbon (after 500°C for 1h annealing) and crystalline button (after arc-melting/casting). Note that both of these curves are for no crystallographic alignment while the maximum for DS Terfenol material is a strain of 2000 μm/m.

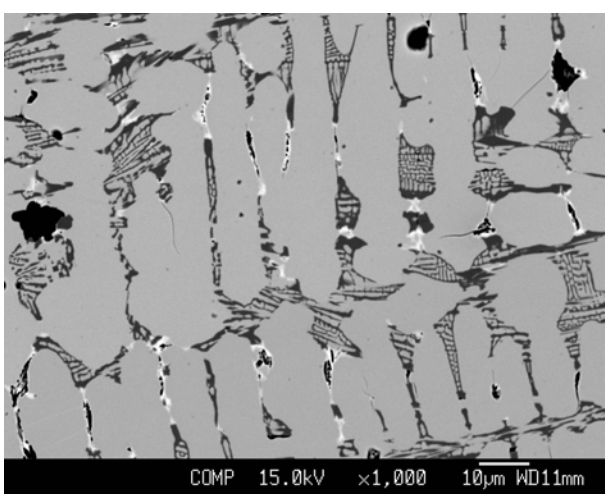

Fig. 6. Back-scatter electron image of bulk $Tb_{30}Fe_{(70-a-b-c)}X_aY_bZ_c$ alloy after casting.

Table 1. EPMA results of the compositions of the phases coexisting in the $Tb_{30}Fe_{(70-a-b-c)}X_aY_bZ_c$ alloy after casting

Phase	Fe	Tb	X
Matrix	59.1	31.4	9.3
Dark Phase	43.2	14.1	42.4
White Phase	27.2	36.1	36.3

[3]E. Quandt, "Giant Magnetostrictive Thin Film Materials and Applications," *J. Alloys & Compounds* **258**, 126–132 (1997).

[4]J. Betz, K. Mackay, J.-C. Peuzin, B. Halstrup, and N. Lhermet, "Torsion Based Drift-Free Magnetostrictive Microactuators," *Proc. Actuators 96,* Bremen, 283 (1996).

[5]E. Quandt and K. Seemann, "Fabrication and Simulation of Magnetostrictive Thin-Film Actuators," *Sensors and Actuator A* **50**, 105 (1995).

[6]E. Quandt and K. Seemann, "Magnetostrictive Thin-Film Microflow Devices," in: H. Reichl, A. Heuberger (Eds.), *Micro Systems Technologies* **96**, VDE-Verlag, Berlin, 451 (1996).

[7]K. I. Arai, W. Sugawara, K. Ishiyama, T. Honda, and M. Yamaguchi, "Fabrication of Small Flying Machines Using Magnetic Thin Films," *IEEE Trans. Magn.* **31**, 3758 (1995).

[8]A. E. Clark, "Magnetostrictive Rare Earth-Fe_2 Compounds," *Ferromagnetic Materials,* Vol. 1, ed. by E. P. Wohlfarth, North-Holland, (1980).

[9]W. J. Ren, Z. D. Zhang, A. S. Markosyan, X. G. Zhao, X. M. Jin, and X. P. Song, "The Beneficial Effect of the Boron Substitution on the Magnetostrictive Compounds $Tb_{0.7}Pr_{0.3}Fe_2$," *J. Phys. D: Applied Phys.* **34**, 3024–3027, (2001).

[10]N. H. Duc, K. Mackay, J. Betz, Z. Sárközi, and D. Givord, "Magnetic and Magnetostrictive Properties in Amorphous $(Tb_{0.27}Dy_{0.73})(Fe_{1-x}Co_x)_2$ Films," *J. Phys.: Condens. Matter* **12**, 7957–7968, (2000).

[11]H. Fujimori, J. Y. Kim, S. Suzuki, H. Morita, and N. Kataoka, "Huge Magnetostriction of Amorphous Bulk (Sm,Tb)Fe_2-B with Low Exciting Fields," *J. of Magnetism and Magnetic Materials* **124**, 115–118 (1993).

[12]A. Inoue, "Stabilization of Metallic Supercooled Liquid and Bulk Amorphous Alloys," *Acta Mater.* **48**, 279–306 (2000).

[13]A. Inoue, A. Takeuchi, and T. Zhang, *Metall. Mater. Trans.* **29A**, 1779 (1998).

[14]A. Inoue, *Bulk Amorphous Alloys,* Trans. Tech. Publications, Zurich (1998).

Probing Charge Transport in Oriented Conducting Polymer Nanostructures: Toward Integrated Molecular Optoelectronics

M. D. Barnes
Chemical Sciences Division

This project focused on measurement and modeling of charge transport and optically gated conductivity in oriented polymer nanorods. This idea was based on newly discovered techniques for producing oriented semiconducting polymer nanoparticles with structural and photophysical properties that are quite different from bulk material. The specific goals of this project were to probe charge transport behavior of isolated polymer nanoparticles and electronic coupling between polymer chains and molecular wire/logic structures as first steps toward enabling an optical interface to molecular-level electronic circuitry, and use of polymeric materials in the newly emerging field of nanoscale optoelectronics.

Introduction

Nanophotonics—or molecular-scale optoelectronics—is a rapidly emerging area of research that combines nanoscale optical elements (e.g., single-molecules, or quantum dots) and molecular-scale electronics. Such "photonic elements" could ultimately provide a route for connecting the macroscopic and nanoscopic worlds through absorption or emission of photons coupled with electron (or hole) motion to or from, say, a molecular wire or gate structure. Here the materials challenge in design and fabrication of such elements is daunting: For practical applications, one needs nanoscale components with well-defined transition energies and dipole moment orientation for spatially selective addressability, as well as robust photostability and facile charge transport properties. Because of the inherent size scalability, responsiveness to optical excitation, and long history in mesoscale photonics, semiconducting polymers make attractive candidates for nanoscale optoelectronics. However, in conventional thin film formats, these species are formed with random in-plane orientation with a broad distribution of chain morphologies and tend to be quite fragile with respect to repeated optical excitation.

The inherent size scalability and large parameter space associated with structural and electronic properties of semiconducting polymers[1] make them interesting candidates for the purpose of interfacing and interconnecting nanoscale logic units. The work of James Tour,[2] for example, has focused on synthetic techniques to fabricate molecular "wires" from conducting polymers with specifically designed branch architectures and end-group functionalities. However, in addition to difficulties in controlling the orientation and chain alignment of semiconducting polymers such as polyphenylene vinylene (PPV) derivatives, these species tend to be quite fragile with respect to repeated electronic excitation. Furthermore, most strategies for organizing conducting chain segments are based on molecular self-assembly which restricts the range of device geometries and position of the desired species. While gel-processing[3] or templating techniques[4] have been used to produce axially aligned conducting polymers, these strategies lack the molecular-level addressability and connectivity needed for multiplexed optoelectronic applications.

Our research program was designed to exploit recent experimental results in our laboratory that have demonstrated the ability to "print" single molecules of a conducting polymer with dramatically altered structural and photophysical properties relative to conventional thin-film preparations.[5,6] We observed luminescence characteristics strikingly similar to those recently observed for cadmium-selenide quantum rods[7] suggesting a highly ordered chain configuration with exciton delocalization within the particle. In addition to linear polarization in emission and modification of spectral characteristics, we found uniform particle orientation and a two-order-of magnitude enhancement in photostability relative to similar molecules deposited (from the same solution) by spin-casting. This modification of structural and photophysical properties derives in part from the effect of three-dimensional confinement by the liquid droplet of solution as it evaporates en route to the substrate.[8] As a result, this is a highly general method of preparing different kinds of nanostructured polymer systems for molecular scale optoelectronics with tailorable properties (absorption/emission frequencies, chain morphologies etc.). We find that many important luminescence characteristics are preserved—and in some cases enhanced further—by doping the polymer solution with other materials.

The many consistent experimental observations we have made on these species lead to a picture of a crystalline-like ordering of conjugated segments within an individual nanostructure (single chain). As such, many of the static electronic structure properties are modified – as manifested in the spectral narrowing and discrete emission frequencies seen in fluorescence. It was therefore natural to expect that the dynamic electronic properties, such as ballistic charge transport, would be greatly enhanced by virtue of the structural order as well. It was the primary goal of this project to make experimental measurements of "molecular wire" behavior in these oriented polymer nanostructures. In order to achieve this goal, it was necessary to develop experimental methodologies to orient these species on conducting substrates such as graphite, gold or indium-tin-oxide. In early experiments, it became clear that control over the (static) charge state of these materials, as well as the experimental parameters for making photochemically robust polymer nanostructures, was crucial to the ultimate program goals. We therefore concentrated our efforts here, and one of the most important results of this program was the development of a hybrid Kelvin-force scanning probe microscopy that allowed us to quantitate the magnitude and sign of static charge on individual polymer nanoparticles.

Technical Approach

Experiments were performed on a Dimension 3100 atomic force microscope (Digital Instruments) using silicon cantilevers coated with Cobalt and Chromium. A "Lift-Mode" scan was used in all these experiments, so that the topographic features could be decoupled from the image features generated by the long-range electrostatic forces. The surface potential was measured by nulling the electric field between the tip and the sample at each point in the image scan, by applying a bias to the tip. To quantify the charge on the sample, we used electric field gradient microscopy (EFM). In this technique the field gradient generated by the long-range electrostatic forces (between the charged sample and the biased tip) was kept at a constant level using a feedback loop which varied the drive frequency of the cantilever as it scanned the sample surface. The charge image was generated by plotting the frequency shift (measured using a lock-in amplifier) for each point in the scan. The shift in the drive frequency was used to calculate the force experienced by the cantilever. These forces arise from Coulomb interactions of the sample charge, its image charges in the AFM tip and substrate, and the induced charges due to the bias voltage applied to the cantilever. From an electrostatic analysis of the tip-sample system modeled using a parallel-plate geometry, the sample charge was quantified. An ultradilute (10^{-12} M) solution of cyano-polyphenylene vinylene (CN-PPV) in toluene was nebulized in a stream of dry nitrogen gas using a drawn glass capillary, and the samples were collected on a cleaned glass substrate and used for the EFM experiments.

Results and Accomplishments

We tested this technique by using a sample of polystyrene nanoparticles (20-nm diameter) which were deposited on a cleaned glass substrate using an electrospray device. By controlling the polarity of the voltage applied to the electrospray needle, we could control the charge on the polystyrene beads. We found excellent correlation between surface potential images and topographic scans, where each polystyrene bead spot shows a negative surface potential. The average surface potential per particle was 30 mV, corresponding to a charge state of about 15 individual carriers. For CN-PPV nanoparticles, topographic scans show heights ranging from 8–15 nm, values that are in good agreement with the persistence length of PPV molecules measured from light scattering experiments. Figure 1 shows the field gradient scan on a CN-PPV nanoparticle sample that provides quantitative information on the charge state. Frequency shifts in the range of 4–8 Hz were measured, corresponding to an excess surface charge of 2–5 electrons. EFM measurements on a freshly prepared CN-PPV sample showed frequency shift of 55 Hz, which corresponds to approximately 10 excess electrons on the CN-PPV nanoparticles. The change in the number of excess charges could be due to charge migration or dissipation phenomena, which is more pronounced in samples that

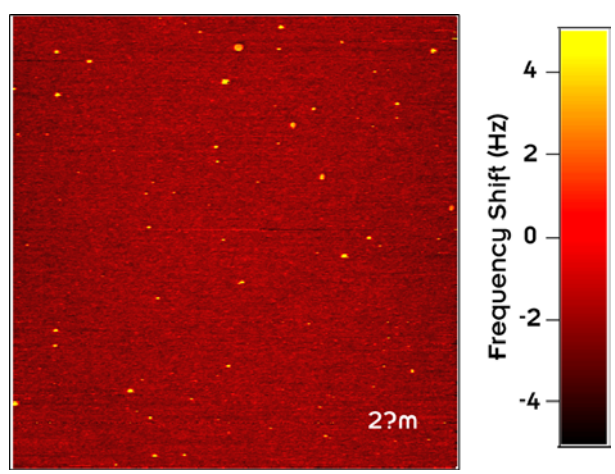

Fig. 1. EFM scan of CN-PPV nanoparticles showing the charge image. Frequency shift ranged from 4–8 Hz, which corresponds to an excess surface charge of 2–5 electrons. (A. Mehta, et al., to be published in Applied Physics Letters.*)*

are exposed to ambient conditions for long periods of time. These results confirm that the CN-PPV nanoparticles produced by the nebulization technique are negatively charged with an excess charge ranging from two to ten electrons. This suggests that these particles could be attached to a conducting surface with an appropriate cationic coating. Using a metal-coated biased cantilever, individual nanoparticles could be addressed to study the I-V characteristics of these nanostructures.

Summary and Conclusions

Our results provided definitive proof that the semiconducting nanoparticles produced by the nebulization technique are negatively charged with an excess charge ranging from two to ten electrons.[9] This value is in good agreement with values estimated from Rayleigh stability limits for a particle of this size. These results suggests that these particles could be attached to a conducting surface with an appropriate cationic coating. Using a metal-coated biased cantilever, individual nanoparticles could be addressed to study the I-V characteristics of these nanostructures. Many questions remain: Are specific charge states (higher or lower) correlated with photochemical properties? How does the chemical potential (electron affinity) depend on charge state? This question is of particular importance in relation to nanoscale optoelectronic device functionality. While our experimental path diverged somewhat from our original proposal, we have made significant progress in our microscopic understanding of the nature of these highly novel polymeric species and the results described here provide a solid scientific foundation for further investigation.

References

[1]A. J. Heeger, "Semiconducting and Metallic Polymers: The Fourth Generation of Polymeric Materials," *J. Phys. Chem. B* **105**, 8475 (2001).

[2]J. M. Tour, "Molecular Electronics: Synthesis and Testing of Components," *Acc. Chem. Res.* **33**, 791 (2000).

[3]T. W. Hagler, K. Pakbaz, and A. J. Heeger, "Polarized-Electroabsorption Spectroscopy of a Soluble Derivative of Poly(P-Phenylenevinylene) Oriented by Gel Processing In Polyethylene- Polarization Anisotropy, the Off-Axis Dipole Moment, and Excited State Delocalization," *Phys Rev. B* **49**, 10968 (1994).

[4]T. Q. Nguyen, J. J. Wu, V. Doan, B. J. Schwartz, and S. Tolbert, "Control Of Energy Transfer In Oriented Polymer-Mesoporous Silica Composites," *Science* **288**, 652 (2000).

[5]P. Kumar, A. Mehta, M. Dadmun, J. Zheng, L. Peyser, R. M. Dickson, T. Thundat, B. G. Sumpter, and M. D. Barnes, "Observation of narrow-bandwith spontaneous luminescence from oriented conjugated polymer nanostructures," *J. Phys. Chem. B* **107**, 6252–6257 (2003). [Letter to the Editor]

[6]A. Mehta, P. Kumar, M. Dadmun, J. Zheng, R. M. Dickson, T. Thundat, B. G. Sumpter, and M. D. Barnes, "Oriented cylindrical nanostructures of a semiconducting polymer: Polarization evidence for highly ordered individual macromolecular structures," *Nanoletters* **3**(5), 603–607 (2003).

[7]J. Hu, L-S. Li, W. Yang, L. Manna, L-W. Wang, and A. P. Alivisatos, "Linearly polarized emission from colloidal semiconductor quantum rods," *Science* **292**, 2060 (2001).

[8]M. D. Barnes, B. G. Sumpter, and D. W. Noid, "Polymer-blend microparticles: A new approach to nanoscale composites with tunable properties," *Materials Today* (invited) **2**(3), 25–27 (1999).

[9]A. Mehta, P. Kumar, T. Thundat, and M. D. Barnes, "Investigation of static charge states of oriented semiconducting polymer nanostructures," to be published in *Applied Physics Letters.*

Synthesis of Highly Textured Ternary Carbide Compounds for Power Generation and Other Industrial Applications

E. Lara-Curzio, T. R. Watkins, C. A. Blue, M. Radovic, and S. Waters
Metals and Ceramics Division

This project focused on the synthesis of highly textured ternary compounds of Ti, Si, and C. These compounds, such as Ti_3SiC_2, have been shown to have excellent physical and mechanical properties for applications at elevated temperatures. Furthermore, surfaces containing the basal planes of the crystalline structure of this compound have exhibited a very low coefficient of friction. Such materials would be ideal to reduce parasitic losses in reciprocating engines that would operate at higher temperatures.

Attempts to extrude cylindrical bodies of Ti_3SiC_2 using ORNL's 1200-ton press were not successful because of the temperature limitations of the system. However, subsequent efforts to extrude cylindrical objects using a press with higher temperature but lower force capabilities were partially successful and provided indications of the possibility of achieving preferential crystallographic orientation of the basal planes Ti_3SiC_2, through hot extrusion. These subsequent experiments also allowed the identification of processing parameters for subsequent research.

Introduction

During the 1980s and 1990s, significant efforts were focused on developing monolithic ceramics to manufacture components for more efficient reciprocating engines (e.g., cam roller followers, intake and exhaust valves, turbocharger rotors, exhaust port liners, and pistons). These materials were chosen because of their excellent wear and corrosion resistance and their ability to retain their mechanical properties at elevated temperatures.[1] Yet, the widespread use of monolithic ceramics in reciprocating engines has not been realized because of high manufacturing costs and concerns about their reliability.

Ti_3SiC_2, which belongs to a class of materials known as MAX phases, might possess the necessary combination of properties to overcome the limitations exhibited by monolithic ceramics and thus enable the development of more efficient reciprocating engines and industrial applications. MAX phases are made up of an early transition metal (M), an element from an A group in the periodic table (A), and either carbon or nitrogen in the composition $M_{n+1}AX_n$ where n is 1, 2, or 3. These materials are layered with a hexagonal crystallographic structure in which $M_{n+1}X_n$ layers are interleaved with layers of pure A.[2–3]

It has been reported that the coefficient of friction of Ti_3SiC_2 on surfaces containing its basal planes is less than 5×10^{-3} and that this ultra-low value persisted even after exposure to ambient air for several months.[4–5] These results are comparable to, and potentially lower than, the lowest coefficient of friction measured on any solid lubricant surface. This unique property of Ti_3SiC_2, along with its high specific stiffness and strength, good thermal conductivity, and machinability make it an ideal candidate material for the manufacture of intake and exhaust valves and valve guides for reciprocating engines, for example.

This project focused on demonstrating the feasibility of synthesizing highly textured Ti_3SiC_2 by hot extrusion using ORNL's 1200-ton press. The objective of this project was to demonstrate the feasibility of forcing the alignment of the basal planes of the crystalline structure of this compound, parallel to the outer surface of extruded bodies, in order to achieve surfaces with low coefficient of friction. The demonstration of such technology could enable the manufacture of intake/exhaust valves and other reciprocating engine components, and in turn, contribute towards the development of higher efficiency engines and industrial processes.

Technical Approach

Dense, polycrystalline bodies of Ti_3SiC_2 have been synthesized by milling Ti, C, and SiC powders followed by cold-pressing and reactive hot-pressing.[2–3] By varying the hot-pressing temperature and time, the average grain size can be controlled. However, the grains in the resulting material are oriented randomly. The objective of this project was to demonstrate the feasibility of synthesizing highly textured polycrystalline bodies of Ti_3SiC_2 that had the crystalline basal planes oriented parallel to their outer surface.

Fig. 1. Photograph of hot-extruded Ti_3SiC_2 in a tantalum-lined 304 stainless steel can. The extrusion products had tears and broke in several pieces.

It has been documented that during extrusion, or during other processes that involve shearing of viscous fluids, anisometric particles align so that their long axis is parallel to the extrusion direction due to shear developed between the extrusion nozzle and the material being extruded.[6] In crystalline materials, slip planes are usually the planes with the highest density of atoms. In the case of hexagonal crystals slip will occur on the basal planes. Therefore, during hot extrusion, when the material can deform plastically, deformation will be easiest along the basal planes, which will align parallel to the extrusion direction. For example, pronounced textures have been achieved through the hot extrusion of superconducting compounds of $YBa_2Cu_3O_x$ and $Bi_2Sr_2CaCu_2O_{8+X}$ where the basal planes became aligned along the direction of extrusion.[7–8]

To achieve the objective of this project, a series of hot extrusion runs were carried out using ORNL's 1200-ton extrusion press. Starting powders of Ti_3SiC_2 with particle size of 1–5 µm were canned under vacuum (>4 × 10^{-4} torr) inside tantalum-lined 304 stainless steel or molybdenum cans, which were subsequently sealed by electron-beam welding. Extrusion runs were carried out after the cans had been heated inside a furnace at temperatures between 1100°C and 1300°C for 1 h. Additional attempts to extrude Ti_3SiC_2 were carried out using a hot-press with higher temperature capabilities, but lower force capacity. In this case, conical dies were manufactured with three different extrusion ratios between 1:2.6 and 1:4 and an angle of 60° using high-strength graphite. The dies were 127 mm in diameter and 171 mm in length. To minimize friction, the die was lined with a 50-µm thick layer of Graphoil®. Hot extrusion runs at temperatures as high as 1700°C were carried out and the microstructure of the resulting materials was characterized using conventional metallographic techniques and X-ray diffraction methods for phase identification.

Results and Accomplishments

Attempts to extrude Ti_3SiC_2 at temperatures between 1100°C and 1300°C and with forces as high as 500 tons were unsuccessful using ORNL's 1200-ton press. One-half of the cans that were prepared failed to extrude through dies with diameters of either 12.5 mm or 15.8 mm. The remaining extrusions had tears or broke in several pieces after exiting the die and revealed poor consolidation of the Ti_3SiC_2 powders (Fig. 1). These results suggested that the temperatures used were not sufficiently high to consolidate the powders and to allow for creep/plastic flow. Although the furnace used to heat up the cans before extrusion can operate in excess of 1300°C, there aren't many materials to fabricate cans capable of withstanding temperatures above 1300°C in air.

The failure to hot-extrude Ti_3SiC_2 using ORNL's 1200-ton extrusion press prompted the search for alternative strategies to accomplish the objectives of this project. Additional hot-extrusions were carried out using a hydraulic press equipped with a graphite furnace capable of 2000°C in vacuum or inert environment. Extrusion experiments were carried out in two steps using this system. In the first step powders were densified at 1400°C in vacuum under an axial force of 10 kN inside a conical graphite mold lined with Graphoil®. This resulted in very dense products. In the second step, the densified bodies were extruded at temperatures between 1400°C and 1700°C and forces as high as 17.5 kN using high-strength conical graphite dies with extrusion ratios between 1:2.6 and 1:4 and an angle of 60° using. The dies were 127 mm in diameter and 171 mm in length. To minimize friction, the die was lined with a 50-µm-thick layer of Graphoil®. Although it was possible to extrude the material (Fig. 2), the amount of extrusion was very small. There was evidence of reaction between the layer of Graphoil® and Ti_3SiC_2, which resulted in the formation of titanium carbide. An X-ray diffraction analysis also revealed that the intensity of the peak associated with the basal plane on a surface of the extruded body parallel to the extrusion direction was 3.5 times larger than the intensity of the peak associated with this plane on a surface perpendicular to the extrusion direction (Fig. 3).

While the results from this investigation have demonstrated the possibility of extruding Ti_3SiC_2, albeit in a small amount, and the preferential alignment of its crystalline planes, they also showed the good resistance of Ti_3SiC_2 to creep deformation, which should be considered a good trait. The ability to hot-extrude Ti_3SiC_2 could be improved by using an alternative lubricant (e.g.,

Fig. 2. Photograph of dense Ti_3SiC_2 body after hot-extrusion at 1400°C in a graphite die using a hydraulic press and a graphite furnace.

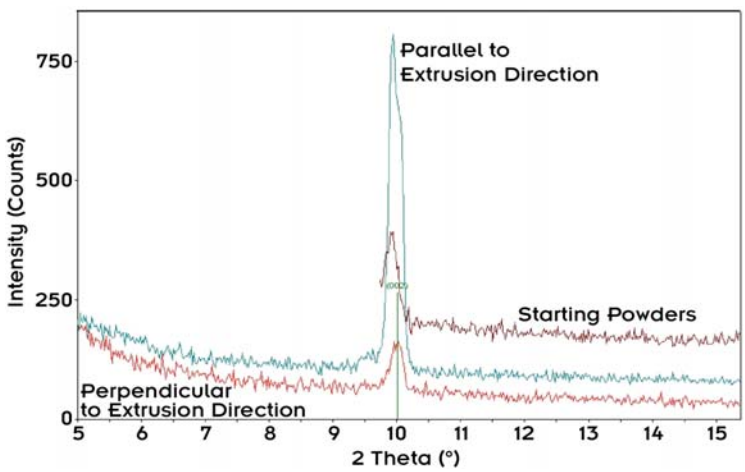

Fig. 3. X-ray diffraction patterns obtained from surfaces parallel and perpendicular to the extrusion direction. The intensity of the basal plane peaks for surfaces parallel to the extrusion direction were 3.5 times larger than that associated with this plane on a surface perpendicular to the extrusion direction.

BN) to reduce reactivity of the material with graphite, and by hot-extruding the material in several steps with a small extrusion ratio in each step. While the creep deformation of materials is a temperature-activated process, higher temperatures also promote grain growth in Ti_3SiC_2, making it more creep resistant and more difficult to extrude. This study has identified the range of temperature and stresses needed to facilitate the hot-extrusion of Ti_3SiC_2.

Summary and Conclusions

Attempts to extrude Ti_3SiC_2 using ORNL's 1200-ton press at temperatures between 1100°C and 1300°C were unsuccessful. Subsequent attempts to hot-extrude sintered powders of Ti_3SiC_2 using a hydraulic press equipped with a high-temperature furnace resulted in bodies with crystalline texture, but the amount of extrusion was limited. This is attributed to the good creep resistance of the material and the lack of force capacity of the press used for these experiments. However, the range of operating conditions to facilitate the hot-extrusion of Ti_3SiC_2 have been identified.

References

[1]U.S. Department of Energy, Energy Information Administration, *Annual Energy Review 1988* (1988)

[2]M. W. Barsoum and T. El-Raghy, "The MAX Phases: Unique New carbide and Nitride Materials," *American Scientist* **89**, 334–343 (2001).

[3]T. El-Raghy and M. W. Barsoum, "Processing and Mechanical Properties of Ti_3SiC_2:I, Reaction Path and Microstructure Evolution," *J. Am. Ceram. Soc*. **82**, 2849–54 (1999).

[4]A. Crossley, E. H. Kisi, J. W. B. Summers, and S. Myhra, "Ultra-low friction for a layered carbide-derived ceramic, Ti_3SiC_2, investigated by lateral force microscopy (LFM)," *J. Phys. D: Appl. Phys*. **32**, 632–638 (1999).

[5]S. Myhra, J. W. B. Summers, and E. H. Kisi, "Ti_3SiC_2—A layered ceramic exhibiting ultra-low friction," *Materials Letters* **39**, 6–11 (1999).

[6]S. Y. Lienard et al., "Texture Development in Si_3N_4/BN Fibrous Monolithic Ceramics," *J. Mater. Sci*. **35**, 3365–3371 (2000).

[7]I-W. Chen et al., "Texture Development in $YBa_2Cu_3O_x$ by Hot Extrusion and Hot Pressing," *J. Am. Ceram. Soc*. **70**, C388–C390 (1987).

[8]X. Wu and I-W. Chen., "Hot Extrusion of Ceramics," *J. Am. Ceram. Soc*. **75**, 1846–53 (1992).

Microscale and Mesoscale Strain Measurements in Cement-Based Materials

C. R. Hubbard,[1] J. J. Biernacki,[1,2] and J. Bai[1,3]
[1]*Metals and Ceramics Division*
[2]*Tennessee Technological University*
[3]*University of Tennessee*

Understanding the microscale and mesoscale load bearing and load transfer characteristics of concrete could revolutionize the way that this complex heterogeneous material is engineered. Synchrotron X-rays were used to make measurements of microscale strains under mechanically generated stresses. Stressors were applied by in situ loading of specimens, and diffraction measurements were made to establish the stress states of various crystalline phases including calcium hydroxide, unreacted clinker phases, and aggregate phases.

Introduction

Concrete is the ubiquitous building material used in virtually every inhabited environment on earth. Despite concrete's benefits of low initial cost, formability, and field fabricability, there are numerous durability-related problems that limit the practical lifespan and life-cycle cost- effectiveness. The four primary mechanisms of degradation are (1) mechanical, (2) thermal, (3) chemical, and (4) drying in origin. While fundamentally different, these four families of *stressors* manifest in the generation of loads (stresses) that result in strains (deformations) that lead to formation of cracks and ultimately to failure.

The goal of this research is to develop and demonstrate experimental techniques that utilize ORNL's strength in synchrotron facilities to study mechanically induced stresses in cement, mortar, and concrete on a mesoscale and microscale. The diffraction experiment provides a direct measurement of the lattice spacings of each phase of a material. These spacings change as a function of mechanical, thermal, or chemical effects. Diffraction techniques provide direct measures of strains in individual phases and can also discriminate between tensile and compressive deformation.

Portland cement concrete is comprised of aggregate, cement paste, and water-filled or partially filled porosity. Both the aggregate and cement paste are themselves heterogeneous in nature, aggregate typically being sand (fine) and whatever rock (coarse) is locally available, and the paste being comprised of hydrated and unhydrated cement. The unhydrated cement fraction includes tricalcium silicate, dicalcium silicate, tricalcium aluminate, tetracalcium aluminoferrite, and gypsum.The hydrated cement fraction includes calcium silicate hydrate, calcium hydroxide, monosulfoaluminate, and ettringite, the respective hydration products of the anhydrous phases.

Research on fracture processes in concrete and other quasi-brittle materials shows that cracks initiate as micro-scale features.[1] As damage progresses, the scale and number of defects increases. Eventually the number density and size of defects grows such that the microscale and now mesoscale cracks merge to form macro flaws leading to complete failure. Prior research has focused on the measurement of macroscopic stress and strain measurements to interpret the cumulative effect of microscale degradation mechanisms. For example, macroscopic shrinkage measurements due to drying of concrete have been combined with macroscale constitutive relationships to predict drying shrinkage cracking in constrained concrete. Until now, virtually no direct measurements of the microscale strain states and strain distributions have been made for cement, mortar, or concrete.

Schulson et al.[2] recently demonstrated that stress levels within hardened cement paste subject to thermal loads could be quantified by measuring strains in the calcium hydroxide (CH) phase using neutron diffraction. Furthermore, their work demonstrated that stress distributions on a microscale are anisotropic. Although they were unable to measure strain levels and stresses developed upon freezing due to lack of instrumental resolution, Schulson et al.[3] also demonstrated that neutron diffraction can be used to study ice formation in cement paste.

Technical Approach

ORNL facilities at the National Synchrotron Light Source (NSLS) are suited for this research. The high flux and highly parallel X-ray beam at X14A makes it far superior to conventional laboratory X rays and results in extremely high resolution and flux needed for measuring very small strains.

Sample Preparation

Type I ordinary Portland cement meeting ASTM C150 specifications and Ohio River sand were blended in the appropriate proportions with tap water to form samples of cement paste, mortar, and concrete. Since the hardened test specimens were to be cubes no larger than 7.6 mm on a side, the particle size of the sand was separated into suitable fractions to produce mortar and concrete samples with workable aggregate distributions. Cement paste samples were prepared using a water/cement (w/c) ratio of 0.34. The Portland cement was mixed by hand with the water until a uniform paste was formed. The paste was then cast into a 1.9-cm-diameter glass jar to a level of about 5 cm. The jar was sealed and placed into a constant temperature water bath at 35°C.

Sand with particle size <425 µm was used to produce mortar samples (primarily quartz or Q). An aggregate (sand)-to-cement ratio (a/c) of 2.0 was used with a w/c of 0.45. The higher w/c ratio was necessary to provide a workable mortar mixture. Mortar mixtures were prepared by hand, sealed in glass jars, and cured at 35°C.

Concrete specimens were made by separating the river sand into two fractions and reconstituting it in proportions that would be more representative of a simulated concrete. Since the test specimen size is smaller than most single coarse aggregate particles, the concrete had to be prepared by blending the coarse fraction of the sand with the fine fraction of the sand to make a reasonable simulation. The sand was separated into <425-µm and >425-µm fractions. A simulated aggregate blend was made by reconstituting these fractions in an x/y ratio of coarse to fine fractions. The aggregate blend was then mixed with cement in an a/c ratio of 2.0 and with water at a w/c of 0.45. The components were mixed by hand, cast into glass jars, and cured at 35°C.

The specimens were cured in the sealed environment for at least 28 days, after which time they were removed from their jars and cut into 7.6-mm cubes using a diamond saw.

X-Ray Experiments

X-ray strain experiments were performed using beamline X14A at NSLS at a wavelength of 1.5425 Å (energy of 8.0377 keV, nominally equivalent to CuK_α) with a Ge analyzer crystal. The X-ray goniometer was fitted with a small load frame capable of applying up to 500 lb_f. Strain data was collected for one mortar and two cement samples. Θ-2Θ scans were made at various applied loads between zero and 500 lb_f for $2Q$ between 124 and 134°. This range was used because it contains two calcium hydroxide (CH) peaks, two quartz (Q) peaks, and one calcium carbonate (C) peak at angles 2Θ = 126.8660°, 130.430°, 127.537°, 131.516°, and 128.262°, respectively (d-spacings of 0.8623, 0.8496, 0.8598, 0.8458, and 0.8571 Å). These diffraction peaks are associated with hkl planes (3 1 0)-CH, (2 1 4)-Q, (3 0 5)-C, (1 1 6)-CH and (2 3-10)-Q. This rather high 2Θ range was selected since peak shift increases with increasing 2Θ for a constant applied load. X-ray scans were performed in sequences of load, no load, load or no load, load, no load to replicate conditions and observed changes in strain states due to sequential stressing.

A procedure called Y tilting was used to obtain the in-plane stress. Since a free surface is required for Θ-2Θ scanning, the load was applied in the sample plane (perpendicular to the diffraction vector when the tilt angle is zero). Θ-2Θ scans were performed at Ψ angles of zero, 25.66, 37.76, 48.59, and 60°. This creates a series of five equally spaced $sin^2\Psi$ values for the given five Ψ angles. In some cases additional Ψ angles selected from the following series; 22.52°, 32.03°, 32.8°, 41.56°, 43.21°, 50°, and 54.11° were also scanned.

Data Analysis

The strain measured in the laboratory reference frame ε'_{33} is related to the strain in the lattice reference frame ε_{33} according to the following equation:

$$(\varepsilon'_{33}) = \frac{d_{\phi\Psi} - d_0}{d_0} = \varepsilon_{11} \cos^2\phi \sin^2\Psi + \varepsilon_{12} \sin 2\phi \sin^2\Psi +$$

$$\varepsilon_{22} \sin^2\phi \sin^2\Psi + \varepsilon_{33} \cos^2\Psi + \varepsilon_{13} \cos\phi \sin 2\Psi + \varepsilon_{23} \sin\phi \sin 2\Psi \quad (1)$$

where $d_{\phi\Psi}$ = the measured strained d spacing, d_0 = the measured unstrained d spacing, ε_{ij}= the lattice strains in directions 1, 2, and 3, ϕ = the angle of rotation of the sample about laboratory direction 3, and Ψ= the laboratory tilt angle. As a result, the observed strain ε'_{33} can be a complex function of $sin^2\Psi$.[4] Three functional behaviors are possible: (1) linear, (2) nonlinear split, and (3) nonlinear oscillating.

Diffraction d-spacings ($d_{\phi\Psi}$) were determined using profile fitting and Bragg's Law. Each 2Θ range was fit assuming a pseudo-Voigt peak form with either constant or variable peak width. The apparent strain was computed using the left-hand side of Eq. (1). All strains were referenced to the Ψ = 0.0°; no load condition (taken as d_o). The strains, so determined, were then plotted as a function of the $sin^2\Psi$ for conditions of load and no load.

Results and Accomplishments

Strain in Cement Specimens

Plots of strain as a function of $sin^2\Psi$ were made for each of the samples tested—two cement cubes and one mortar cube. Cement sample 1 was tested in an initial no load, load, no load, load sequence with loads of roughly 10 lb_f, 250 lb_f, 20 lb_f and 300 lb_f, respectively. The initial no load data, however, was limited to a single Ψ angle of 0.0°. Figures 1 and 2 summarize the results. Figures 1(a) through 1(e) include $sin^2\Psi$ plots for two peaks associated with CH (d = .8623 and .8496, 2Θ = 126.866 and 130.430°), two peaks associated with quartz (d = .8598 and .8458, 2Θ = 127.537 and 131.516°), and one peak

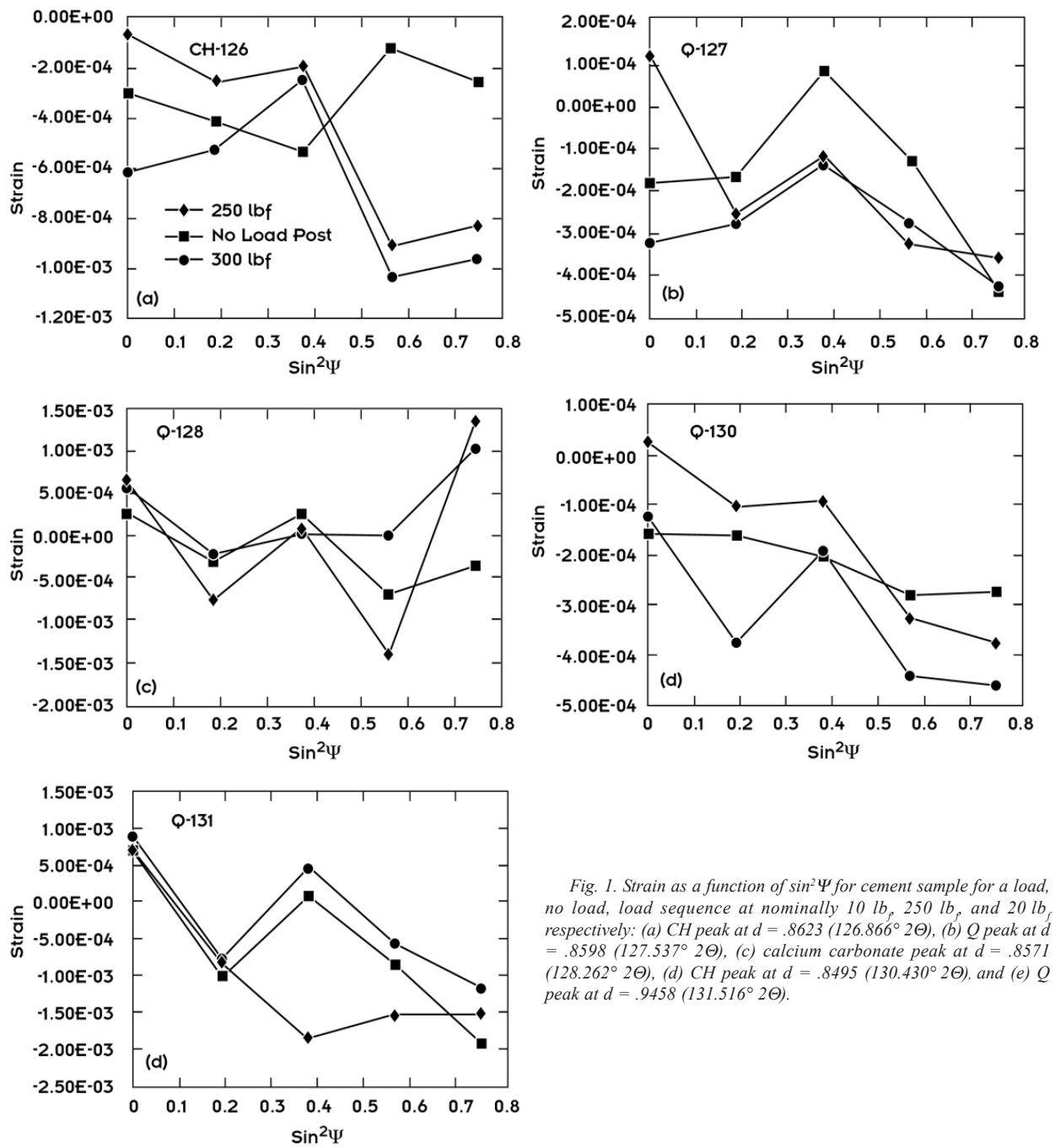

Fig. 1. Strain as a function of $sin^2\Psi$ for cement sample for a load, no load, load sequence at nominally 10 lb_f, 250 lb_f, and 20 lb_f respectively: (a) CH peak at d = .8623 (126.866° 2Θ), (b) Q peak at d = .8598 (127.537° 2Θ), (c) calcium carbonate peak at d = .8571 (128.262° 2Θ), (d) CH peak at d = .8495 (130.430° 2Θ), and (e) Q peak at d = .9458 (131.516° 2Θ).

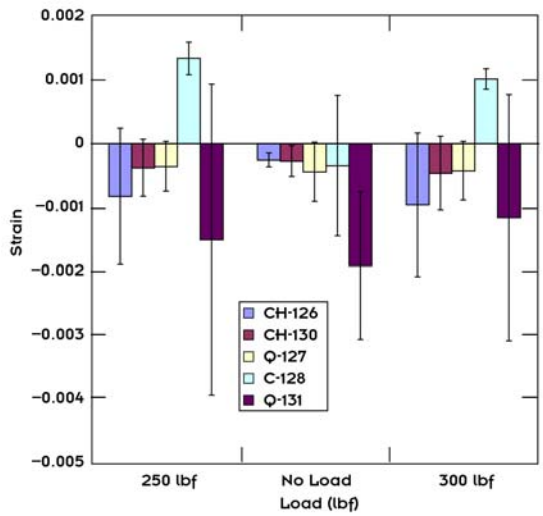

Fig. 2. Strain at $\Psi = 60°$ as a function of load for cement Sample 1 for various CH, Q, and calcium carbonate peaks.

associated with calcium carbonate (d = .8571, 2Θ=128.262°). Figure 2 is a bar chart comparing the strain at $\Psi = 60°$ for the load, no load, load sequence all referenced to the initial no load d-spacings at $\Psi = 0.0°$.

Figure 1 suggests that the strain behavior for hardened cement paste is of a complex nonlinear form. Although the diffraction peaks used are from different phases and different hkl planes, it is expected that the strain behavior would be qualitatively similar, albeit the absolute strains may differ due to crystal anisotropy. While complex and somewhat variable, the general trend in the $sin^2\Psi$ plots is the same for the CH and Q peak pairs, Figures 1(a) and 1(d), and 1(b) and 1(e). When loaded, CH exhibits a larger oscillatory strain behavior, as a function of $sin^2\Psi$, than when unloaded. When the load is removed, the behavior suggests some level of compressive residual loading (relative to the no load $\Psi = 0.0°$ d-spacing) which may be somewhat oscillatory in nature. Most distinct is the repeatability of the compressive strain state noted for $\Psi = 60°$ (Fig. 2). Finally, when loaded, the strain behavior, while similar on repeated cycles, appears to vary some from cycle to cycle, suggestive of plastic deformation in some of the phases in the concrete. This, however, is difficult to establish at this time since, in this case, only two no-load load cycles were recorded.

The quartz peak pair illustrates a similar oscillatory $sin^2\Psi$ behavior. Again, similarities are shared between the peak pairs. Consistent with CH, the strain behavior appears to change with load cycle. The strain state at $\Psi = 60°$ is also consistent and appears repeatable for both peaks (Fig. 2).

A single carbonate peak was observed. Again the strain behavior appears to change from load to no load and with loading cycle. As for CH and Q, calcium carbonate displays a distinct and repeatable change in strain state most evident at $\Psi = 60°$ (Fig. 2).

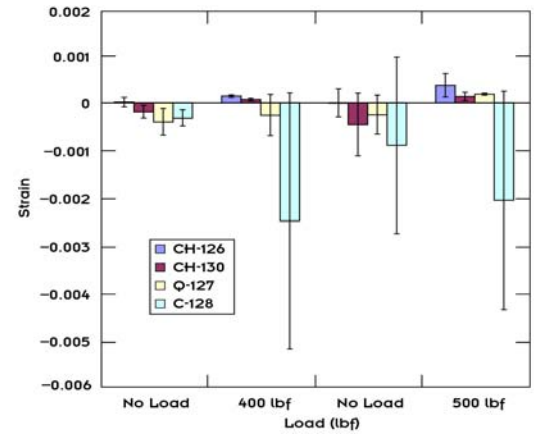

Fig. 3. Strain at $\Psi = 60°$ as a function of load for cement sample 2 for various CH, Q and calcium carbonate peaks.

A second series of experiments was also conducted on a different cement sample. Figure 3 summarizes the strain response for the same series of CH, Q, and calcium carbonate peaks for a no-load/load/no-load/load sequence. Again the results suggest a somewhat variable yet repeatable pattern of changing strain states with changing stress states. Detailed plots of strain as a function of $sin^2\Psi$ are similar to those for cement Sample 1 shown in Fig. 1.

Strain in Mortar Specimens

A single mortar specimen was tested in a no-load, load, no-load cycle. While the results are similar to those found for the cement sample, they are also somewhat more ambiguous. Figure 4 summarizes the strain response for $\Psi = 60°$. Again, the responses appear systematic except for the calcium carbonate peak that was difficult to resolve in the presence of the strong Q peaks in mortar. Although

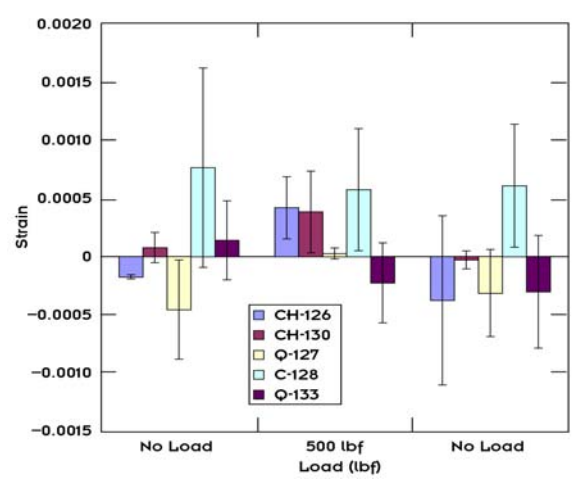

Fig. 4. Strain at $\Psi = 60°$ as a function of load for mortar Sample 1 for various CH, Q and calcium carbonate peaks.

for the calcium carbonate peak that was difficult to resolve in the presence of the strong Q peaks in mortar. Although systematic with no-load, load, no-load cycle, both the Q peak pair and CH peak pair demonstrate compressive behavior for one hkl plane and tensile behavior in the other. At this time it is unclear if there is a physical interpretation for this response. Furthermore, since standard construction grade sand was used, the sand was not *pure* quartz and appears to contain a variety of other compounds that interfere in the 124° to 134° 2Θ range scanned.

Summary and Conclusions

These results, while based on limited experiments, support the proposed hypothesis that strain states in several phases in Portland cement–based materials can be measured using synchrotron X-ray diffraction methods. Further, it clearly demonstrated that the response of different phases are different and that understanding stressors in cements requires such a microscale probe. Based on this research, current efforts to develop models that aim to predict crack initiation due to applied loads or other stressors must include the response of each phase instead of assuming a bulk average.

The variability is possibly due to the low depth of penetration of ~1.54-Å X rays and the highly parallel beam resulting in a consequential limited number of grains sampled. Further, the limited penetration depth results in the X-ray probe sampling just near surface grains. Possible solutions could be improved methods to involve more grains contributing to the X-ray results via oscillation of the sample and/or use of higher-energy X rays. Another alternative is to use neutron diffraction methods due to the far greater depth of penetration of neutrons. However, for neutron diffraction the hydrogen should be replaced with deuterium to minimize incoherent background scattering. These approaches will be included in follow-up proposals.

The development and demonstration of synchrotron-based diffraction techniques to quantify mesoscale and microscale stress and strain behavior in concrete has broad reaching application-based implications. The concrete industry has recently prepared a vision document and a draft technology roadmap in which they identify specific research needs.[5,6]

Among the needs identified in Roadmap 2030 as "high priority items" are development of "new materials to reduce shrinkage and cracking," "reduction of alkali-silica reactions in concrete," "prediction methods and models for . . . cracking, durability and performance (including environmental interaction)," "tools and data for quantifying benefits of using alternative materials," and "multiscale modeling to connect microstructure with engineering properties." Each of these areas and others can benefit from the synchrotron method and the proposed neutron diffraction method. Once fully developed, the phase-sensitive nondestructive analytical methods would enable a researcher to test the microscale impact of prospective shrinkage-reducing admixtures on stress and strain development. For the first time, researchers could study the impact that chemical modification of cement has on alkali-silica interaction-induced stresses. Further, the experimental data could be used to validate and evolve multiscale model development for prediction of cracking, durability, and performance as they relate to interactions such as sulfate, alkali-silica, freeze-thaw, and other environmental stressors.

The joint TTU/ORNL team lead by PI Biernacki (TTU) has secured follow-on funding through the National Science Foundation (NSF) for a three-year $235,000 effort to extend this line of research—specifically to further explore the use of synchrotron XRD and to initiate efforts with neutron diffraction, Raman spectroscopy, and direct microscopic measurement of stressed samples. This project will be conducted in part at ORNL facilities.

References

[1]S. P. Shah, S. E. Swartz, and C. Ouyang, *Fracture Mechanics of Concrete : Applications of Fracture Mechanics to Concrete, Rock and Other Quasi-Brittle Materials*, Wiley, New York (1995).

[2]E. M. Schulson, I. P. Swainson, and T. M. Holden, "Internal Stress Within Hardened Cement Paste Induced Through Thermal Mismatch Calcium Hydroxide versus Calcium Silicate Hydrate," *Cem. Concr. Res.* **31**, 1785–1791 (2001).

[3]E. M. Schulson, I. P. Swainson, T. M. Holden, and C. J. Korhonen, "Hexagonal Ice in Hardened Cement," *Cem. Concr. Res.* **30**, 191–196 (2000).

[4]I. C. Noyan and J. B. Cohen, *Residual Stress Measurement by Diffraction and Interpretation*, Springer-Verlag, New York, pp. 276 (1987).

[5]*Vision 2030: A Vision for the U.S. Concrete Industry*, Strategic, Development Council, American Concrete Institute (2001).

[6]*Roadmap 2030: The U.S. Concrete Industry Technology Roadmap*, Strategic Development Council, American Concrete Institute (Draft, May 10, 2002).

Investigation of Tribological Properties of Graphitic Foam Reinforced Carbon-Carbon Composites

P. J. Blau,[1] J. Qu,[2] J. Klett,[1] and B. Jolly[3]
[1]*Metals and Ceramics Division, ORNL*
[2]*Post-doctoral Research Associate, ORISE, Oak Ridge, TN*
[3]*Pellissippi State Technical College, Knoxville, TN*

Research at ORNL has led to the development of a new class of high-thermal-conductivity carbon foam materials. While the applications of these materials are primarily aimed at rapid heat removal, recent experiments have revealed their potential as bearing surfaces as well. The three primary advantages are (1) they can efficiently remove frictional heat, (2) their natural porosity can trap debris, and (3) the porosity can serve as a lubricant reservoir. A series of pin-on-disk experiments was conducted at room temperature and 400°C to compare the sliding friction and wear characteristics of a densified form of the carbon foam material, mated against M-50 tool steel or alumina, to those of conventional bearing materials such as graphite, bearing bronze, poly-tetrafluoroethylene (PTFE), bearing steel, and a cobalt-based superalloy. At room temperature and under low contact pressure, the tribological behavior of the densified carbon foam material was comparable to that of graphite and better than that of other bearing materials. At 400°C, traditional graphite exhibited a 'dusting' wear regime and experienced a very high friction coefficient. In contrast, the carbon foam demonstrated the ability to maintain low friction and wear at elevated temperature. Further work is needed to elucidate the sliding mechanisms and optimize material properties for high-temperature tribological applications.

Introduction

High-thermal-conductivity graphite foam, developed by researchers at ORNL, has shown considerable promise for use in electronics cooling systems and vehicle radiators.[1] With a thermal conductivity comparable to that for aluminum and one-fifth of that metal's density, this material has the potential to solve thermal management problems in a variety of industrial and military applications. However, in many instances the low density and low strength of the porous foam limit its applicability. In order to overcome the limitations of the as-formed carbon foam, a novel densification process has been developed to improve the density, thermal conductivity, and compressive strength.[2–3]

Certain characteristics of carbon foam, such as its low density, inherent porosity, and attractive thermal properties, suggest the possibility of using it in tribological (sliding bearing) applications. For example, surface-breaking voids have been reported to reduce the friction coefficient by serving as a repository for wear debris[4] or to hold lubricants. The porosity of carbon foam may provide a built-in ability to do these things. Secondly, the maximum operating temperature for the carbon foam is 500°C higher than that for most commercial bearing materials. Thirdly, the high thermal conductivity of the foam could help dissipate frictional heat. This could allow bearings to run at higher speeds without experiencing thermal failure. Finally, the low density of the foam is attractive for weight-sensitive applications and, hence, energy efficiency improvements.

Technical Approach

The friction and wear characteristics of densified carbon foam were measured at room temperature at 400°C for comparison to traditional bearing materials tested under the same conditions. Table 1 lists the composition, density, and Vickers microindentation hardness of the materials used in this research. Friction and wear tests were conducted using a flat-ended pin-on-disc geometry. A custom-built, pin-on-disk testing machine was used. The pin specimen was a bearing ball whose tip was ground and polished to create a flat spot of either 2 or 4 mm in diameter. The use of a flat-ended pin avoided the concentrated contact stresses associated with a spherical tip. Initial tests with rounded pins crushed the ligaments between pores to create a deep wear groove. Tests were conducted at a normal load of 10 N and a sliding speed of 1.0 m/s for a total pin sliding distance of 5000 m. The disk wear tracks were all of the same diameter (21 mm).

It was originally proposed to use a Sub-Scale Brake Tester (SSBT) for high-speed pin-on-disk testing (up to 10 m/s). This required the use of 230-mm-diameter disks, but the large, densified carbon foam disks were not ready for testing by the end of FY 2003. However, large disks

Table 1. Test materials

Specimen	Material designation	Composition/description	Density (g/cm^3)	HV, 100 gf load (GPa)
Pin	M-50 tool steel	Nominal composition (wt%): 0.85 C, 0.10 W, 4.25 Mo, 4.00 Cr, 1.00 V, bal. Fe (Winsted Precision Ball Co., CT)	7.97	9.08
	Polycrystalline alumina	99.5 wt% dense aluminum oxide, ABMA grade 25 ball (McMaster-Carr)	3.90	24.75
Disk	Densified carbon foam	Graphitic foam reinforced carbon-carbon composites, 46% relative density (ORNL—raw foam, SMJ Carbon Technology—densification)	1.26	*N/M*[a]
	Graphite ACF-10Q	Commercial grade, fine-grained graphite, 5 µm particle size, 0.8 µm pore size, 80% relative density (POCO Graphite, TX)	1.80	*N/M*[a]
	Alloy 932 bronze	Nominal composition (wt%): 83 Cu, 7 Sn, 7 Pb, 3 Zn (McMaster-Carr)	8.91	1.34
	PTFE (Teflon)	Virgin electrical grade Teflon™ sheet (McMaster-Carr)	2.14	*N/M*[a]
	AISI 52100 steel	Nominal composition (wt%): 0.95–1.1 C, 1.3–1.6 Cr, 0.2–0.5 Mn, 0.35 max. Si, 0.025 max P, 0.025 max. S (McMaster-Carr)	7.81	8.32
	Stellite 6B	Heat composition (wt%): 1.09 C, 29.58 Cr, 2.75 Fe, 0.06 Mo, 1.48 Mn, 2.66 Ni, 0.01 N, <0.01 P, 0.58 Si, 3.82 W, bal. Co (High Performance Alloys, IN)	8.39	5.26

[a]N/M = not measurable with a Vickers indentation test.

specimens have been obtained and are nearly finished at the time of this report. High-speed tests of the materials are planned for a new follow-on effort which has recently been funded by DARPA.

Results and Accomplishments

Friction and Wear Behavior at Room Temperature

The friction and wear results of the densified carbon foam and other bearing material disks against M-50 tool steel and alumina pins at room temperature are summarized in Tables 2 and 3. The wear factor, as used here, is defined as the wear volume normalized by the applied load and the sliding distance of the pin.

The carbon foam had relatively low friction coefficients, 0.31 and 0.23, for M-50 steel and alumina pins, respectively. The friction coefficient trace was fairly stable and free from significant fluctuations. More promisingly, this material showed fairly high wear resistance. Fracture and a high wear rate, which might have been intuitively expected for foam-structured materials, did not occur. The wear factor of the densified carbon foam disk was relatively low, 5.6×10^{-6} and 1.3×10^{-5} mm^3/N-m for the steel and alumina sliders, respectively. No debris was found on the wear track (Fig. 1), possibly having been trapped by the pores. The worn surface was flat and smooth without evidence of surface damage. The porous macrostructure survived. The swirled microstructure between pores disappeared after the unidirectional sliding test—probably due to the surface crystallites being oriented with their basal planes roughly parallel to the surface. The steel and alumina pins had no measurable wear. A thin film of carbon was formed on the sliders, however, and this helped to stabilize the sliding conditions after a brief running-in period.

Graphite performed similarly to the carbon foam material with even lower friction coefficient and wear rate. The friction coefficient was very stable. The corresponding wear track is shown in Fig. 2. Sliding action smeared the surface and wiped off the porous microstructure, leaving little wear debris. A thin transfer film of graphite on the pin specimens protected the sliders from damage.

Bronze and Teflon disks had relatively low friction coefficients, but high wear rates, as shown in Tables 2 and 3. The friction coefficient traces for bronze and Teflon show higher variations compared to carbon foam or graphite. Large amounts of flake shape debris were collected on the bronze and Teflon disks, evidence of low shear strength which contributed to the low friction and high wear. The tests on 52100 steel and Stellite 6B alloy had high average friction coefficients (0.5 ~ 0.6) with large variations (>±0.1), as shown in Table 2. The contact surfaces on both the pins and disks were damaged, and the wear factors were on the order of $10^{-6} \sim 10^{-5}$ mm^3/N-m. Material removal and deformation were observed on the wear tracks of the 52100 steel and Stellite 6B disks. The pin surfaces were scratched and covered with transferred material.

Table 2. Kinetic friction coefficient

Friction coefficient	Room temperature		400°C
	M-50 steel	Alumina	M-50 steel (test #1,#2)
Carbon foam	0.31 ± 0.005	0.23 ± 0.005	0.15 ± 0.003, 0.57 ± 0.01
Graphite	0.21 ± 0.002	0.24 ± 0.002	1.2 ± 0.2, 0.8 ± 0.1
Bronze	0.19 ± 0.02	0.20 ± 0.03	–
PTFE	0.21 ± 0.01	0.19 ± 0.02	–
52100 steel	0.60 ± 0.08	0.61 ± 0.12	–
Stellite 6B	0.50 ± 0.13	0.56 ± 0.16	0.55 ± 0.06, 0.54 ± 0.04

Table 3. Wear rates of disk specimens[a]

Wear rate (mm^3/N-m)	Room temperature		400°C
	M-50 steel	Alumina	M-50 steel (test #1,#2)
Carbon foam	5.6×10^{-6}	1.3×10^{-5}	1.8×10^{-5}, 1.7×10^{-5}
Graphite	1.0×10^{-6}	2.5×10^{-6}	1.6×10^{-5}, 2.2×10^{-5}
Bronze	2.8×10^{-4}	2.9×10^{-4}	–
PTFE	1.1×10^{-3}	1.0×10^{-3}	–
52100 steel	7.5×10^{-6}	1.6×10^{-5}	–
Stellite 6B	5.8×10^{-5}	7.6×10^{-5}	3.5×10^{-7}, $<1.0 \times 10^{-7}$

[a]Typical wear rates of bearing materials for unlubricated sliding should be less than ~10^{-5} mm^3/N-m. Values for well-lubricated sliding should be less than ~10^{-7} mm^3/N-m.

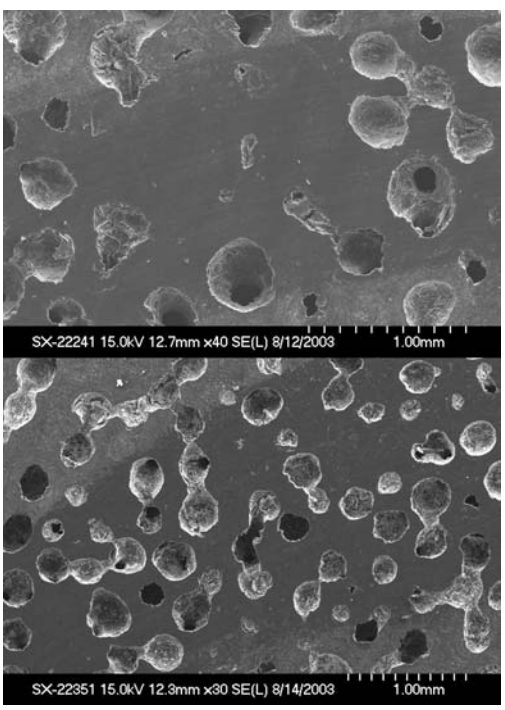

Fig. 1. SEM images of wear tracks on densified carbon foam disks at room temperature (top) and 400°C (bottom).

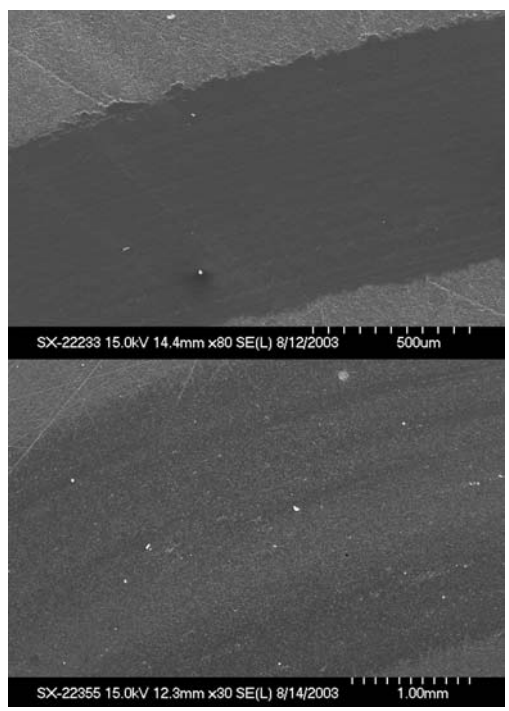

Fig. 2. SEM images of wear tracks on graphite disks at room temperature (top) and 400°C (bottom).

Notably, there was a lower friction coefficient for the alumina pin than for the M-50 steel pin against the carbon foam disk. In contrast, the friction coefficient for the alumina pin against other disk materials was comparable or slightly higher than that for the M-50 steel.

Friction and Wear Behavior at Elevated Temperature

Friction and wear tests were also conducted at 400°C in ambient air. Due to softening and oxidation problems, bronze, Teflon, and 52100 steel cannot be used at temperatures higher than about 300°C. Consequently, graphite and Stellite 6B were used as a basis for comparison with the densified foam. The slider was an M-50 tool steel pin with a 4 mm-diameter flat contact surface.

Graphite and carbon-carbon composite materials may significantly deteriorate their tribological properties in vacuum,[5] inert gases,[6] or elevated temperature,[7] by showing high friction coefficients (0.4 ~ 1.0) and high wear rates. The propensity of carbon materials to expel clouds of fine wear particles is known as "dusting." It is now widely accepted that the self-lubricating properties of graphite are environmentally dependent, and the shear strength along the basal planes is lowered only in the presence of moisture, oxygen, or certain other gases that can be adsorbed into the graphite structure.[8–9]

A critical temperature for graphite and carbon-carbon composites to transition to dusting has been reported in the range of 150 ~ 200°C,[7] above which high friction and wear occur due to the desorption of water. In this study, however, high wear rates were not produced in 400°C tests on either the graphite or the densified carbon foam. Further study of the surface chemistry of sliding films is needed and will be pursued in follow-on efforts. The densified carbon foam exhibited a very low friction coefficient in just one of the two high-temperature tests, and while results demonstrate that low friction is possible, it still remains for us to learn how to achieve such low friction repeatedly.

As shown in Tables 2 and 3, graphite had very high friction coefficient, $\mu = 1.2$ and 0.8, but relatively low wear factors, 1.6×10^{-5} and 2.2×10^{-5} $mm^3/N\text{-}m$, in the two tests at 400°C. The friction coefficient trace of test #2 is shown in Fig. 3. There was a low-friction running-in stage ($\mu = 0.04 \sim 0.16$), apparently from residual water vapor in the surface porosity, then μ increased quickly as the water vapor was removed by heating and sliding. The friction coefficient eventually reached steady state (0.8 ± 0.1). Test #1 had similar friction behavior, but the friction coefficient climbed to a surprisingly high level, 1.2 ± 0.2. This indicated strong adhesion in the contact area. The worn surface (Fig. 2) was smooth, with the porous microstructure remaining intact. Smears and deformation were significantly less than that at room temperature, indicating higher resistance to shear at elevated temperature. Two types of debris were observed: very fine black dust and larger-sized shiny particles. According to EDS X-ray analysis, the black dust was carbon generated during dusting and the shiny particles were iron, chromium, and their oxides, worn off the steel slider. Loud noises, which sounded like metal scraping against metal, was generated in the tests of steel against graphite at 400°C.

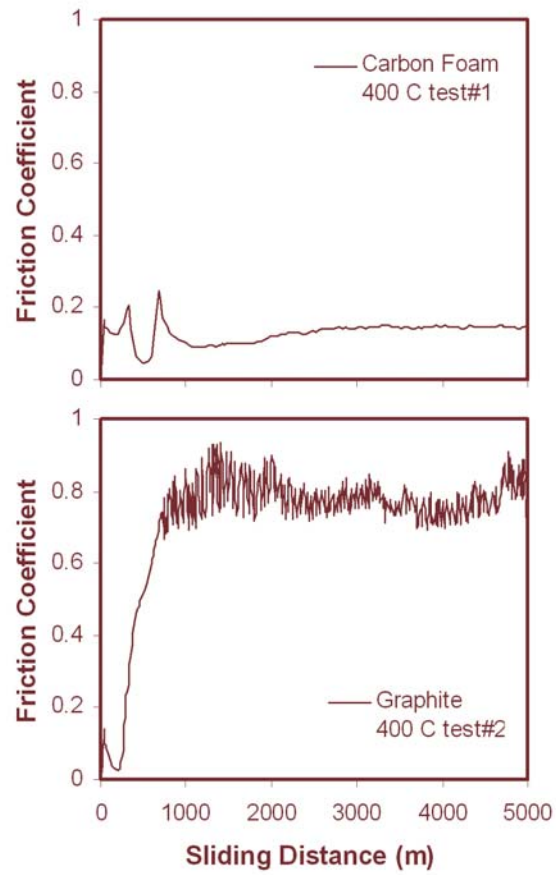

Fig. 3. Friction coefficient traces of densified carbon foam (top) and graphite (bottom) at 400°C.

Similar to the tests on graphite, the tests on the densified carbon foam material also had a low-friction running-in stage. The friction coefficient traces of the two replicates had a similar initial trend, showing double peaks in the range of $\mu = 0.2 \sim 0.25$ and a single valley around $\mu = 0.05$. After the second peak, the two traces headed in opposite directions. The first one (Fig. 3) dipped and stabilized at $\mu = 0.15 \pm 0.003$. The second one (not shown here) rose after 1000-m sliding and eventually transitioned into the dusting regime with $\mu = 0.57 \pm 0.01$ by the end of the test. Despite different frictional behavior, the wear factors for the two tests were low and similar, 1.8×10^{-5} and 1.7×10^{-5} $mm^3/N\text{-}m$, respectively. Results indicate that unlike graphite, the densified carbon foam material does not necessarily transition into a high friction regime at elevated temperature in ambient air. This suggests the

possibility for using carbon foam as a high-temperature bearing material, but the favorable behavior must be made repeatable.

Stellite 6B showed comparable friction and wear behavior at room temperature and 400°C. Energy-dispersive X-ray analysis indicated that the wear track on the Stellite 6B disk was covered by a transfer layer of iron and iron oxides.

Summary and Conclusions

The friction and wear characteristics of a novel, high thermal conductivity, densified carbon foam material were compared with those for several conventional bearing materials at room temperature and 400°C without additional lubrication. High contact stresses can crush the foams, but if the load is distributed over a planar contact region, low friction and wear can be obtained without fracture or chipping problems. At room temperature, the friction and wear rates of carbon foams were comparable to those of graphite and better than those of the other bearing materials we tested. At the elevated temperature, Stellite 6B behaved similarly to room temperature, but graphite exhibited dusting and experienced high kinetic friction coefficients, up to $\mu = 1.2$. In one test against M-50 tool steel at 400°C, the carbon foam material had a low friction coefficient ($\mu = 0.15$), but in a repeated test, it had a high friction coefficient ($\mu = 0.57$). Despite this, the wear factors for both tests were similar. We have shown that it is possible to obtain low friction and wear on the densified carbon foam at elevated temperature. As the sliding mechanisms are clarified, it should be possible to optimize the material properties to obtain low friction and low wear behavior repeatedly. Support from the Defense Advanced Research Projects Agency that resulted from this project will enable such research to be started during FY 2004.

References

[1]J. Klett, R. Hardy, E. Romine, C. Walls, and T. Burchell, "High-Thermal-Conductivity, Mesophase-Pitch-Derived Carbon Foams: Effect of Precursor on Structure and Properties," *Carbon* **38**, 953–973 (2000).

[2]P. G. Wapner, W. P. Hoffman, and S. Jones, *Carbon and Ceramic Matrix Composites Fabricated by a rapid Low-Cost Process Incorporating in-situ Polymerization of Wetting Monomers,* U.S. Patent 6,309,703 (2001).

[3]J. Klett, S. Jones, L. Klett, and C. Walls, "High Thermal Conductivity Graphitic Foam Reinforced Carbon-Carbon Composites," *SAMPE 2003*, May 11–15 2003, Long Beach, California (2003).

[4]A. P. Semenov, "Tribology at High Temperature," *Tribology International* **28**(1), 45–50 (1995).

[5]R. I. Longley, J. W. Midgley, A. Strang, and D. G. Teer, "Mechanism of the Frictional Behavior of High, Low, and Non-Graphitic Carbon," *Lubrication and Wear Convention*, 198–209 (1963).

[6]F. Robert, D. Paulmier, H. Zaidi, and E. Schouller, "Combined Influence of an Inert Gas Environment and a Mechanical Action on a Graphite Surface," *Wear* **181–183**, 670–690 (1995).

[7]B. K. Yen, T. Ishihara, and I. Yamamoto, "Influence of Environment and Temperature on 'Dusting' Wear Transitions of Carbon-Carbon Composites," *Journal of Materials Science* **32**, 681–686 (1997).

[8]J. K. Lancaster and J. R. Pritchard, "The Influence of Environment and Pressure on the Transition to Dusting Wear of Graphite," *Journal of Physics D: Applied Physics* **14**, 747–762 (1981).

[9]M. Brendle and P. Stempe, "Triboreactions of Graphite with Moisture—a New Model of Triboreactor for integrating Friction and Wear," *Wear* **254**, 818–826 (2003).

Tailoring the Properties of Crystalline Solid Solutions by Magnetic and Stress Annealing

E. D. Specht,[1] C. J Sparks,[1] R. K. Williams,[1] and A. Gali[2]
[1]*Metals & Ceramics Division*
[2]*Department of Materials Science and Engineering, University of Tennessee*

It is demonstrated that magnetic annealing affects the atomic short-range order of $FeNi_3$. While this in accord with the commonly accepted model for magnetic annealing of substitutional alloys, annealing is shown to produce order which is *strong* and *isotropic*, while the model predicts a *weak* and *anistropic* affect on short-range order. The Seebeck coefficient is shown to provide a rapid measure of short-range order.

Introduction

The beneficial effects of annealing magnetic materials in magnetic field have been known since 1913.[1] Similarly, magnetic anisotropy can be induced by annealing in a stress field.[2] The commonly accepted model for both these effects is that both these effects are due to local redistribution of atoms creating a *small* preference for atomic pairs oriented to minimize their energy in the magnetic or stress field.[3] In an effort to make the first direct test of this hypothesis, we discovered magnetic annealing conditions which create a *large* increase in atomic short-range order in $FeNi_3$ alloys. This project confirms this increase and measures the Seebeck effect to assess its potential as a rapid screening tool to determine which annealing conditions give rise to enhanced order.

Technical Approach

Samples were annealed using the apparatus shown schematically in Fig. 1. Sealed in a quartz capsule, $FeNi_3$ samples were first heated to high temperature to create local atomic disorder, then heated in vacuum with an applied magnetic field under conditions which lead to large increases in short-range order. One set of control samples was annealed in magnetic field under conditions leading to small increases in short-range order, and another set of control samples was annealed in no magnetic field.

Diffuse X-ray scattering is used as a direct measure of atomic short-range order. At high temperatures, $FeNi_3$ is disordered, with Fe and Ni atoms distributed randomly on an fcc lattice. At low temperatures, $FeNi_3$ forms an ordered L12 crystal with *fundamental* Bragg peaks on the fcc reciprocal lattice points and *superstructure* Bragg peaks on the other cubic reciprocal lattice points. Both these structures have cubic symmetry; the applied field leads to no anisotropy. Samples are annealed so as to produce local order only; the fundamental Bragg peaks then remain sharp, while the superstructure Bragg peaks are broadened into short-range order peaks. The width of the short-range order peaks provides a measure of the length scale of the local order. Any anisotropy due to the applied field is seen as a difference in the intensities of the various superstructure peaks. For example, if the sample orders along the [100] direction, the (100) short-range order peak will be stronger than the (010) or (001) peaks.

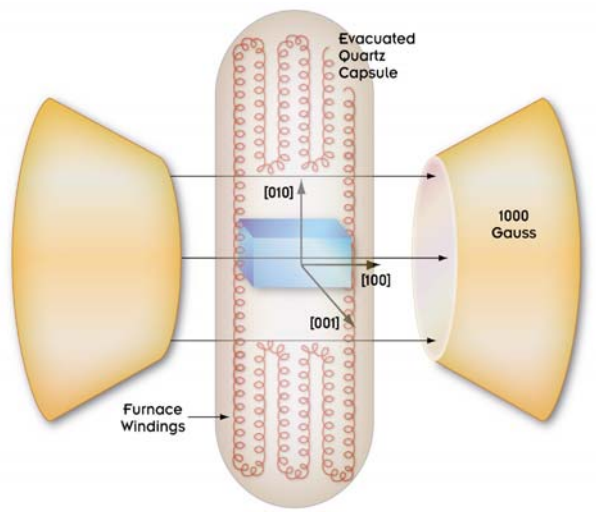

Fig. 1. Apparatus used to anneal $FeNi_3$ in an applied magnetic field.

While diffuse X-ray scattering provides the most direct measure of short-range order, it is a slow measurement which requires the use of synchrotron radiation sources which are very limited in availability.

Seebeck coefficients were measured to assess their value as a rapid probe of short-range order. The Seebeck apparatus is shown schematically in Fig. 2; we followed the procedure described elsewhere in detail.[4] One end of the sample is heated to create a thermal difference of ~1°C. Chromel-alumel thermocouples are attached to the hotter and cooler end of the sample. The voltages of all four leads are measured. The temperature of each end of the sample is calculated from the thermocouple voltages V_{1c}- V_{1a} and V_{2c}- V_{2a} (voltages are defined in Fig. 2). The differences in voltage for each lead material, V_{1a}- V_{2a} and V_{1c}-V_{2c}, are due to the combined Seebeck effect of the thermocouple material and of $FeNi_3$. Subtracting the effect of the thermocouple material leaves the Seebeck voltage of $FeNi_3$; dividing by the temperature difference T_1- T_2 gives two independent measurements of the Seebeck coefficient of $FeNi_3$. Each sample is measured at two temperatures.

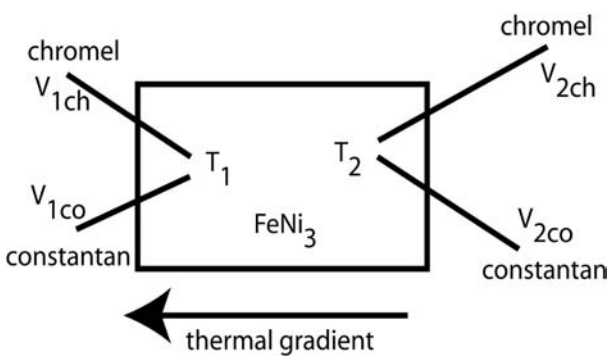

Fig. 2. Apparatus used to measure Seebeck coefficients.

Results and Accomplishments

Diffuse X-ray scattering confirmed our preliminary results. Samples annealed in zero magnetic field show very weak short-range order, barely extending beyond near-neighbor atoms. Annealing conditions which give weak short-range order produce ordering which extends ~0.5 nm. Annealing conditions which give the strongest short-range order produces ordered domains of up to 5 nm.

Repeating these measurements at various superstructure reciprocal lattice vectors, however, yield data which contradicts the commonly-accepted model that magnetic annealing leads to magnetic anisotropy through the local rearrangements of atoms. All the short-range order peaks have the same intensity, within experimental uncertainty of ~5%. Consequently, none of the magnetic anisotropy can be attributed to anisotropic local atomic ordering.

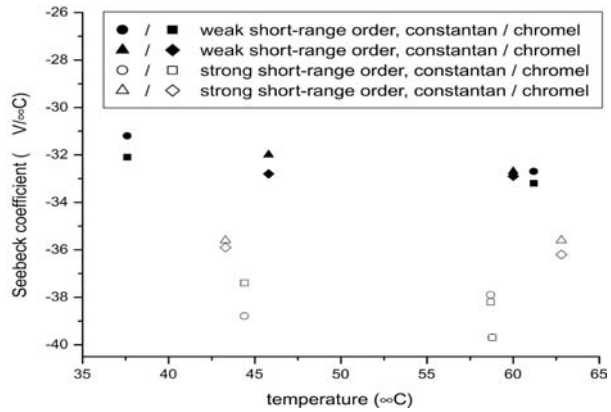

Fig. 3. Seebeck coefficients for $FeNi_3$, measured with both constantan and chromel leads. Two samples are annealed in magnetic fields to give weak short-range order, two to give strong short-range order.

The Seebeck coefficients (Fig. 3) for the samples annealed for weak short-range order are consistent with the results for highly disordered $FeNi_3$, while those for the samples annealed for strong short-range order are between those for disordered and fully ordered $FeNi_3$.[4]

Summary and Conclusions

The effects of magnetic annealing on short-range atomic order in $FeNi_3$ have been confirmed; under the proper conditions, short-range order forms to a far greater extent than in the absence of a field. The isotropic nature of the short-range order, however, is at odds with the prevailing model for magnetic annealing. These studies can form the basis for reassessment of the fundamental mechanisms by which magnetic and stress annealing affect the properties of solid solution alloys. We will pursue funding for this effort from Basic Energy Sciences; successful explanation of the magnetic and stress annealing effects will lead to funding in applied areas.

We have demonstrated that measurement of Seebeck coefficients provides a rapid measure of short-range order, which will greatly facilitate future studies.

References

[1]H. Pender and R.L. Jones, *Phys. Rev.* **1**, 259 (1913).

[2]R. M. Bozorth, *Ferromagnetism*, D. Von Nostrand, New York, 1951.

[3]J. C. Slonezewski, p. 205 in *Magnetism*, Vol. 1, edited by G. T. Rado and H. Suhl, Academic Press, New York, 1963.

[4]J. P. Moore, T. G. Kollie, R. S. Graves, and D.L. McElroy, *J. Appl. Phys.* **42**, 3114 (1971).

Nanoelectronic Devices Made from Doped Nanofibers

J. B. O. Caughman,[1] M. L. Guillorn,[2] D. B. Beach,[3] V. I. Merkulov,[2] L. R. Baylor,[1] and L. F. Allard[4]
[1]*Fusion Energy Division*
[2]*Engineering Science and Technology Division*
[3]*Chemical Sciences Division*
[4]*Metals and Ceramics Division*

The purpose of this project is to understand and develop a process for depositing doped carbon and boron carbonitride nanofibers that will be used to make nanoelectronic devices in a way that will be useful for large-scale manufacturing. Vertically aligned nanofibers are being grown using a high-density plasma-enhanced chemical vapor deposition technique that allows control of gas-phase and surface chemistry. In contrast to current growth methods, the electrical properties of the nanofibers will be controlled by substitutional doping of boron and/or nitrogen to produce metallic or semiconducting doped carbon or boron carbonitride nanofibers. The electrical characteristics of individual vertical nanofibers will be determined by measuring the current flowing through the fiber as a function of applied voltage across the fiber. Nanofiber rectifying devices containing metal-semiconductor (Schottky) junctions will be grown and measured. Our approach for growing nanofibers has advantages over current methods in terms of controlling electrical properties of individual nanofibers, controlling the geometry of the growth, and the potential use as a practical method for realizing vertical integration of dense arrays of nanoelectronics.

One of the main objectives of our project is to be able to control the electrical characteristics of nanofibers by controlling their composition. The other objective is to be able to grow individual, isolated nanofibers in a controlled way. Such an approach has applications for massively parallel vertical nanofiber devices for nanoelectronics. Our approach for growth of the fibers uses a plasma-enhanced chemical vapor deposition technique using an inductively coupled radio frequency plasma source operated at low pressure (<100 mTorr). The gases used during the growth process include hydrogen and a carbon-containing gas, which is either acetylene or methane. Details of the system and initial growth results can be found in a recently published paper (Caughman et al., *J. Appl. Phys.*, Vol. 83, 2003, p. 1207). Our research to date has focused on understanding of the growth of vertically aligned carbon-based nanofibers and how to change their composition. We have conducted experiments to determine the role of various parameters on the growth results, started the electrical characterization of the nanofibers, and are starting to explore changes to their composition with the addition of boron.

Many parameters influence the growth and structure of vertically aligned carbon nanofibers (VACNFs), including the gas composition, the substrate bias, and the growth temperature. As the gas composition changes from being hydrogen rich to a carbon rich (i.e., by increasing the acetylene flow relative to the hydrogen flow), the structure of the fibers changes from being tall and thin cylinders to broad-based cones. The carbon-rich plasma condition creates excess carbon species that condense on the sides of the fibers to create the cone-like structure. The role of substrate bias is related to ion energy, which controls the physical etching that takes place during VACNF growth. We have discovered that a minimum amount of substrate bias is required to grow fibers. If the ion energies are too low, then a layer of carbon builds up on the surface and VACNF growth stops. We have also discovered that growth temperature is important. If the growth temperature gets too high, then the carbon-containing gas (acetylene of methane) will substantially decompose on the substrate surface and inhibit VACNF growth. There is a balance between growth temperature and gas flow. We have added an optical pyrometer to the system to better control the temperature during growth.

The electrical characterization of the VACNFs has started. We have measured the VACNF conductivity by using a four-point probe technique. We have found that the VACNFs are conducting, with a conductivity similar to graphite at 1 mΩ-cm, which is similar to that measured for VACNFs grown with a DC PECVD technique by Mike Simpson's group at ORNL.

The changes to the fibers as a function of composition are also being explored. For growing boron-containing

VACNFs, we have added dilute diborane to the system (4% in hydrogen). Tests with the mass spectrometer have shown that the plasma is very efficient at breaking up the diborane in the gas-phase, which is probably advantageous for the boron to become bonded in the nanofiber structure (less surface temperature needed to break the chemical bonds because the plasma already did it). High diborane flows have been shown to inhibit nanofiber growth, while low flows do not. The change in nanofiber composition as a function of diborane flow is currently being determined.

There should be numerous benefits for DOE and potential for follow-on funding. The area of nanoscience is of great interest to DOE, and the knowledge that we gain from this work will help us to understand the growth mechanisms of nanofibers. Potential applications of interest include nanoelectronics, field-emission devices, hydrogen storage, and super-hydrophobic materials. We are currently pursuing follow-on funding as part of a white-paper to DARPA.

Development of a New High-Temperature Proton-Electron Mixed Conductor for Hydrogen Separation

E. A. Payzant, R. D. Carneim, S. A. Speakman, and T. R. Armstrong
Metals and Ceramics Division

High-temperature ion transport membranes (proton conductors) are presently limited in availability and performance. Current high-temperature proton conductors (HTPCs) either have low conductivities (e.g., $SrZrO_3$-based materials) or are highly susceptible to chemical attack by contaminants such as sulfur (H_2S) and CO_2 (e.g., $BaCeO_3$-based materials). *The purpose of the proposed research is to develop a practical HTPC, where high conductivity is the primary requirement, based on a novel approach investigating proton conductivity near phase boundaries.* Durability is addressed by avoiding the use of polyvalent lanthanides and transition metals, which bind readily with sulfur—especially under the reducing conditions found in reformate or syngas streams. The perovskites $LaYO_3$ and $SrZrO_3$, and the pyrochlore $La_2Zr_2O_7$, meet the stability requirement and have demonstrated proton conductivity. These binary oxides have low proton conductivities; however, by studying pyrochlore–perovskite binary systems, it was hoped a ternary composition will be produced that meets the primary requirement for a practical HTPC—high conductivity. This novel approach relies on there being at least one phase boundary between the two end-point compositions. It is expected that various properties, including protonic conduction, of each end-point phase can be increased since transport mechanisms are often enhanced near phase boundaries. Rapid synthesis and characterization techniques are used to screen a large number of initial compositions, which was followed by conductivity measurements, structural characterization, and modeling.

X-ray diffraction and dc conductivity measurements were used to survey the functionality of two pyrochlore-perovskite binary systems as high-temperature proton conductors (HTPCs). An efficient HTPC could be employed in a number of electrochemical devices, such as gas separation membranes, fuel cells, or direct chemical conversion stacks. The primary driver for HTPC development is the need for hydrogen separation membranes that can provide an unadulterated hydrogen stream from a reformate feed for petrochemical processing. Equally important, though, are the advantages an efficient HTPC could provide to a future generation of fuel cell technology.

A solid ceramic ion transport membrane has the greatest potential for producing pure hydrogen at high temperatures. Nafion® membranes produced by DuPont are currently the most effective low-temperature proton conductors; however, their maximum operating temperature (~160°C for hybrid membranes) is below the desired operating temperature (500 to 600°C) for petrochemical processes.[1] Microporous membranes operate in this temperature range with high fluxes; however, they are at best 99% selective to hydrogen.[2] Ceramic membranes operate well at high temperatures and can be very selective; however, they are intolerant to H_2S and CO_2 contaminants and their flux is too low for practical application.[2]

Ionic conductivity in ceramics can be enhanced by disorder. Typically, disorder is related to structural defects such as oxygen vacancies or to configurational features such as the rotation and tilting of oxygen polyhedra. However, disorder can also be created by fluctuations in crystal structure. Displacive properties, such as piezoelectricity, are enhanced at compositions near a phase boundary, where little separates one phase from another and localized regions can dynamically fluctuate between different crystal structures.[3] The inherent chaos of these structural fluctuations increases the kinetics of the system. It has recently been shown that transport properties can also be enhanced at a phase boundary, providing a new mechanism for developing fast ion conduction in ceramic oxides.[4]

The crystal structure for pyrochlore, $A_2B_2O_7$, has octahedrally coordinated B-site cations, 8 coordinated A-site cations, and two distinct oxygen sites. The crystal structure of perovskite, ABO_3, also has octahedrally coordinated B-site cations, as well as 12 coordinated A-site cations. The pyrochlore-perovskite binary system was chosen for study because the crystal structures share several features, particularly the BO_6 octohedra. Additionally, small, localized regions of pyrochlore-type ordering were recently observed in perovskite materials.[5]

Therefore, it was anticipated that compositions near the phase boundaries in these systems might exhibit enhanced conductivity due to structural fluctuations. The pyrochlore $La_2Zr_2O_7$ and the perovskites $LaYO_{3-}$ and $SrZrO_3$ were selected for investigation because all have demonstrated proton conduction.[6–9] Furthermore, these systems are stable in the presence of both CO_2 and H_2S. Samples were tested across a full compositional range, thereby including doped-pyrochlore regions, doped-perovskite regions, near-phase boundary regions, and pyrochlore-perovskite heterophase mixtures.

The glycine-nitrate method was used to produce precursor powders for the test materials.[10] Nitrate solutions of the appropriate cations were mixed with glycine fuel and then combusted. The resulting precursor was calcined at 900°C for 1 h. The calcined powders were pressed into pellets and sintered at either 1000°C for 96 h, 1500°C for 2 h, or 1500°C for 15 h. X-ray diffraction (XRD) was used to analyze the precursor, calcined, and sintered powders. Peak positions were determined by profile fitting individual diffraction peaks with pseudo-Voigt functions. The peak positions of standard reference materials were used for internal 2θ calibration of the diffraction data.[11] The calibrated peak positions of the sample were analyzed with a cell refinement algorithm to determine the unit cell lattice parameters.[12]

Discs were sintered at 1500°C, had Pt lead wires attached with silver paint, and then were annealed at 900°C. The electrical conductivities were then measured in air at temperatures between 300 and 900°C using a four-point van der Pauw technique.[13] Electronic measurements were made with two Keithley 6517A electrometers and an Agilent 34970A switch unit. One electrometer simulated a current source, applying voltages (V_{appl}) of ±10, 5, 2.5, 1.25, and 0.675 V and measuring the corresponding current (I_{source}) across two electrodes, while the second electrometer measured the resulting potential (V_{obs}) across the two parallel electrodes. Eight measurements made at different V_{appl} were analyzed for linearity and consistency. The linear portion of the $I_{source}V_{obs}$ curve was then used to determine the resistance. These measurements were repeated for four configurations of the electrodes M, N, O, and P: $I_{MN}V_{OP}$; $I_{NO}V_{PM}$; $I_{OP}V_{MN}$; and $I_{PM}V_{NO}$. The measurements of $I_{MN}V_{OP}$ and $I_{OP}V_{MN}$ were averaged together to produce R_A; likewise, $I_{NO}V_{PM}$ and $I_{PM}V_{NO}$ were averaged together to produce R_B. The resistivity (ρ) was then solved from the equation:

$$\exp\left(-\frac{\pi d}{\rho}R_A\right)+\exp\left(-\frac{\pi d}{\rho}R_B\right)=1 \quad , \tag{1}$$

where d is the thickness of the pellet. These measurements were performed in a Thermolyne F21130-33 tube furnace at different temperatures. The sample temperature was measured with a thermocouple that was independent from the one used to operate the furnace. The resulting temperature and conductivity data were used in an Arrhenius analysis to determine the activation energy (E_A) and pre-exponential geometric factor (σ_o) according to the equation:

$$\sigma_{ion}=\frac{\sigma_o}{T}\exp\left(-\frac{E_A}{kT}\right) \quad . \tag{2}$$

Activation energies and geometric factors (E_A and σ_o) at 600°C were determined by linear regression analysis of the observed conductivity data. Figure 1 shows the electrical conductivity for the various compositions in air at 600°C, while Fig. 2 shows the variation of E_A and σ_o with composition.

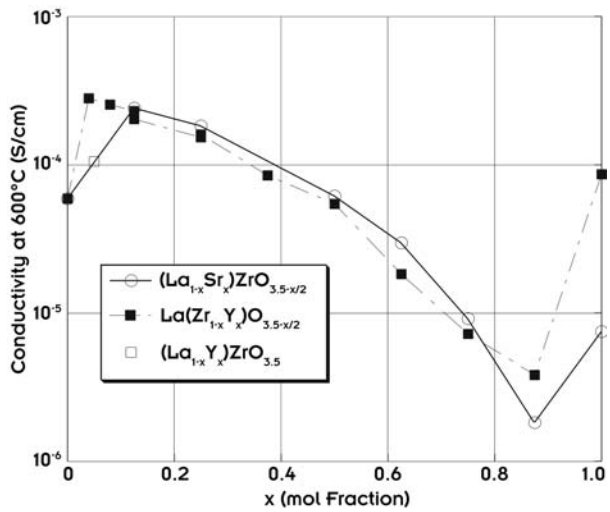

Fig. 1. The electrical conductivity at 600°C in air.

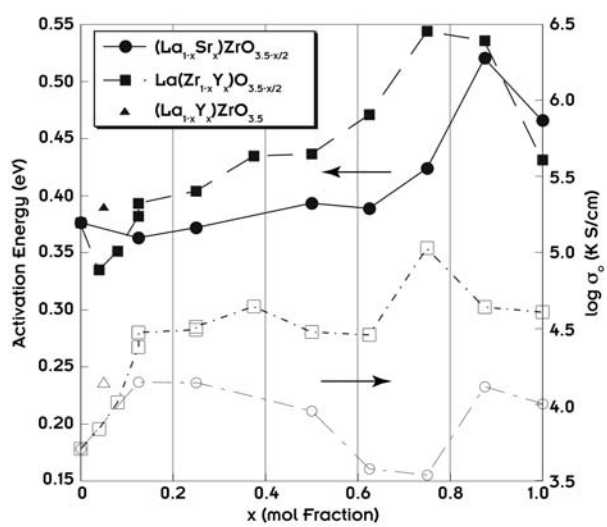

Fig. 2. The activation energies (solid data points) and pre-exponential factors (hollow data points) for electrical conductivity at 600°C in air.

The conductivities of both $(La_{1-x}Sr_x)ZrO_{3.5-x/2}$ and $La(Zr_{1-x}Y_x)O_{3.5-x/2}$ varied similarly with composition. Low levels of doping in $La_2Zr_2O_7$, whether by the substitution of Sr for La or the substitution of Y for Zr, produced a modest increase in the high-temperature conductivity. Likewise, both $(La_{1-x}Sr_x)ZrO_{3.5-x/2}$ and $La(Zr_{1-x}Y_x)O_{3.5-x/2}$ exhibited a depression in conductivity at low levels of doping in the perovskite phase, whether La-doped $SrZrO_3$ or Zr-doped $LaYO_3$. The conductivities of compositions $0.125 < x < 0.875$ varied almost linearly and empirically appeared to be a mixing function of the conductivity at $x = 0.125$ and $x = 0.875$.

Though the conductivities of $(La_{1-x}Sr_x)ZrO_{3.5-x/2}$ and $La(Zr_{1-x}Y_x)O_{3.5-x/2}$ behaved similarly, their dopant solubilities did not. In $(La_{1-x}Sr_x)ZrO_{3.5-x/2}$, a phase pure product was only formed for $x = 0$ and 1. All other compositions produced heterophase mixtures of perovskite and pyrochlore phases. The lattice parameters of $(La_{1-x}Sr_x)ZrO_{3.5-x/2}$ did not vary much with composition for either the pyrochlore or perovskite phases, confirming that little or no doping occurred.

The $La(Zr_{1-x}Y_x)O_{3.5-x/2}$ phase diagram was more complicated than that of $(La_{1-x}Sr_x)ZrO_{3.5-x/2}$, despite the similarities in their conductivities. A pyrochlore phase was observed for $0 \le x \le 0.25$ in $La(Zr_{1-x}Y_x)O_{3.5-x/2}$, though a small amount of La_2O_3 impurity was observed at $x = 0.125$ and 0.19 and an unidentified phase was observed at $x = 0.25$. Examination of lattice parameters, shown in Fig. 3, revealed that Y did not substitute strictly for Zr as anticipated but rather substituted for both Zr and La at higher doping levels. According to Vegard's Law, if the substitution of Y into $La_2Zr_2O_7$ followed a consistent pattern, then the variation of the lattice parameter with composition would be linear. The lattice parameters for $0 \le x \le 0.25$ were not co-linear but rather demonstrated a discontinuity between $x = 0.08$ and 0.125. In Fig. 3, the lattice parameter of $(La_{0.95}Y_{0.05})ZrO_{3.5}$ is also shown; it was significantly smaller than that of $La_2Zr_2O_7$. These data support the hypothesis that Y substituted on both the A and B sites. The substitution of La by the smaller Y cation on the A site produced a smaller unit cell in $(La_{0.95}Y_{0.05})ZrO_{3.5}$, while the substitution of Zr by the larger Y cation on the B site produced a larger unit cell in $La(Zr_{0.96}Y_{0.04})O_{3.48}$. For $0.125 \le x \le 0.25$, Y substituted onto both the A and B sites, producing a mixed effect on the size of the unit cell. This hypothesis was further supported by the observation of La_2O_3 in the XRD patterns of $x = 0.125$ and 0.19. Since the composition was formulated for pure B site substitution, the occupancy of Y on the A site produced excess La_2O_3. The lack of La_2O_3 in the X-ray diffraction (XRD) pattern of $x = 0.25$ deviated from this hypothesis; however, there was a second (presently unidentified) phase observed. It was suggested that this phase was a La-rich phase that formed instead of La_2O_3, though this was not proven. The exact composition at which Y began to substitute onto the A site has not yet been clearly identified. The lattice parameter of $x = 0.08$ lies below a line defined by the lattice parameters at $x = 0$ and $x = 0.04$, suggesting that the lattice parameter at $x = 0.08$ was not as large as it would be if Y substituted only for Zr on the B site and therefore that a small amount of A site substitution may have occurred at $x = 0.08$.

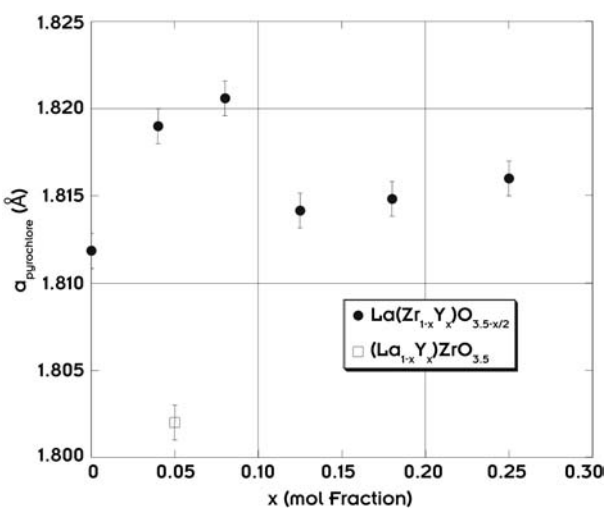

Fig. 3. The variation of the lattice parameter of the pyrochlore phase $La(Zr_{1-x}Y_x)O_{3.5-x/2}$.

As a consequence of the A-site substitution by Y, the electrical conductivity did not increase above its level at $x = 0.04$ and 0.08. The substitution of La with Y did not produce oxygen vacancies and therefore had little effect on the conductivity. The substitution of Y for Zr in $La_2Zr_2O_7$ at 0.04 and 0.08 mole fraction increased σ_o and decreased E_A, thereby increasing the overall conductivity; however, the Y-doping at greater levels of 0.125, 0.19, and 0.25 mole fraction consisted mostly of La substitution and consequently increased E_A, leading to a decrease in conductivity.

The conductivity behavior of $La(Zr_{1-x}Y_x)O_{3.5-x/2}$ at $x \ge 0.875$ paralleled that of $(La_{1-x}Sr_x)ZrO_{3.5-x/2}$, but the phase composition was markedly different, showing a dependence on thermal history. Samples sintered at 1000°C were an orthorhombic polymorph of $LaYO_3$.[14] Pellets sintered at 1500°C had different phases on the surface and within the interior of the pellet. The surface phase was a metastable cubic polymorph of $LaYO_3$,[15] while the interior of the pellet was a presently unindexed polymorph of $LaYO_3$, best described with an orthorhombic unit cell, similar to the orthorhombic polymorph formed at 1000°C but with an a/b ratio closer to 1 (i.e., more nearly tetragonal) and a different symmetry. A definitive indexing was not achieved. In order to test the effect of these polymorphs on conductivity, two pellets of $La(Zr_{0.125}Y_{0.875})O_{3.0625}$ were sintered at 1500°C. One was

ground to remove the surface layer, then electroded; the other was not ground and was electroded. Conductivity data empirically indicated that the surface cubic phase surface layer of $LaYO_3$ acted as a barrier to conduction.

Doping of $La_2Zr_2O_7$, $LaYO_3$, and $SrZrO_3$ was shown to affect the electrical conductivity. Substitutional doping of Sr for La and Y for Zr in $La_2Zr_2O_7$ increased the conductivity, with the greatest gains achieved by 4 and 8 mol % substitution of Y for Zr. Yttrium was more soluble in $La_2Zr_2O_7$ than Sr; however, its effectiveness as a dopant was hindered by its tendency to substitute for both A and B site cations at higher doping levels. Enhancement of conductivity due to phase boundaries has not yet been demonstrated, primarily owing to the lack of miscibility between the systems studied to date, and perhaps also influenced by the occupancy of Y on both A- and B-sites in $La_2Zr_2O_7$, which precludes a single, well-defined phase boundary between pyrochlore and pyrochlore-perovskite. The complex system of polymorphs of $LaYO_3$-based perovskites may also have hindered the dynamics at the boundary between pyrochlore-perovskite and perovskite.

Computer simulations of empirical potential models are currently being used to identify pyrochlore-perovskite binary systems with greater miscibility and therefore a greater chance of producing enhancement of the conductivity near the phase boundaries. Conductivity data is scheduled to be collected on this system in a hydrogen atmosphere in order to separate the proton contribution to the overall conductivity. Neutron powder diffraction data will be collected in early October 2003 for Rietveld refinement of these systems to facilitate more exact identification of site occupancies in these systems and a greater understanding of the relationship between structure and conductivity. Finally, additional compositions with Ce, Sc, and Ga dopants are being synthesized in an effort to improve the overall conductivity.

References

[1]G. Alberti and M. Casciola, "Solid State Protonic Conductors, Present Main Applications and Future Prospects," *Solid State Ionics* ***145***(1–4), 3–16 (2001).

[2]Y. S. Lin, "Microporous and Dense Inorganic Membranes: Current Status and Prospective," *Separation and Purification Technology* **25**(1–3), 39–55 (2001).

[3]R. Newnham, "Phase Transformations in Smart Materials," *Acta Cryst*. **A54**(6.1), 729–37 (1998).

[4]H. Yamamura, H. Nishino, K. Kakinuma, and K. Nomura, "Electrical Conductivity Anomaly around Fluorite-Pyrochlore Phase Boundary," *Solid State Ionics* **158**(3–4), 359–65 (2003).

[5]J. T. S. Irvine, "High Temperature Fuel Cell Materials-Structure at Ion's Length," presented at Materials for Energy Production and Storage Conference, Rutherford Appleton Laboratory, March 6–7, 2003.

[6]J. A. Labrincha, J. R. Frade, and F. M. B. Marques, "Protonic Conduction in $La_2Zr_2O_7$-based Pyrochlore Materials," *Solid State Ionics* **99**(1–2), 33–40 (1997).

[7]E. Ruiz-Trejo and J. A. Kilner, "Oxygen Diffusion and Proton Conduction in $La_{1-x}Sr_xYO_{3-d}$," *Solid State Ionics* **97**(1–4), 529–34 (1997).

[8]J. A. Labrincha, F. M. B. Marques, and J. R. Frade, "Protonic and Oxygen-Ion Conduction in $SrZrO_3$-based Materials," *J. of Materials Science* **30**(11), 2785–92 (1995).

[9]T. Schober, F. Krug, and W. Schilling, "Criteria for the Application of High Temperature Proton Conductors in SOFCs," *Solid State Ionics* **97**(1–4), 369–73 (1997).

[10]L. A. Chick, L. R. Pederson, G. D. Maupin, J. L. Bates, L. E. Thomas, and G. J. Exarhos, "Glycine-Nitrate Combustion Synthesis of Oxide Ceramic Powders," *Materials Letters* **10**(1–2), 6–12 (1990).

[11]R. Jenkins and R. L. Snyder, *Introduction to X-Ray Powder Diffractometry*, pp. 281–5, John Wiley & Sons, Inc., New York, 1996. Materials Data, Inc., *Jade v. 6.5.5*, Livermore, California, 2003.

[12]L. J. van der Pauw, "A Method of Measuring the Resistivity and Hall Coefficient on Lamellae of Arbitrary Shape," *Philips Technical Review* **20**(8), 220–4 (1958).

[13]J. Coutures and M. Foex, "Etude à haute température du diagramme d'equilibre du système formé par le sesquioxyde de lanthane avec le sesquioxyde d'yttrium, " *J. Solid State Chem.* **11**(4), 294–300 (1974).

[14]O. Yamaguchi, H. Kawabata, H. Hashimoto, and K. Shimizu, "New Modification of $LaYO_3$," *J. Am. Ceram. Soc.* **70**(6), C131–2 (1987).

Selective Area Chemical Vapor Deposition of Carbon Nanotube Films Using Seeded Molecular Beams

G. Eres
Condensed Matter Sciences Division

Because carbon nanotubes (CNTs) are not a stable form of carbon, synthetic routes for formation of CNTs must be kinetically controlled. The objective of this project is to explore beams of small carbon-containing molecules for catalytic growth of CNTs. The molecular beam environment allows reaction control at the single collision level, revealing the molecular parameters that influence the catalytically induced conversion of hydrocarbons into CNTs. The key benefits of this approach include reducing the growth temperature of CNTs, controlling the structure (single wall vs multiwall) of CNTs, increasing the yield, and circumventing formation of undesirable side products such as nanoparticles and amorphous carbon.

The main obstacle to widespread practical application of CNTs is the lack of controllable synthesis methods. Currently single-wall CNT (SW-CNT) synthesis is performed either by evaporation and spontaneous condensation of carbon or by high-temperature chemical vapor deposition of hydrocarbons using transition metal catalysts. The extreme reaction conditions in these growth techniques induce a large number of secondary reactions that, in addition to SW-CNTs, produce numerous undesirable side products such as encapsulated nanoparticles and amorphous carbon. These side products interfere with applications, and must be removed before the CNTs can be used.

The molecular beams are generated by mixing small amounts of hydrocarbon source gases (2%) with an inert carrier gas such as He. The beam of carbon molecules is directed at a heated substrate containing a thin film of transition metal catalyst. Upon collision with the substrate, the carbon molecules either stick to the surface or bounce off unchanged and are pumped away. For a fixed catalyst composition, the outcome of the collision depends on the nature of the carbon-containing molecule, the incident velocity of the molecule, the incident angle of the molecule, and the substrate temperature. Each of these reaction parameters can be independently controlled to form the desired reaction products, namely, pure SW-CNTs. The following results have been achieved during the first half of the funding period in this project.

The key accomplishment of this project is the growth of SW-CNTs from molecular beams. There are no previous reports in the literature of SW-CNT growth from molecular beams. The substrate temperature for SW-CNT growth was in the range from 530°C to 680°C. Interestingly, CNT growth ceases above 680°C, suggesting that the mechanism for CNT growth is governed by a surface-limited reaction. Compare these growth temperatures with typical CNT growth temperatures by hot-wall CVD of 900°C or higher.

The molecular structure was found to play an important role in determining the CNT yield from hydrocarbons. No SW-CNT growth was observed from CH_4, and only a small amount of SW-CNTs was found with C_2H_4. The best precursor for SW-CNT growth was C_2H_2. The order CH_4, C_2H_4, C_2H_2 represents a chain of stable intermediates in carbon formation by thermal decomposition of methane. This trend implies that the molecule that is the closest stable intermediate to carbon formation should be chosen to obtain the highest CNT yield.

Several transition metal catalyst were explored in the form of thin films, and chemically synthesized catalyst nanoparticles, deposited on various substrates including Si, sapphire, and quartz. The most effective catalyst was Fe, followed by Co. Surprisingly no CNT growth was observed with Ni. The composition and the thickness of the catalyst films also affected SW-CNT growth. No CNT growth was observed using chemically synthesized nanoparticles of Fe, Co, FeMo, and FePt.

In the second half of this project, work will be focused on the chemical reaction dynamics of the most efficient catalyst-carbon source molecule system. The goal is to use the molecular reaction parameters to tailor the properties of as-grown SW-CNTs in application-relevant configurations.

High-T_c Silicon-Compatible Ferromagnetic Semiconductors

H. H. Weitering, J. Shen, and Z. Zhang
Condensed Matter Sciences Division

Semiconductor "spintronics" holds great promise for novel, faster devices that consume much less power than conventional electronics and that may even facilitate quantum bit or "qubit" operations for quantum computing. The control of the electron spin in semiconductor devices is still at a conceptual stage, awaiting the science and engineering breakthroughs to create new materials and technologies. The objective of this project is to create silicon-compatible semiconductor materials with high ferromagnetic ordering temperatures which could serve as the spin injector or spin detector in silicon-based spintronic devices.

The revolution of spin-based electronics ("spintronics") in materials physics is likely to impact our lives in ways reminiscent of the early days of the transistor and microelectronics industry. Unlike current microelectronic devices, spintronic devices utilize both carrier spin and charge to carry or store information. Spin is a purely quantum phenomenon which lends itself elegantly to the logic of "ones" and "zeroes." One example of a spintronic device is the "spin valve," a layered structure of magnetic and nonmagnetic metal films, which is now widely used in read heads for magnetic hard disk drives. The discovery of high-temperature ferromagnetism in diluted magnetic semiconductors in the late 1990s has defined a radically new avenue in spintronics research.[1,2] If spintronic devices can be made from semiconductors (i.e., if semiconductors could be made magnetic), then in principle we could build spin amplifiers and integrate electronic, opto-electronic, and magneto-electronic functionality on a single device. We may even think of injecting spin-polarized currents into semiconductors and controlling the spin state of the charge carriers, which may allow quantum bit operations for quantum computing.

There are two ways to realize spin injection. One of these is to fabricate a ferromagnetic-metal/semiconductor (MS) heterostructure; the other is to use a dilute magnetic semiconductor (DMS) as the spin aligner. The former method is hampered by chemical intermixing or lattice mismatch at the MS interface, which usually results in significant loss of spin polarization. The large "conductivity mismatch" between the metal and semiconductor furthermore limits the spin injection efficiency for "transparent" MS contacts. Low Curie temperatures (T_c) limit the latter method using a DMS. The objective of this program is to create semiconductors with ferromagnetic ordering temperatures (i.e., Curie temperatures) approaching room temperature so as to create atomically abrupt interfaces between a high-T_c DMS and a nonmagnetic semiconductor for spin-injection purposes. These novel materials are grown using molecular beam epitaxy, an advanced growth technique that allows researchers to create artificially structured materials that cannot be grown under thermodynamic equilibrium conditions. The synthesis efforts are guided by theory efforts, aimed at predicting the proper growth conditions and magnetic properties.

We have succeeded in making germanium semiconductor ferromagnetic by doping it with a few percent of manganese (Mn). The Mn atoms are distributed randomly in the crystal lattice, and the highest Curie temperature that can be achieved by random doping is about 110 K. Although similar results had been reported in 2002 by researchers at the Naval Research Laboratory in Washington, D.C.,[3] we have firmly established the parameters for optimum growth and significantly increased the ferromagnetic ordering temperature by about 40 K through "digital doping" (Fig. 1). In digital doping experiments, Mn atoms are located in two-dimensional sheets. Parallel theoretical studies by Fishman and collaborators, using dynamical mean field theory, have indicated that these materials are so-called "frustrated" magnets and that the ferromagnetic transition temperature can be substantially increased by alleviating magnetic frustration. In a digitally doped heterostructure, magnetic frustration can be removed from each plane of Mn atoms when the Mn magnetic moments are aligned normal to the plane. The consistency between theory and experiment show that it is indeed possible to boost the magnetic ordering temperature in artificially structured materials, as we originally envisioned.

Spintronics is a major research area for the DOE and other federal agencies. Within the first year, this project produced a novel heterostructure for spin injection in a

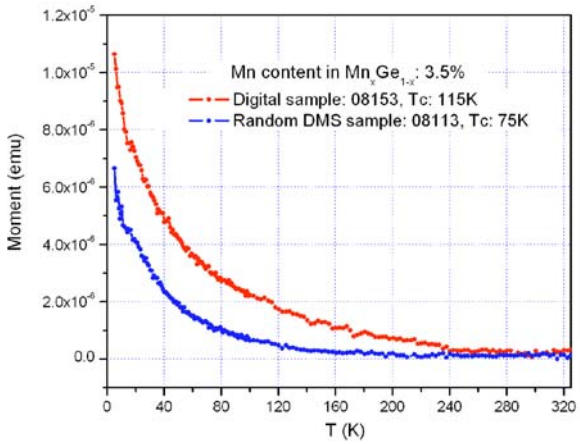

Fig. 1. Magnetization of a "random" and a "digital" manganese-germanium heterostructure as a function of temperature. Digital doping significantly enhances ferromagnetism.

silicon compatible geometry and produced a powerful strategy toward enhancing the ferromagnetic ordering temperature in a dilute magnetic semiconductor. These accomplishments represent major contributions toward solving the bottleneck issues for spintronics research and technology.

References

[1]S. A. Wolf, D. D. Awschalom, R. A. Buhrman, J. M. Daughton, S. von Molnár, M. L. Roukes, A. Y. Chtchelkanova, and D. M. Treger, "Spintronics, A Spin-Based Electronics Vision for the Future," *Science* **294**, 1488 (2001).

[2]T. Dietl, "Ferromagnetic Semiconductors," *Semicond. Sci. Technol*. **17**, 377 (2002)

[3]Y. D. Park, A. T. Hanbicki, S. C. Erwin, C. S. Hellberg, J. M. Sullivan, J. E. Mattson, T. F. Ambrose, A. Wilson, G. Spanos, and B. T. Jonker, "A Group-IV Ferromagnetic Semiconductor: Mn_xGe_{1-x}," *Science* **295**, 651 (2002).

An Innovative Technique for Bimaterial Interface Toughness Research

J. A. Wang,[1] K. C. Liu,[2] I. G. Wright,[2] and L. R. Xu[3]
[1]*Nuclear Science and Technology Division*
[2]*Metals and Ceramics Division*
[3]*Vanderbilt University*

In general, the weakest link in bimaterials occurs at the interface between dissimilar materials, such as the interface between a thin film and its substrate. In order to make multilayered electronic devices or structural composites with a long-term reliability, the fracture behavior of these interfaces must be known. Unfortunately, none of the state-of-the-art testing methods for evaluating interface fracture toughness fully conform to fracture mechanics theory, as is evident in existing data that show severe scatter and procedure dependence in thin-film evaluation methods. This project addresses the problems associated with this deficiency and offers an innovative testing procedure for determination of interface fracture toughness applicable to thin-coating materials in general.

The drive toward increased performance, efficiency, and reduced environmental pollution in heat engines, energy conversion processes, and many chemical processes involves operation of equipment at higher temperatures, often in increasingly corrosive environments. All materials of construction require environmental protection, and in high-temperature environments, the ability of the protective barrier to remain adherent to the surfaces is critical. As a result, measurement of the toughness of the substrate-barrier interface addressed in this project is expected to enhance the ability to improve the performance of many of the components needed in, for example, the DOE's Vision 21 and distributed generation programs, as well as in DOD programs to improve liners for combustors and thermal barrier coatings for gas turbine engines, and to develop better thermal protection systems for space vehicles.

An innovative technology for measuring interface toughness will be demonstrated for oxide scales formed on high-temperature alloys. This new approach includes the development of analytical and experimental procedures and associated bimaterial fracture mechanics theory for evaluating interface fracture toughness. The expected outcomes are (1) improved life prediction capability for high-temperature environmental and thermal barrier coatings, (2) understanding of the mechanism of the interface crack initiation, and (3) determination of unambiguous values for interface fracture toughness. This innovative technique is expected to greatly assist the development of coating materials with improved protective capabilities and provide a reliable method for use in assessing material performance.

In the Phase I of the proposed project, the following progress was made as scheduled:

- Upgraded biaxial test machine with a new load cell capable of high resolution required for torsional testing on thin film materials.
- Selected a Ni-based super alloy (MA956) currently used in high-temperature heat exchangers as the base material on which a thin coating will be formed by oxidation. Two types of notch configurations, a V-shape and a U-shape with different aspect ratios, were used in the new spiral notch torsion test (SNTT) specimens. The specimens are currently being fabricated at a local machine shop.
- To enhance the latitude of this project, a collaboration was discussed with Dr. Matt Ferber of the ceramic structure group at the High Temperature Materials Laboratory (HTML) for using his thermal-barrier-coating (TBC) material in the proposed study. The specimen design appropriate for this material was also completed.
- Developed a fatigue precrack procedure, which utilizes underpeak detector to detect and control fatigue crack growth.
- Developed the finite element models for the SNTT specimens with specified notch configurations and the boundary conditions.

The great technical challenges are expected to be met both in developing experimental procedures and testing apparatus, and theoretical and analytical evaluation of interface toughness for the proposed configurations, which will be carried out in the Phase II research in FY 2004.

The development of this innovative testing procedure will support innovation in the development and use of materials and coatings by providing reliable methods for industry to use in assessing their performance and provide industry with the means to develop and use better (more advanced) materials and coatings through a better understanding of how they behave in practical situations. Knowledge of how the toughness of coating-substrate interfaces is influenced by alloy and coating parameters will greatly aid improved environmental/thermal barrier design.

Nanoporous Inorganic Membranes for High Selectivity Hydrogen Separations

L. K. Mansur and B. L. Bischoff
Metals and Ceramics Division

The United States is committed to a future hydrogen economy. Hydrogen is not generally available as an elemental resource. It can be dissociated from compounds, such as from hydrocarbons or water, by high-temperature chemical reactions. Subsequent to dissociation, effective recovery of hydrogen from gas mixtures becomes a central issue. We are addressing this issue by research on the nanoscience of inorganic gas separation membranes. Pore sizes in commercially available membranes range from about 4 nm to many micrometers. Knudsen diffusion, surface transport, and other reasonably well-understood permeation processes provide limited gas selectivity in such commercial membranes. Recently, we have fabricated experimental inorganic membranes with pore sizes of 1 nm or less. Proof-of-principle experiments are now being carried out on these membranes with the goal of demonstrating exceptionally high selectivity for hydrogen with respect to a number of other gases including a hydrocarbon and carbon dioxide. Guided by theoretical models, we are analyzing these data for evidence of the dominant separation mechanisms in operation and, in particular, for thermally activated atomic-level separation mechanisms.

Approximately 40 nanoporous membranes have been fabricated and characterized over the past 2 years in earlier research. Much of the permeation work to characterize the selectivity of these membranes employed helium and sulfur hexafluoride (SF_6) up to temperatures of 275°C. This base of historical data was examined at the outset of the present research effort.

Since hydrogen separation from hydrocarbon mixtures is the focus of our research, H_2 was added to the membrane evaluation protocol and propane (C_3H_8) was chosen to replace SF_6. A modification to the test system was completed for these flammable gases. The required safety documentation was completed and approved. The system is now fully operational for analysis of the permeation of individual gases, including H_2, He, CO_2, and C_3H_8 up to 275°C. Measurements with SF_6 will also be carried out for comparison with earlier work. In order to help determine the fundamental operating mechanisms of gas separation, it is essential that data be obtained over a wider range of temperatures. Therefore, more recently, a second system has been modified to measure the permeation of individual gases up to approximately 400°C. In addition, this second system gives us the capability to measure the separation of hydrogen from mixtures of gases. During the past month, permeation measurements were initiated. Nanoporous membranes are currently being evaluated with the series of gases mentioned. In several cases the preliminary data show selectivities higher than that for Knudsen diffusion, indicating that the membrane pore size is indeed in the desired nanometer-size regime.

In order to most effectively analyze the experimental data being accumulated, the dominant operating mechanisms of membrane transport need to be known. To this end we have distilled parametric dependencies of key mechanisms of gas transport into simple and readily applicable expressions. Key parameters include temperature T, pressure P, molecular mass m, kinetic molecular diameter d_m, pore diameter d_p, molecular collision mean free path λ, and several thermal activation energies. The latter are H_a, the heat of gas adsorption, E_s, the activation energy for surface diffusion, and E_d, the activation energy for nanopore diffusion.

The most important characteristic of membranes that dictates the dominant transport mechanism is the pore diameter or, more precisely, the ratio of the pore diameter to two important physical characteristics of the gas, λ and d_m. Most gases of interest have kinetic diameters between one-fourth and two-thirds of a nanometer. Generally, for pore diameters >2 nm, the important permeation mechanisms in operation are Knudsen diffusion and surface transport, together with molecular diffusion and viscous flow (Poiseuille or laminar flow) at larger pore diameters. For pore diameters of about 1 nm and smaller, other mechanisms, which are covered by the term "nanopore diffusion," come into operation. Several mechanisms of gas transport through a membrane are summarized in Table 1. Expressions for selectivity and permeance also are given in the table for those cases where the dependencies on important variables can be expressed in simple form without extensive qualifying statements or limiting conditions.

Table 1. Characteristic expressions for key membrane gas-transport mechanisms

Mechanism	Pore Diameter	Selectivity	Permeance
Viscous Flow	$\lambda < d_p$	None	$d_p^2\ P\ T^{-1}$
Molecular Diffusion	$\lambda < d_p$	None	
Knudsen diffusion	$\lambda > d_p$	$m^{-1/2}$	$m^{-1/2}\ d_p\ T^{-1/2}$
Surface Transport	All d_p	Variable	$d_p^{-1}\ P \exp[(H_a - E_s)/RT]$
Capillary Condensation	$f(P)$	Variable	
Nanopore Diffusion	$3\ d_m > d_p$	Highest	$m^{-1/2}\ d_p\ T^{-1/2} \exp[-E_d/RT]$

This research project is expected to help DOE to accomplish its goals set forth in the "National Hydrogen Energy Roadmap" released by Secretary of Energy Spencer Abraham on November 12, 2002. The work can benefit programs within the Office of Fossil Energy, including the separation of hydrogen during syngas production and the Oil Processing Program, where hydrogen is used to upgrade low-grade heavy petroleum in a refinery. Government agencies, such as NASA, that heavily utilize hydrogen as an energy source can benefit from the capability to separate hydrogen more efficiently.

High-Aspect-Ratio Carbon Nanofiber Probes for Scanning Probe Microscopy

M. L. Simpson,[1] M. A. Guillorn,[1] C. Rouleau,[2] D. Hensley,[1,2]
R. J. Kasica,[1] M. J. Doktycz,[3] and A. V. Melechko[1,4]
[1]*Engineering Science and Technology Division*
[2]*Condensed Matter Sciences Division*
[3]*Life Sciences Division*
[4]*University of Tennessee*

The objective of this project is to develop the first technique for the synthesis of high-resolution, high-aspect-ratio scanning-probe-microscope (SPM) tips that can be implemented in a large-scale fabrication process. This technique will be based on the ORNL-developed vertically aligned carbon nanofibers (VACNF) technology. While other methods currently exist for the production of this type of probe tip, the use of the VACNF will surpass these techniques since VACNFs can be synthesized completely deterministically in a wafer-scale fabrication process. This allows for thousands of identical tips to be fabricated simultaneously in precise locations with total control over their morphology.

Scanning probe microscopy (SPM) has become an indispensable tool for the analysis of surfaces and the exploration of general substrate morphology at the nanoscale and microscale. Moreover, SPM techniques have been used to investigate a wide variety of material properties beyond substrate topography. The range of applications spans a vast array of scientific disciplines ranging from solid state physics to biology, environmental science to polymer engineering. The currently used methods for producing high-resolution, high-aspect-ratio tips for SPM applications are based on processes serial in nature; that is, only a single tip can be fabricated at a time. The goal of this project is to integrate synthesis of vertically aligned carbon nanofibers (VACNFs) with standard cantilever fabrication processes and to characterize the high-aspect-ratio VACNF SPM tips obtained in such method.

We have demonstrated that VACNFs can be synthesized in a completely deterministic manner using a catalytic dc, plasma-enhanced, chemical vapor deposition process. Features such as the location, length, tip diameter, shape, and chemical composition of VACNFs can be precisely controlled during the synthesis process. Functional microfabricated device structures have been fabricated that exploit both the electrical and mechanical properties of single and multiple VACNF. These structures have been fabricated on a variety of substrates including whole 10-cm-diameter Si, Si-on-insulator (SOI) and quartz wafers. This material meets the required specifications for high-aspect-ratio SPM tips. In addition, it offers a number of other features that may allow it to surpass all other materials presently used in SPM tip manufacturing.

The fabrication process for microcantilevers with VACNF tips have been developed during FY 2003. Individual processing steps compatible with handling microsctructures with high-aspect-ratio features such as VACNFs have been developed and tested. The first batch of cantilevers with VACNF tips has been obtained, thus proving the feasibility of the idea. Figure 1 shows an SEM image of a finished device. The sharpness of the VACNF tips has been improved via changes in the catalyst preparation process. The diameter of the nanofiber coincides with the diameter of the catalyst particle. We have found the techniques to prepare smaller nanoparticles that can be prepared using standard photolithography, thus making the complete fabrication an inexpensive and high-throughput method.

The devices obtained after optimization of all processing steps will be characterized, and their performance will be compared to currently available atomic force microscope tips in application areas that are critical to DOE and NIH. Micro- and nano-fabricated structures and complex biological systems, two major research thrust areas at ORNL, possess a varied surface topography that is often best characterized by SPM techniques. However, they can only be imaged accurately with high-resolution high-aspect-ratio tips. We will explore the application of the VACNF probe tips in these two target areas as they show significant promise to benefit programs at ORNL.

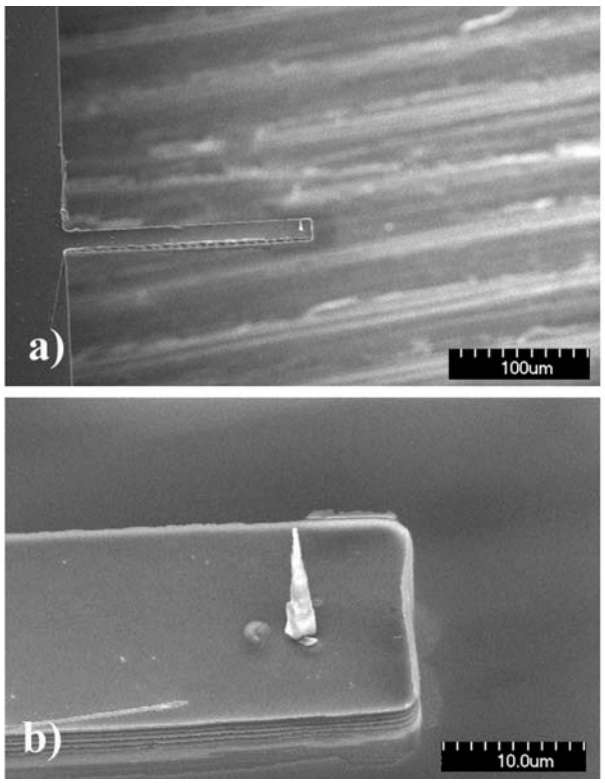

Fig. 1. Scanning electron micrographs of a cantilever with a VACNF tips at 45° viewing angle at two different magnifications: (a) 300× and (b) 3000×.

In Situ Studies of Hydrogen Storage Materials Using Neutron Scattering

C. J. Rawn,[1,2] J. Y. Howe,[1] B. C. Chakoumakos,[3] J. L. Robertson,[3] and F. C. Montgomery[1]
[1]*Metals and Ceramics Division, Oak Ridge National Laboratory*
[2]*Materials Science and Engineering Department, University of Tennessee*
[3]*Condensed Matter Sciences Division, Oak Ridge National Laboratory*

This project concentrates on using in situ neutron diffraction studies to answer structural and thermodynamic issues about the role of hydrogen in hydrogen containing compounds. The first tasks underway are collaborating with personnel from the neutron scattering facility at Chalk River to collect neutron diffraction data at ambient conditions on candidate hydrogen storage materials and to design and construct a new pressure cell for use at different temperature and pressure ranges of interest for the investigation of suitable hydrogen storage materials. Future research includes proof-of-principle experiments using the new pressure cell to demonstrate its utility for implementation of neutron scattering experiments on hydrogen-containing compounds.

Progress Report

To obtain a pressure cell for use at different temperature/pressure ranges of interest for the investigation of suitable hydrogen storage materials. To verify the efficacy of the cell by studying $NaAlD_4$ and demonstrate that we can generate details surrounding the role of H atoms in the atomic structure.

To collect neutron powder diffraction data on the candidate hydrogen storage materials $NaAlD_4$ doped with the addition of $TiCl_3$ as a catalyst. With high-quality neutron powder diffraction data we can use the Rietveld method to determine the positions of Ti in the crystal structure. Additional in situ experiments have been proposed to observe hydrogen absorption and desorption under service conditions of hydrogen storage materials. From these experiments we hope to understand the path that the hydrogen atoms take during absorption and desorption and to evaluate a high-temperature/high-pressure cell, designed by the group at Chalk River, for possible procurement and use at the High Flux Isotope Reactor.

Our two-phase proposal to obtain beamtime on the powder diffractometer at the Chalk River neutron scattering facility has been review and approved, and we are hoping to start data collection in early March. The first experiments we wish to conduct are at ambient temperature and ambient pressure on $NaAlD_4$ with and without the addition of $TiCl_3$ as a catalyst. There are several explanations in the literature for where the Ti must be located within in the crystal structure; however, to date this has not been shown experimentally using neutron scattering techniques. Our intent is to collect a high-quality neutron powder diffraction pattern and examine the data using the Rietveld method to determine the sites occupied by Ti in the $NaAlD_4$ unit cell. A third data set is to be collected on $NaAlD_4$ + $TiCl_3$ desorbed to Na_3AlD_6 + products. We are collaborating with Joachim Schneibel (Metals and Ceramics Division) to synthesize $NaAlD_4$ with $TiCl_3$ from as-received $NaAlH_4$ by desorbing the material and recharging it with D_2 gas.

One of the main goals of this proposal is obtain a high-pressure/high-temperature cell to study hydrogen storage materials with in situ neutron powder diffraction techniques. To this end we are collaborating with Lachlan M.D. Cranswich, a Research Council Officer from the Neutron Program for Materials Research at Chalk River Laboratories (Chalk River, Ontario, Canada). In July we learned from Mr. Cranswick that the Chalk River group was in the first stages of designing such a cell, and in October Mr. Cranswich visited ORNL and discussed the early stages of a high-pressure/high-temperature cell design. Figure 1 shows the mass flow control layout designed to minimize the amount of tubing. The design of this pressure cell is such that it will work in conjunction with a commercial Cryofurnace, which we currently have available at the High Flux Isotope Reactor (HFIR), for changing the temperature. For the current cell design, the highest obtainable pressure would be 10 bar, and we have proposed modifications to the design to obtain pressures of 50 bar. For this increased pressure range, several factors such as the choice of container material and the addition of an external gas booster are being considered. We have received two of mock-up sample holders that are the sizes and geometry used on the powder diffraction beamline at the Chalk River facilities. These cells contain porous metal filters that will allow the gas into the sample holders

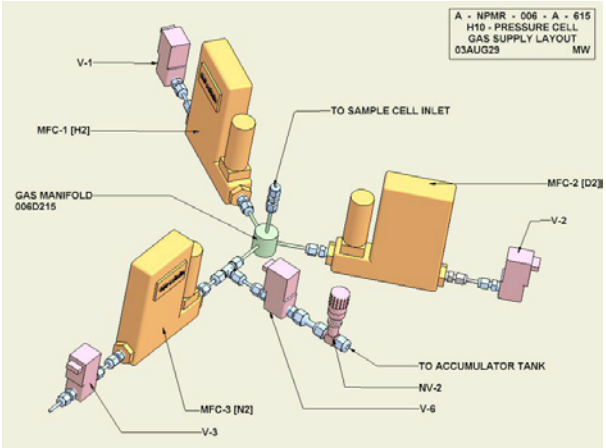

Fig. 1. The Chalk River design for the mass flow controllers for the 10 bar hydrogen pressure cell. The design attempts to minimize the amount of tubing used.

without blowing the powder samples out. These cells are important to our understanding of how much powder will be needed per experiment.

This research will result in expertise in the characterization of hydrogen-storage material systems at the atomic level and position ORNL to compete for future funding from the Hydrogen, Fuel Cells, and Infrastructure Technology Program and other areas where hydrogen fuel is the focus.

Alanates for High-Capacity Hydrogen Storage

J. H. Schneibel,[1] D. S. Easton,[2] S. Babu,[1] and S. A. Speakman[1]
[1]*Metals and Ceramics Division*
[2]*Consultant, Metals and Ceramics Division*

We propose to investigate the hydrogen absorption/desorption properties of alanate compounds [$NaAlH_4$, $LiAlH_4$, AlH_3, $Mg(AlH_4)_2$] capable of storing up to approximately 10 wt % hydrogen. The synthesis of these materials will be accompanied and guided by thermodynamic modeling and crystal structure analysis. Alloying will be carried out by high-energy milling. Elements or compounds will be added to improve the absorption/desorption kinetics and to shift the absorption/desorption conditions closer to ambient conditions.

To reduce the country's dependence on foreign oil supplies and to promote a cleaner environment, the President has proposed the FreedomCar (Freedom Cooperative Automotive Research) initiative. Its long-term goal is to develop technologies for hydrogen-powered fuel cell cars and trucks. This project focuses on a particularly important issue of the initiative, namely, hydrogen storage. The objective is to develop materials which can absorb and desorb large amounts of hydrogen (e.g., 10 wt %) at near-ambient conditions.

Alanate materials (i.e., materials containing AlH4$^-$ ions, such as for example $LiAlH_4$) will be prepared by high-energy ball milling of powder precursor materials. Small quantities of elements or compounds with catalytic activity will be added to improve the absorption/desorption kinetics ("micro-alloying"). Macro-alloying (i.e., ≈1 wt % and above) with the aim of shifting the absorption/desorption conditions closer to ambient will be guided by thermodynamic calculations as well as electronegativity and atomic size considerations.

During FY 2003, this project focused on experiments designed to assure that we are able to reproduce existing results for high-performance hydrogen-storage materials and that our equipment for measuring hydrogen storage capacity values is performing properly. Considerable effort was spent on determining the precision and reproducibility of a recently acquired piece of equipment for characterizing hydrogen-storage materials. This equipment measures the hydrogen pressure as a function of the hydrogen concentration in the material, for absorption and desorption at preselected temperatures (the so-called pressure-composition-isotherm, PCI). The equipment also measures, as a function of temperature and pressure, the rates with which hydrogen is absorbed and desorbed. Following published information, commercially available sodium alanate, $NaAlH_4$, was high-energy milled with 2 wt % of $TiCl_3$. Its hydrogen absorption and desorption behavior was measured as a function of pressure. The curves obtained demonstrated the two-stage decomposition reaction:

$$3NaAlH_4 \rightarrow Na3AlH6 + 2Al + 3H_2 \rightarrow 3NaH + 3Al + 5/2\ H_2 \quad (1)$$

According to a desorption PCI curve measured by us, the hydrogen storage capacity was 4.95 wt %. The hydrogen storage capacity was independently measured by weighing the fully charged as well as the material discharged according to the right-hand side of Eq. (1). The storage capacity measured in this way was 4.66 wt %, which is in reasonable agreement with the PCI value of 4.95 wt %. These values are not as high as the theoretical capacity, 5.6 wt %, but are in agreement with typical values found in the open literature. We have now reached the point at which we will be able to perform experiments with novel compositions.

If improved hydrogen storage capacities can be obtained, and if absorption and desorption occur at close-to-ambient conditions, this project will be very valuable for the Energy Efficiency and Renewable Energy (EERE) program of DOE.

Other federal agencies involved in supporting cutting edge research in carbon nanotube synthesis and electronic application such as DARPA and NASA will directly benefit from increased control over the carbon nanotube film growth process. A specific example is the application of carbon nanotubes as field emitters. The ability to control the growth rate and the growth temperature is also relevant to mass production of carbon nanotubes. Agencies that are involved in supporting carbon nanotube composite research such as NASA would directly benefit from a high-rate carbon nanotube synthesis process.

Enhancing Performance of Hydrogen Storage Materials through Nanoscale Design

V. K. Sikka,[1] G. Muralidharan,[1] T. J. Huxford,[1] T. M. Besmann,[1] N. C. Gallego,[1] and M. P. Paranthaman[2]
[1]*Metals and Ceramics Division*
[2]*Chemical Sciences Division*

Insufficient gravimetric capacities and slow hydriding/dehydriding kinetics have been recognized as hurdles to be overcome in the quest for future hydrogen storage materials. The objective of this project is to examine a novel approach for enhancing the hydriding/dehydriding kinetics based on the use of nanometer-thick films. The feasibility of this approach will be studied by depositing films of magnesium on the interior surfaces of a microporous silica gel with a large surface area (up to 1000 m^2/g) and examining the hydriding/dehydriding characteristics of the resulting material. The use of silica gel as the template material is a key to obtaining improved kinetics without sacrificing storage capacity. Improved kinetics and lower operating temperatures are benefits anticipated as a result of using this approach.

Hydrogen-storage materials are of great interest for the new national and international interest in the hydrogen economy. Based on the potential use of hydrogen storage materials in automotive applications, a storage criteria of 9 wt % of hydrogen has been set as a national goal and there are many efforts under way to develop such materials. In addition to meeting the gravimetric capacity, such materials should also be capable of adsorbing and desorbing the hydrogen at temperatures less than 100°C at pressures of 1–10 atm. A number of metal hydrides have been studied for their potential use as hydrogen-storage materials. Such studies have shown that slow kinetics of the hydriding/dehydriding reaction, high temperatures required to absorb/release the hydrogen, or insufficient storage capacities limit the use of metal hydrides.

A number of approaches, such as physical and chemical treatments, have been carried out to improve the hydriding and dehydriding kinetics of metal hydrides with limited success. Our approach to addressing this problem is based on developing a general scheme for improving the hydriding/dehydriding kinetics of all hydrogen storage materials of interest. We plan to use magnesium as a model material for developing and demonstrating our concept. In addition to improving the hydriding/dehydriding kinetics using this methodology, our objective is to also achieve reduced operating temperatures in the range of 100–150°C in such films.

The core theme of our approach is the use of thin films of hydrogen-storage materials with a thickness of less than 50 nm. A significant benefit in using such films is that diffusion is required only over very short distances when the surfaces of the thin films are exposed to the gas. In addition, to achieve sufficient gravimetric storage capacity, the internal surfaces of a foam-like material with a large surface area and an interconnected pore structure that is permeable to the surrounding gas medium have to be coated with the thin film that can store hydrogen. An example of this kind of a material is silica gel. These gels are commonly used for humidity control, and catalyst support. The combined use of the silica gel as a template and a thin-film hydrogen-storage material is unique and novel.

Significant progress has already been made over the first three months of the project. Several candidate silica gel materials have been identified and are currently being evaluated for use in this work. The pore surface area has been evaluated for one particular batch of materials using Brunauer-Emmett-Teller gas adsorption measurements. The results show a typical total accessible pore surface area of about 430 m^2/g. Experiments are under way to evaluate deposition techniques that would be suitable for coating the internal surfaces of these gels with Mg/Mg-alloy composite thin films. Initial experiments have explored the use of physical vapor deposition methods to coat the silica gels with magnesium. These techniques exploit the fact that the vapor pressure of magnesium is high at relatively low temperatures due to its low melting point. Silica gels were exposed to an atmosphere consisting of a high partial vapor pressure of magnesium through heat treatment in a furnace either in a sealed quartz tube or in a flowing Ar/H_2 atmosphere. The resulting material was crushed and the phases present were analyzed through X-ray diffraction. MgO peaks were observed in the diffraction pattern, indicating that magnesium was indeed deposited but was subsequently oxidized during exposure to air. Future experiments will focus on protecting the magnesium films through handling in an inert atmosphere and subsequently depositing palladium to prevent

oxidation. An alternate and novel technique using rapid sequential heating of magnesium and palladium with a high-power IR lamp in a flowing Ar/H_2 atmosphere has also been attempted to minimize the problems due to oxidation of magnesium. Further characterization of this material is in progress.

Chemical vapor infiltration will also be pursued as an alternative technique for depositing composite thin films. Experiments to evaluate the hydriding/dehydriding properties of the material produced have also been initiated.

Hydrogen storage and delivery materials are of significant interest to DOE and other federal agencies such as DARPA. If this scheme is successful, engineering hydrogen-storage materials based on magnesium with gravimetric capacities up to 9.3 wt % may be feasible, thus satisfying both the existing and future DOE criteria. There is also the additional advantage that, if necessary, this methodology can be applied to other hydrogen-storage materials.